学位論文
Doctor's Thesis

Optimization of Contrast Delivery and Radiation Dose Reduction at Abdominal Multidetector CT

（腹部の多列検出器 CT における至適な造影剤投与および放射線被曝低減）

彌永由美
Yumi Yanaga

熊本大学大学院医学教育部博士課程病態制御学専攻放射線診断学

指導教員

山下　康行　教授
熊本大学大学院医学教育部博士課程病態制御学専攻放射線診断学

2009年3月

学　位　論　文

Doctor's Thesis

論文題名　：　**Optimization of Contrast Delivery and Radiation Dose Reduction at Abdominal Multidetector CT**

（腹部の多列検出器 CT における至適な造影剤投与および放射線被曝低減）

著 者 名　：　彌 永 由 美

（単名）　Yumi Yanaga

指導教員名　：　熊本大学大学院医学教育部博士課程病態制御学専攻放射線診断学

山 下 康 行 教授

審査委員名　：

放射線治療医学担当教授	大屋　夏生
形態構築学担当教授	児玉　公道
循環器病態学担当教授	小川　久雄
分子病理学担当准教授	今村　隆寿

２００９年３月

Contents

Abstract

1. Characteristics of Iodine Enhancement and Image Noise at Multidetector CT Scan with a Low Tube Voltage Technique

Purpose: To investigate the characteristics of low tube voltage CT scanning including iodine enhancement, image noise, and radiation exposure.

Materials and Methods: We conduced phantom experiment using a phantom including iodine solution syringe (iodine solutions concentration: 0-, 2-, 4-, 6-, 8-, 10-, 12-, and 14 mg/mL) with a 64-detector CT scanner. Multislice helical scans were acquired at 80-, 120-, and 140 kV techniques to investigate the relationship between the attenuation- and image noise values.

Results: There was a strong positive linear correlation between the iodine concentration and the attenuation value at each kV ($r = 0.99$, $p < 0.001$). Compared to scans acquired at 80 kV, at 140- and 120 kV, the iodine attenuation values were 1.85 and 1.59 times- and the mean image noise was 2.82 and 2.29 times higher, respectively.

Conclusion: Iodine enhancement and image noise increased in low kV scan technique with a given tube current second.

2. Optimization of Contrast Dose for Pancreatic Dynamic MDCT

Purpose: To prospectively compare the effect of a protocol with a fixed contrast injection dose (Protocol 1: P1) and one with a contrast dose tailored to patient body weight (Protocol 2: P2) on pancreatic enhancement at pancreatic dynamic CT.

Methods and Materials: We randomly assigned 78 patients with suspicion of pancreatic tumor to 1 of 2 protocols (of 39 patients in each protocol). In P1, we delivered a fixed contrast dose (120 ml Iohexol-300); in P2 we injected a dose tailored to the patient body weight (BW, 2.0 ml/kg). Pancreatic enhancement during pancreatic parenchymal phase (PPP) and hepatic enhancement during portal venous phase (PVP) were compared.

Results: Under P1, in patients whose BW equal or more than 60kg, pancreatic and hepatic enhancement were statistically significantly lower than that in patients whose BW less than 60 kg. Under P2, there were no significant difference in pancreatic and hepatic enhancement between high and low BW group.

Conclusion: The patient BW-tailored dose protocol (P2) yielded satisfactory pancreatic and hepatic enhancement irrespective of patient weight.

3. Optimal Contrast Dose for Depiction of Hypervascular Hepatocellular Carcinoma at Dynamic MDCT

Purpose: To investigate prospectively the optimal contrast dose for the depiction of hypervascular hepatocellular carcinoma (HCC) at dynamic CT.

Materials and Methods: 47 patients with hypervascular HCCs were randomly assigned to 3 protocols; a contrast dose of 450-, 525-, and 600 mgI per kg weight (BW) was delivered in protocols A, -B, and -C, respectively. We measured the tumor-liver contrast (TLC) during the hepatic arterial phase (AP) in the 3 groups and compared the results.

Results: The TLC in protocol A was significantly lower than that in protocol B and C. In the mean score of tumor conspicuity, there was no significant difference between protocols B and C.

Conclusion: The Administration of a total iodine dose of 525 mg or more per kg BW is desirable for the good or excellent depiction of hypervascular HCC.

4. Low-Dose Hepatic Perfusion CT Using a Low Tube Voltage Technique

Purpose: To investigate the clinical applicability of the low-dose hepatic perfusion CT using a low tube voltage technique and an adaptive noise reduction filter.

Materials and Methods: Thirty patients underwent serial hepatic dynamic CT. The first 15 patients were assigned to 120 kVp protocol; and the subsequent 15, 80 kVp protocol. We applied an adaptive noise reduction filter for images obtained at 80 kVp scan. The image noise on liver parenchyma was measured on 120-, 80-, and filtered 80 kVp images. Furthermore, 2 radiologists qualitatively evaluated image quality of the perfusion images for diagnostic applicability. We also calculated estimated effective dose for each protocol.

Results: There was no statistically significant difference in the image noise between 120- and filtered 80 kVp images. In the evaluation of diagnostic acceptability, there was no statistically significant difference between 120- and filtered 80 kVp images.

Conclusion: The hepatic perfusion CT with 80 kVp and an adaptive noise reduction filter had almost comparable image quality as that with 120 kVp.

和文抄録

1. 低電圧撮像法を用いた多列検出器CTにおけるCT値および画像ノイズの検討

目的：低電圧 CT 撮像における CT 値・画像ノイズ・放射線被曝を検討する。

方法：ヨード溶液で満たされたシリンジファントムを 64 列 CT で撮影し（管電圧は 80, 120, 140kV）、その CT 値および画像ノイズを測定した。

結果：それぞれの電圧においてヨード濃度と CT 値に強い正の線形相関を認めた。80kV における画像ノイズは 140kV の 2.82 倍、120kV の 2.29 倍であった。

結論：低電圧撮像法では CT 値は増加するが、画像ノイズも増加することが判明した。

2. 膵ダイナミック CT における至適造影剤量についての検討

目的：膵ダイナミック CT において、造影剤量固定法 (protocol 1: P1) と体重によって造影剤量を決定する方法 (protocol 2: P2) の二者で膵および肝の造影効果を比較する。

方法：膵腫瘍が疑われる 78 人を P1 (造影剤量固定 120ml) と P2 (造影剤量体重あたり 2.0mL) のプロトコールに振り分け膵ダイナミック CT を施行した。P1 及び P2 における膵実質相における膵・門脈相における肝の造影効果を測定した。

結果：造影剤量固定法では、体重 60kg 以上の高体重患者において膵および肝の造影効果が 60kg 未満の患者と比較して統計学的に有意に低かった。体重により造影剤を決定する方法では、高体重群と低体重群の間でこれらに統計学的有意差はなかった。

結論：体重によって造影剤量を決定した方法では、体重によらず膵および肝実質の十分な造影効果を得ることができた。

3. 肝ダイナミック CT における肝癌描出の至適造影剤量についての検討

目的：肝ダイナミック CT における肝癌描出の至適造影剤量について検討する。

方法:肝癌患者 47 人を造影剤量によって 3 つのプロトコール(造影剤量 450, 525, 600mg/kg）に振り分け、肝ダイナミック CT を施行した。それぞれのプロトコールにおいて腫瘍ー肝コントラスト (TLC)を測定した。

結果：TLC は、造影剤量 450, 525 mg/kg 群間および 450, 600 mg/kg 群間ではいずれも前者において統計学的に有意に低かった。これに対して 525, 600 mg/kg 群間では有意差はなかった。また、腫瘍描出の顕著性についても 525, 600 mg/kg 群間では有意差はなかった。

結論：肝癌の良好な描出においては 525mg/kg 以上の造影剤量が必要である。

4. 低管電圧撮影による肝血流 CT の検討

目的：低管電圧テクニックおよび適応型ノイズ低減フィルター（以下、ノイズ低減フィルター）を用いた肝血流 CT が実際の臨床に応用出来るか否か検討する。

対象と方法：対象は肝血流 CT を実施した 30 人の患者。前半 15 人は標準管電圧プロトコール（120 kVp, 200 mAs）、後半 15 人は低管電圧プロトコール（80 kVp , 150 mAs）で撮影し、後者についてはノイズ低減フィルターを画像に適応した。両プロトコールで画像ノイズの定量評価、画質に関する視覚評価を行った。

結果：画像ノイズおよび画質は、２プロトコールで統計学的有意差はなかった(p = 0.30 および 0.20)。

結論：低管電圧およびノイズ低減フィルターによる肝血流画像は、標準管電圧肝血流画像の代用として実際の臨床に応用可能である。

Publication list

1: Yanaga Y, Awai K, Nakayama Y, Nakaura T, Tamura Y, Hatemura M, Yamashita Y. Pancreas: Patient Body Weight-tailored Contrast Material Injection Protocol versus Fixed Dose Protocol at Dynamic CT. Radiology. 2007 ;245(2):475-82.

2: Yanaga Y, Awai K, Nakaura T, Namimoto T, Oda S, Funama Y, Yamashita Y. Optimal contrast dose for depiction of hypervascular hepatocellular carcinoma at Dynamic CT Using 64-MDCT. AJR Am J Roentgenol. 2008 ;190(4):1003-9.

3: Yanaga Y, Awai K, Nakaura T, Oda S, Funama Y, Bae KT, Yamashita Y. Effect of Contrast Injection Protocols with Dose Adjusted to the Estimated Lean Patient Body Weight on Aortic Enhancement at CT Angiography. AJR Am J Roentgenol. (in press)

4: Yanaga Y, Awai K, Nakayama Y, Nakaura T, Tamura Y, Funama Y, Aoyama M, Asada N, Yamashita Y. Optimal dose and injection duration (injection rate) of contrast material for depiction of hypervascular hepatocellular carcinomas by multidetector CT. Radiat Med. 2007;25(6):278-88.

5: Yanaga Y, Awai K, Nakaura T, Oda S, Funama Y, Bae KT, Yamashita Y. Low-dose Multidetector CT Urography (MDCTU) Using a Low Tube-Voltage Technique and an Adaptive Noise Reduction Filter: Feasibility Study. AJR Am J Roentgenol. (in press)

6: Nakaura T, Awai K, Yanaga Y, Nakayama Y, Oda S, Funama Y, Yamashita Y. Detection of Early Enhancement of Hypervascular Hepatocellular Carcinoma Using Single Breath-Hold 3D Pixel Shift Dynamic Subtraction MDCT. AJR Am J Roentgenol. 2008;190(1):W13-8.

7: Oda S, Awai K, Liu D, Nakaura T, Yanaga Y, Nomori H, Yamashita Y. Ground-Glass Opacities on Thin-Section Helical CT: Differentiation Between Bronchioloalveolar Carcinoma and Atypical Adenomatous Hyperplasia. AJR Am J Roentgenol. 2008;190(5):1363-8.

8: Awai K, Nakayama Y, Nakaura T, Yanaga Y, Tamura Y, Hatemura M, Funama Y, Yamashita Y. Prediction of aortic peak enhancement in monophasic contrast injection protocols at multidetector CT: phantom and patient studies. Radiat Med. 2007 ;25(1):14-21.

9: Nakayama Y, Awai K, Yanaga Y, Nakaura T, Funama Y, Hirai T, Yamashita Y. Optimal contrast medium injection protocols for the depiction of the Adamkiewicz artery using 64-detector CT angiography. Clin Radiol. 2008;63(8):880-7.

10: Liu D, Awai K, Funama Y, Oda S, Nakaura T, Yanaga Y, Hatemura M, Kawanaka K, Yamashita Y. Identification and characterization of focal ground-glass opacity in the lungs by high-resolution CT using thin-section multidetector helical CT: experimental study using a chest CT phantom.
Radiat Med. 2008 ;26(1):21-27.

11: Namimoto T, Awai K, Nakaura T, Yanaga Y, Hirai T, Yamashita Y.
Role of diffusion-weighted imaging in the diagnosis of gynecological diseases.
Eur Radiol. 2008 7.

12: Funama Y, Awai K, Taguchi K, Hatemura M, Yanaga Y, Shimamura M, Yamashita Y. Cone-Beam Technique for 64-MDCT of Lung: Image Quality Comparison with Stepwise (Step-and-Shoot) Technique. AJR Am J Roentgenol. 2009;192(1):273-278.

13: 彌永由美、粟井和夫、中山善晴、中浦猛、田村吉高、羽手村昌宏、船間芳憲、山下康行. 腹部 MDCT 検査法の最近の考え方と推奨プロトコール. 臨床画像 22(9), 950-964, 2006

14: 彌永由美、粟井和夫、中山善晴、中浦猛、田村吉高、羽手村昌宏、船間芳憲、山下康行. 腹部 MDCT における最近の造影の考え方：造影剤注入時間一定法. 映像情報 Medical 38(7), 106-111, 2006

15: 中浦猛、粟井和夫、浪本智弘、彌永由美、山下康行. ３T MRI の臨床：肝・胆・膵. 臨床画像 23(11), 1293-1300, 2007

16: 彌永由美、粟井和夫、中浦猛、山下康行. CT におけるヨード造影剤投与法のトレンド. 臨床画像 23(10), 1202-1207, 2007

17: 彌永由美、粟井和夫、中浦猛、船間芳憲、尾田済太郎、中村信一、浪本智弘、山下康行. Multidetector CT urography (MDCTU). 映像情報 Medical 40(7), 113-119, 2008

18: 彌永由美、粟井和夫、中浦猛、伊牟田真功、浪本智弘、尾田済太郎、中村信一、山下康行. 64 列 CT による肝パフュージョン CT. Innervision 230(6), 47-51, 2008

Acknowledgements

These academic investigations took place during my postgraduate study period from 2006-2009, at the department of Diagnostic Radiology & Imaging, Kumamoto University School of Medicine.

I'd like to express my sincere thanks to Professor Yasuyuki Yamashita, Chairman of the Department of Diagnostic Radiology, Graduate School of Medical Sciences, Kumamoto University, his generous guidance and constructive instructions. Never would I have finished my postgraduate study without help in academic field.

I am deeply grateful to Dr. Kazuo Awai, professor, Department of Diagnostic Image Analysis, Graduate School of Medical Sciences, Kumamoto University, who has been instructing me during the most part of my research with his profound insight into the Radiological Science shed on my whole study. I have learned much from his scientific way of thinking, serious working skill and style and honest personality.

I, of course, owe a great deal to Dr. Nakayama, Dr. Nakaura, and Dr. Oda for their cooperation and helps in my work. My appreciation also goes to all the other members of the Department of Diagnostic Radiology, Graduate School of Medical Sciences, Kumamoto University.

Finally I want to say thank you to all people who have ever helped me and loved me. I determine to do better for the sake of your love in the future.

Abbreviations

CT: computed tomography

MDCT: multidetector computed tomography

BW: body weight

PPP: pancreatic parenchymal phase

PVP: portal venous phase

HCC: hepatocellular carcinoma

TLC: tumor-liver-contrast

HAP: hepatic arterial phase

EP: equilibrium phase

CTDIw: weighted computed tomography dose index

CNR: contrast-to-noise ratio

HU: Hounsfield unit

CTDI: computer tomography dose index

FOV: field of view

ROI: region of interest

$CTDI_{volume}$: computer tomography dose index volume

SD: standard deviation

US: ultrasonography

IPMN: intraductal papillary mucinous neoplasm

MR

GEE: generalized estimating equation

SPSS: Statistical analyses were performed with a statistical software package

CTHA: computer tomography during hepatic arteriography

ANOVA: analysis of variance

LCD: liquid crystal display

LRLT: living-related liver transplants

PSE: percutaneous transarterial splenic embolization

PTPE: percutaneous transhepatic portal vein embolization

DLP: dose-length product

Chapter 1 Background and Objectives

Contents

1. Multidetector CT (MDCT) for abdominal imaging

1.1 Current status of MDCT for the abdomen

Since its introduction in 1998 (1, 2), volumetric computed tomography (CT) scanning with multidetector CT (MDCT) scanners has revolutionized diagnostic imaging. Improvements implemented over the last few years, e.g. increased detector width along the X axis, faster gantry rotation time, more powerful X-ray tubes, and improved image reconstruction algorithms, render MDCT the most robust imaging tool among various imaging modalities.

MDCT scanners capable of acquiring 64 channels of helical data simultaneously represent the greatest incremental gain in scan speed and make possible rapid thin-section imaging of the regional body anatomy. Faster scanning facilitates imaging at greater speed and at shorter breath-hold times, yields better image quality, and improves three-dimensional (3D) and multiplanar reconstructions.

MDCT, adapted for hepatic and pancreatic imaging, provides multiphase and multiplanar data obtained during defined circulatory phases that optimally visualize the organ blood flow information and facilitate the detection and characterization of focal parenchymal lesions. Factors related to tumor size and the tissue-to-contrast ratio increase the detection rate of abdominal focal lesions. Furthermore, the enhancement

characteristics of multiphase scanning and the availability of thinner reconstructed sections improve lesion characterization on MDCT images.

1.2 Hepatic dynamic MDCT and contrast material administration

The most common primary malignant hepatic neoplasm is hepatocellular carcinoma (HCC). It usually occurs as a complication of chronic liver disease and most often arises in patients with hepatic cirrhosis. Imaging the cirrhotic liver by MDCT raises technical challenges as the parenchyma of the cirrhotic liver is changed by degenerative processes such as fibrosis, scarring, and nodular regeneration. It is not only difficult to detect true hepatic tumors in patients with cirrhosis, but the cirrhotic changes create lesions that may simulate tumors. Most HCCs are hypervascular lesions that typically enhance during the maximum hepatic arterial enhancement phase and they are demonstrated as hypo-attenuated lesion in the equilibrium phase ("washout" lesions in the equilibrium phase) (Figure 1.1.) (3-9).

Current MDCT scanners can scan the whole liver in 3-10 sec. In many Japanese institutes hepatic dynamic CT study includes 4-phase scans that consist of pre-enhanced-, hepatic arterial phase (HAP)-, portal venous phase (PVP)-, and equilibrium phase (EP) scans. It has been demonstrated that this multiphase approach to scanning greatly improves the detection rate of HCCs (9, 10).

The HAP, the most important phase for the detection of HCCs, occurs 35-45 sec after the start of contrast administration. Quantification of the blood flow in HCC during the HAP is also important for treatment selection and for assessing the treatment response.

The PVP is 60-80 sec after the start of contrast administration. As typical HCCs tend to become isodense compared with the surrounding liver parenchyma, PVP scans are not useful for the demonstration of HCCs (9, 10). However, during the PVP, the liver parenchyma is maximally enhanced and this phase is therefore suitable for the depiction of hypovascular tumors such as well-differentiated HCCs and metastatic liver tumors (11-14). The PVP is also useful for the depiction of tumor thrombosis in the portal vein because this vessel is most highly enhanced during the PVP.

The EP, occurring 180 sec or more after the start of contrast injection, is also important for the detection of typical HCCs. Most HCCs are demonstrated as a hypo-attenuated area during the EP and some well-differentiated HCCs are only demonstrated during this phase (8-10).

The recommended iodine injection dose for hepatic dynamic MDCT ranges between 40-45 g. Some (11, 14, 15) have advocated that the dose for hepatic dynamic CT be adjusted according to the individual patient's body weight. As the most recently

introduced 64-detector CT instruments can scan the whole liver in 2-3 sec, it may be possible to reduce the iodine dose. However, to our knowledge, the optimal iodine dose for hepatic dynamic MDCT using a 64-detector CT scanner has not been elucidated.

1.3 Pancreatic dynamic MDCT and contrast material administration

MDCT has been established as the primary initial imaging method for both the detection and staging of suspected pancreatic carcinoma. Most studies reported that CT is highly reliable when it demonstrates features indicating that a tumor is unresectable.

For the detection or staging of pancreatic cancer, images are acquired in two phases, the pancreatic parenchymal phase (PPP) and the portal venous phase (PVP). The PPP begins 40-50 sec after the start of contrast injection. Maximal pancreatic enhancement is obtained during the PPP and the detection of pancreatic cancer is maximized during this phase because the lesion is hypo-attenuated compared with the surrounding pancreatic parenchyma (Figure 1.2.) (16-19). The PPP is also useful for evaluating tumor invasion into peri-pancreatic arteries and the portal vein because these vessels are intensely enhanced during this phase (17, 18). As described in the previous

section, the PVP occurs 60-80 sec after the start of contrast administration and is useful for the detection of liver metastases because metastatic lesions from pancreatic cancer are most clearly demonstrated as hypovascular tumors during the PVP.

Many patients undergoing pancreatic dynamic CT were subjected to contrast injection protocols in which the dose and injection rate were fixed (16-23), e.g. a 150-mL contrast volume with an iodine concentration of 300 mgI/mL delivered at 5 mL/sec (17, 18). As the feeding arteries to the pancreas are branches derived from the abdominal aorta, pancreatic- and abdominal aortic enhancement is thought to occur in parallel. Because aortic enhancement is associated with the contrast dose per body weight (15, 24), protocols with the dose adjusted for the body weight may be appropriate for pancreatic dynamic CT. However, to date, no contrast injection protocol with the dose adjusted for the body weight has been adopted for pancreatic dynamic CT.

2. Radiation dose reduction in abdominal MDCT

2.1 Necessity for a dose reduction at abdominal MDCT

CT is widely used in the clinical setting because it is the most robust tool for body imaging. Patients now undergoing abdominal MDCT are subjected to higher radiation exposure because of the routine use of thinner sections, extended acquisition volumes, and multiphase acquisitions. The radiation dose from hepatic or pancreatic dynamic CT studies is relatively high because many patients suspected of harboring tumors undergo multiphase dynamic enhanced CT.

The detector width of MDCT scanners has increased over the years and the current 64-detector scanners make it possible to scan a 40 mm-wide area. This led to the widespread use of body perfusion- such as hepatic perfusion CT which can demonstrate the vascular physiology of the hepatic parenchyma and existing lesions. However, the radiation dose at hepatic perfusion CT is several times higher than at hepatic dynamic CT because the same region is scanned 10-20 times without table movement.

Thus, radiation exposure at dynamic- and body perfusion CT is the most important issue at abdominal CT(25). According to Berrington de Gonzalez (26),

among patients living in advanced countries, Japanese patients are subjected to the highest radiation exposure at CT, indicating that efforts must be made to reduce the radiation dose.

2.2 Techniques for dose reduction at MDCT

Strategies for reducing the radiation dose at MDCT include lowering the tube current or tube voltage (27-31), performing fewer scans (32-35), using X-ray filtration (36), controlling the x-ray tube focal spot motion and beam collimation (37), applying adaptive noise reduction filters (29, 38-40), and using a dose modulation technique (38, 41-43). Among these methods, low tube voltage techniques drastically reduce the radiation dose (29, 31). However, as low-contrast detectability, tissue contrast, iodine enhancement, and image noise are affected by the low tube voltage (90 or 80 kVp) technique, the application of this method in the clinical setting requires an understanding of the characteristics of low tube voltage images.

2.3 Low kVp technique for abdominal MDCT

Low tube voltage (low kVp) settings vary with CT scanners and CT manufacturers. We can evaluate the radiation dose by using the weighted CT-dose

index (CTDIw) (44) provided by the manufacturer. Data were acquired at 90 and 80 kVp with CT scanners available at our hospital (Philips16-detector CT scanner [IDT-16] and the 64-detector scanner [Brilliance-64]). At identical mAs settings, the CTDIw on 90-kVp scans was about 43% of 120-kVp scans; on 80-kVp scans it was about 31% of 120-kVp scans. Although the currently available MDCT scanners can accommodate the higher tube current needed with low tube voltage settings, the tube power is not sufficiently high for these scan parameter settings. This limits the use of the low-tube voltage technique in larger patients. However, as the physique of Japanese patients tends to be relatively small, they are good candidates for the low kVp technique.

In our phantom study, there was a direct correlation between the contrast-to-noise ratio (CNR) and the radiation dose in the center of the phantom at both 90- and 120 kVp (29). At identical radiation doses, the CNR at 90 kV was 1.29 times higher than at 120 kVp and at identical CNR, the radiation dose at 90 kVp was 0.71 times than at 120 kVp.

2.4. Adaptive noise reduction filter for MDCT

The increased noise on low tube voltage images can be reduced with adaptive noise reduction filters (38-40). In general, when a noise reduction filter is used, image blurring tends to be increased and edge enhancement reduced, although the image noise tends to decrease as the smoothing factor increases. In the clinical setting, the recently developed adaptive noise reduction filters simultaneously achieve noise reduction and edge preservation (28, 40).

The XRES filter is an adaptive noise reduction filter developed at the Medisys Research Laboratory (Philips Healthcare, Paris); it can be adopted when images are obtained at 80 kVp. The generic image-processing algorithm of the XRES filter was designed to compensate for the higher noise level in this low-dose dataset without altering fundamental clinical information. The main principle underlying XRES is to separate the medical image into the sum of several relevant components to which specialized filtering kernels are applied independently (Figure 1.3A). The processed components are then recomposed to form a filtered result. By adapting both the separation step and the filtering step to different imaging modalities, XRES was first successfully applied to the filtering of ultrasound images (45, 46), then to x-ray-, and more recently to CT cardiac images (40).

To process low kVp CT data, the main steps used by the dedicated XRES filter are as follows. The initial image is decomposed into a so-called Laplacian pyramid (47). Decomposition uses down-sampled images to create spatial frequency sub-bands that represent the features of the medical image at different scales. This decomposition allows XRES to adapt to differently-sized anatomic structures forming the image (Figure 1.3B). For each spatial resolution level, 3 component classes, A, B and C, are identified where A = weakly textured organs inside, B = elongated structures, and C = organ boundaries. Thus, the psoas muscle is assigned to class A, the ureter to class B, and the boundary between areas with/without contrast irrigation to class C. Specialized processing is applied to each of the 3 components; it isotropically smoothes the organs inside, directionally smoothes and enhances the elongated structures, and it carefully notes the organ boundaries to avoid introducing misleading artifacts. For each spatial resolution level, a processed sub-band is recomposed from the 3 processed components. The final filtered image results from the application of the reconstruction algorithm (47) using the processed sub-band derived for all resolution levels.

3. Research objectives

In ***chapter 2***, to elucidate relationships between iodine concentration and attenuation value (CT number [HU]) or image noise in each tube voltage setting, we conducted phantom experiments. We also investigated radiation dose (CT dose index: CTDI) in various tube currents in each tube voltage setting.

As outlined in section 2.3, contrast injection protocols for abdominal dynamic CT with the dose adjusted to the patient body weight appear to be rational. However, this contrast administration method has not found international acceptance. In ***Chapter 3***, a prospective comparison of the effect of protocols with a fixed contrast dose and with a contrast dose tailored to the patient's body weight is presented. The comparison was performed to assess the validity of the tailored dose at pancreatic dynamic CT.

Current 64-detector CT scanners can scan the whole abdomen in less than 5 sec. Although this may make it possible to reduce the iodine dose, to our knowledge, the optimal dose for abdominal dynamic MDCT with a 64-detector scanner has not been determined. ***Chapter 4*** presents a discussion of the optimal iodine dose for hepatic dynamic CT to detect hypervascular liver tumors using contrast doses tailored to the patient's body weight.

Chapter 5 examines the clinical validity of low-dose hepatic perfusion CT using scan parameters determined in the phantom study described in chapter 2.

Chapter 2. Characteristics of Iodine Enhancement and Image Noise at Multidetector CT Scan with a Low Tube Voltage Technique

Contents

ABSTRACT

Purpose: To investigate the characteristics of low tube voltage CT scanning including iodine enhancement, image noise, and radiation exposure.

Materials and Methods: We conduced phantom experiment using a phantom including iodine solution syringe (iodine solutions concentration: 0-, 2-, 4-, 6-, 8-, 10-, 12-, and 14 mg/mL) and a low contrast module phantom. We used a 64-detector scanner for the phantom studies. Multislice helical scans were acquired at 80-, 120-, and 140 kV techniques to investigate the relationship between the attenuation- and image noise values in the iodine solutions. We also obtained mutislice step-and-shoot scans using 80- and 120 kV to study the effect of an adaptive noise reduction filter at low kV scanning on image noise.

Results: There was a strong positive linear correlation between the iodine concentration and the attenuation value at each kV ($r = 0.99$, $p < 0.001$). Compared to scans acquired at 80 kV, at 140- and 120 kV, the iodine attenuation values were 1.85 and 1.59 times- and the mean image noise was 2.82 and 2.29 times higher, respectively. On the low contrast module phantom, the image noise on the processed images with the adaptive noise reduction filter obtained with 80 kV and 150 mAs was comparable to that on the images obtained with 120kV and 200 mAs.

Conclusion: Iodine enhancement and image noise increased in low kV scan technique with a given tube current second. Use of an adaptive noise reduction filter represents one solution for dealing with increased image noise on low kV scans.

INTRODUCTION

Currently, 5,800 multidetector CT (MDCT) scanners are in use in Japan; at 6.2 scanners/100,000 population, the availability of these instruments is greater in Japan than elsewhere. As the radiation exposure at CT is higher than at other imaging studies, the risk of cancer attributable to diagnostic radiation exposure is also highest in Japan (26) and a reduction in the radiation exposure at CT is highly desirable.

Among methods developed to reduce the radiation dose at MDCT, low tube voltage (90- or 80 kV) techniques drastically reduce the radiation dose (29, 30, 48). However, tissue enhancement by the iodine contrast material, the image noise, and tissue contrast are affected by the low tube voltage technique. Therefore, the use of these techniques in the clinical setting requires an understanding of the image characteristics of low tube voltage images.

To investigate the characteristics of low tube voltage scanning including iodine enhancement, image noise, and radiation exposure, we conduced phantom experiments using a syringe phantom containing different concentrations of iodine solution and a low contrast module phantom.

MATERIALS AND METHODS

Phantom

A multislice CT phantom (type MHT, Kyoto-Kagaku, Kyoto, Japan) was employed to investigate the relationship between the attenuation value (CT number) or the image noise value of iodine solutions and the tube voltage. The long and short diameter and the length along the z-axis of the phantom were 330-, 220-, and 185 mm, respectively. A 10.0-mm syringe containing different concentrations of iodine solution (0-, 2-, 4-, 6-, 8-, 10-, 12-, 14 mg/mL) was inserted into a 11.0-mm diameter cavity located in the center of the phantom along the z-axis (Figure 2.1.).

In another set of experiments we employed a low-contrast module phantom (Catphan 424; Phantom Laboratory, Cambridge, NY) (Figure 2.2.) to investigate the possibility of reducing the radiation dose by using 80 kV and an adaptive noise reduction filter without producing a concomitant increase in the image noise compared with 120 kV scans. Both the diameter and the length of the phantom along the z-axis were 20.0 cm. The phantom contained several cylindrical low-contrast objects of different sizes arranged in a circle; the background was of uniform density. We used the background to measure the image noise at each scan technique applied.

CT scan

Our phantom studies were carrried out on a 64-detector scanner (Brilliance-64, Philips Medical Systems, Cleveland, OH).

Multislice helical scans were acquired at 80-, 120-, and 140 kV to investigate the relationship between the attenuation- and image noise values of the iodine solutions and tube voltage. The scan parameters were: tube rotation time 0.75 sec, detector collimation 64 x 0.625 mm, section thickness 5 mm, scan field of view (FOV) 50 cm, tube current second 250 mAs, and reconstruction kernel C.

Multislice step-and-shoot (axial) scans were obtained at 80- and 120 kV to investigate the effect of an adaptive noise reduction filter (XRES filter, Philips; see ***Chapter 1***) in low kV scan. The scan parameters at 120 kV were: rotation time 0.5 sec, detector collimation 8 x 5 mm, section thickness 5 mm, scan field of view (FOV) 50 cm, tube current 200 mAs, and at 80 kV were: rotation time 0.5 sec, detector collimation 4 x 10-mm, section thickness 10 mm, scan FOV 50 cm, tube current 250-, 200-, 150-, 100-, 50-, and 30 mAs. We repeated scanning 5 times for each scan parameter setting. The 80-kV images were processed using the XRES filter.

Data Analysis

In the experiments using the phantom harboring a syringe containing different concentrations of iodine solution, we measured the attenuation- and image noise values (standard deviation of the CT number) of the iodine solutions at each kV setting using a circular region of interest (ROI) cursor (= 50 mm^2) on images obtained at 120- and 80 kV. The measured noise values (n = 5) for each scan parameters were averaged. We recorded the radiation dose (CT dose index volume: $CTDI_{volume)}$ (49) that was automatically calculated on the operator console of the CT scanner.

In the experiments with the low-contrast module phantom we measured the noise values (standard deviation of the CT number) of the phantom at the center of the phantom consisted of uniform material using a circular ROI cursor (= 50 mm^2) on images obtained at 120- and 80 kV with an XRES filter. We averaged 5 measured noise values for each scan parameter.

RESULTS

Fig. 2.3. is a scattergram of the relationship between the iodine concentration and the attenuation value (CT number) in the test syringes at each kV setting. There was a strong positive linear correlation between the iodine concentration and the attenuation value at each kV ($r = 0.99$, $p < 0.001$). The iodine attenuation values at 80 kV scan were 1.85 and 1.59 times that at 140- and 120 kV, respectively.

The graph in Fig. 2.4. shows the relationship between the iodine concentration and the image noise measured in test syringes at each kV setting. At 250 mAs, the image noise at all kV settings was almost constant irrespective of the iodine concentration. The mean image noise at 80 kV was 2.82 and 2.29 times that at 140- and 120 kV, respectively.

Fig. 2.5. shows relationship between the radiation dose ($CTDI_{volume}$) and tube current second (mAs) at each kV setting. At each kV setting, there was a strong positive linear correlation between the mAs and the $CTDI_{volume}$ ($r = 0.99$, $p < 0.001$). At identical mAs settings, the radiation dose at 80 kV was 20.6 - 21.8% (mean 20.8%) and 30.5 - 32.2% (mean 30.9%) of that delivered at 120 kV and 140 kV, respectively.

In the low-contrast phantom experiments, the mean image noise at 120 kV and 200 mAs was 3.62 ± 0.03 (SD). The mean image noise at 80 kV and 250-, 200-, 150-,

100-, 50-, and 30 mAs was 2.93 ± 0.05, 3.08 ± 0.09, 3.52 ± 0.07, 4.28 ± 0.12, 6.34 ± 0.15, and 10.11 ± 0.27, respectively (Fig. 2.6.).

DISCUSSION

In general, iodine enhancement on CT images is drastically affected by the tube voltage. The attenuation of iodine increases as the effective energy (keV) decreases because the energies in the x-ray beam move closer to the k-absorption edge of iodine. As shown in Fig. 2.3., there was a significant linear correlation between the CT number and the iodine concentration at a given tube voltage. As the increase was greater at the lower tube voltage setting, the difference in the iodine contrast of each organ is more pronounced than at a setting of 120 kV; this may provide an advantage at contrast-enhanced scanning such as hepatic dynamic CT (50, 51), hepatic perfusion CT, CT angiography (31), and CT urography (52). At those CT examinations, the contrast dose may be reduced by using low kV scanning because the iodine enhancement at 80 kV was 1.59 times that at 120 kV.

Lowering the tube voltage in the low kV scan technique with a given tube current second decreases the amount of transmitted x-rays; this results in an image noise increase that frequently leads to decreased contrast detectability. One solution to compensate for the increase in the image noise on low kV scans is to increase the tube current second. Funama et al. described that a 35% reduction in the radiation dose can be achieved when scanning was performed at 90- rather than 120 kV without

degradation of detectability on low-contrast images (29). Although currently available MDCT scanners can accommodate the higher tube current needed with low tube voltage settings, the tube power is not high enough for the assessment larger patients, thus the applicability of the low tube voltage technique is restricted in these individuals.

Another solution to compensate for the increase in the image noise at low kV scanning is the use of adaptive noise reduction filters. Although the image noise tends to decrease as the smoothing factor increases and image blurring tends to increase with reduced edge enhancement, the filter used in this study simultaneously achieves noise reduction and edge preservation.

In our study, the noise value on processed images acquired with the XRES filter at 80 kV and 150 mAs was comparable to images obtained at 120 kV and 200 mAs. Therefore, we conclude that 80 kV and 150 mAs is appropriate for hepatic perfusion CT scanning described in the Chapter 5.

The adaptive noise reduction filter may be useful at MDCT urography. The primary purpose of CT urography is the identification of filling defects in the urinary tract and the detection of irregularities in the tract contour (53, 54) rather than the detection of low-contrast objects. We found that the internal homogeneity and the sharpness of the contour of the urinary tract was preserved on filtered 80 kV images and

that the quality of the filtered 80 kV images was comparable to images obtained with 120 kV (52). Therefore, we suggest that use of a noise reduction filter is highly effective at MDCT urography performed with a low tube voltage technique.

In conclusion, iodine enhancement and image noise were increased with the low kV scan technique at a given tube current second. Use of the adaptive noise reduction filter mitigated the effects of the image-noise increase.

Chapter 3. Optimization of Contrast Dose for Pancreatic Dynamic MDCT: Patient Body Weight Tailored Contrast Material Injection Protocol versus Fixed Dose Protocol

Contents

ABSTRACT

Purpose: To prospectively compare the effect of a protocol with a fixed contrast injection dose (Protocol 1: P1) and one with a contrast dose tailored to patient body weight (Protocol 2: P2) on pancreatic enhancement at pancreatic dynamic CT.

Methods and Materials: This study was approved by an institutional review committee, and patients gave informed consent. We randomly assigned 78 patients with suspicion of pancreatic tumor to 1 of 2 protocols (of 39 patients in each protocol). In P1, we delivered a fixed contrast dose (120 ml Iohexol-300) at an injection rate of 4.0 ml/sec; in P2 we injected a dose tailored to the patient body weight (BW, 2.0 ml/kg) over the course of 30 sec. Scans were started 25-, 45- (pancreatic parenchymal phase, PPP), and 70 sec (portal venous phase, PVP) after the initiation of contrast injection. Pancreatic enhancement during PPP and hepatic enhancement during PVP were compared using Student's t-test in patients whose BW was less than 60 kg (group A) or 60 kg or more (group B). A radiologist measured CT number of each organ in a blinded fashion for the contrast-injection protocol used.

Results: Under P1, mean pancreatic enhancement during PPP was 94.1 Hounsfield units (HU) in group A, and 76.1 HU in group B; the difference was statistically

significant ($p = 0.02$). Under P2 it was 89.5 HU in group A and 84.7 HU in group B; there was no significant difference ($p = 0.45$). Mean hepatic enhancement during PVP was 59.6 HU in group A- and 48.5 HU in group B patients ($p < 0.01$) under to P1; under P2 it was 55.4 HU in group A, and 58.3 HU in group B, indicating no significant difference ($p = 0.34$).

Conclusion: The patient BW-tailored dose protocol (P2) yielded satisfactory pancreatic and hepatic enhancement irrespective of patient weight.

INTRODUCTION

As multidetector CT (MDCT) offers high volumetric coverage, speed, and spatial resolution, it is now widely used for the acquisition of reliable images for the diagnosis and follow-up of pancreatic tumors. Some pancreatic dynamic CT studies (16-19, 55) emphasized the importance of the pancreatic parenchymal phase (PPP) that occurs 40-70 sec after the start of contrast injection at a rate of 3.0 ml/sec (17, 18). Maximum pancreatic enhancement can be obtained during PPP (17-19) and the detection of pancreatic cancer is maximized during PPP because the cancer is hypo-attenuated compared to the surrounding pancreatic parenchyma. The PPP is also useful for evaluating tumor invasion into the peri-pancreatic arteries and portal vein because these vessels are intensively enhanced during PPP (16-20, 23).

Technique-related factors for contrast enhancement at pancreatic dynamic CT include the scan delay time after the start of contrast injection (16-19), and the dose (56, 57) and concentration of contrast material (56, 58), the injection rate (injection duration) (22, 57), and saline flush after contrast administration (59, 60). In most of these examination protocols the contrast dose is fixed (16-23), although some tailor the contrast dose to the patient body weight (15, 56, 57).

Because the feeding arteries for the pancreas are the branches derived from the abdominal aorta, pancreatic enhancement is presumed to be almost parallel to that of the abdominal aorta. Aortic enhancement is associated with contrast dose per body weight (15). Therefore, protocols using a fixed contrast dose may yield insufficient aortic enhancement in heavy patients. Thus, the purpose of our study was to prospectively compare the effect of a protocol with a fixed contrast injection dose and one with a contrast dose tailored to patient body weight on pancreatic enhancement at pancreatic dynamic CT.

MATERIALS AND METHODS

Our study was approved by our institutional review board. Before obtaining their informed consent to undergo CT examinations and to participate, we explained to all patients the purpose of this study.

Patients

Between July 2005 and April 2006, we enrolled 78 patients (39 men and 39 women, age range 23–91 years, mean age 66.4 years) in this prospective study. Inclusion criteria were (a) suspicion of pancreatic tumors at ultrasonography (US) or elevated tumor marker levels (CA19-9, DUPAN-2, or Elastase-1) and (b) absence of renal failure (serum creatinine > 1.5 mg/dl (114 mol/l)) or absence of a contraindication for iodinated contrast material. All enrolled patients satisfied both criteria. The final diagnosis was intraductal papillary mucinous neoplasm (IPMN) in 10 patients, pancreatic carcinoma in 38, islet cell tumor in 5, mucinous cystic adenoma in 1, serous cystadenoma in 1, and pancreas cyst in 7; 16 patients were proven to be without pancreatic lesions. The diagnosis of 5 patients with IPMN, 30 patients with pancreatic carcinoma, and of all patients with islet cell tumor, mucinous cystic adenoma, and

serous cystadenoma was based on pathological findings at definitive surgery. The diagnosis of 5 patients with IPMN was made by basis of both the follow up CT and blood chemistry evaluation. The diagnosis of 8 patients with pancreatic carcinoma, all patients with pancreatic cysts, and all patients without pancreatic disease was determined by follow up study using US, CT-, or MR imaging, and blood chemistry evaluation. In these patients, range of the follow up duration was 6-14 months and mean follow up duration was 11 months.

The patients were randomly assigned to 1 of 2 protocols; P1 was a fixed contrast-dose protocol, in P2 the contrast dose was tailored to the patient weight; 39 of the 78 patients were assigned to P1 and 39 to P2. The P1 group consisted of 18 men and 21 women ranging in age from 23 to 91 years (mean 64.5 years); their weight ranged from 40 to 88 kg (mean 56.8 kg); 26 patients weighed less than 60 kg (group A) and 13 weighed 60 kg or more (group B). In the P2 group there were 21 men and 18 women ranging from 46 to 85 years (mean 68.2 years); their weight range was 37 to 74 kg (mean 55.0 kg); 22 patients weighed less than 60 kg (group A) and 17 weighed 60 kg or more (group B). We measured patient body weight of each patient just before the CT examinations. There was no statistically significant difference in the distribution

of the age ($p = 0.21$, two-tailed Student's t-test), sex ($p = 0.33$, χ^2-test), and body weight (BW) between the 2 protocols ($p = 0.33$, two-tailed Student's t-test).

Contrast Injection Protocols

The contrast medium was Iohexol (Omnipaque, Daiichi Pharmaceutical Co., Ltd., Tokyo, Japan) containing 300 mg iodine/mL. In all patients the contrast medium was administered with a mechanical power injector (Dual Shot; Nemoto-Kyorindo, Tokyo, Japan) through a 20-gauge cannula inserted into an antecubital vein. P1 patients received a total of 36 g of iodine (120 mL contrast medium at 300 mg iodine/mL). In P2 patients, the contrast dose was tailored to their BW; they received 600 mg of iodine/kg (2.0 mL contrast/kg BW). Yamashita et al (15) reported that when dose was tailored to patient weight, the use of 2.0 or 2.5 ml/kg of intravenous contrast material produced better results for abdominal dynamic CT than did 1.5 ml/kg. According to this report, we adopted the 2.0 ml/kg for contrast dose which was tailored to patient weight.

As the average BW in the Japanese population is approximately 60 kg (61), patients weighing 60 kg received 36 g of iodine, a concentration identical to that in P1. In all patients the contrast medium was injected over 30 seconds. Therefore, the

injection rate was a constant 4 mL/sec under P1; in P2 it varied from 2.5 mL/sec (37 kg) to 4.9 mL/sec (80 kg). After contrast injection, all patients were injected with 30 mL of saline solution delivered at the same rate as the contrast medium.

Scan Protocol

All patients were scanned using a 40–detector CT scanner (Brilliance-40; Philips Medical Systems, Cleveland, Ohio); the parameters were rotation time, 0.5-sec; detector collimation, 40 x 1.5-mm; helical pitch, 0.7; gantry rotation time, 0.5-sec; reconstructed section thickness and interval, 3.0-mm; tube voltage, 120 kV; and tube current-time product, 300 mAs. Image reconstruction was in a 25–35-cm display field of view depending on the patient's physique. All scans were started at the top of the liver to the lower pole of the kidney in a cephalocaudal direction. Patients were instructed to hold their breath, with tidal inspiration during scanning. Unenhanced and three-phase contrast-enhanced helical scans of the whole liver were obtained. In both protocols, first-, second-, and third phase scans were started 25-, 45-, and 70 sec after the inception of contrast injection; the phases corresponded to the arterial phase, the pancreatic parenchymal phase (PPP), and the portal venous phase (PVP), respectively. The scans

were the same as those acquired by pancreatic dynamic CT in our routine clinical practice.

Quantitative Assessment

All numerical data are presented as the mean ± standard deviation (SD). Because the PPP reportedly provides the best tumor contrast and good opacification of the peripancreatic arteries and portal vein, and the PVP is adequate for the detection of liver metastases (18, 62), we measured the enhancement values of the pancreas, celiac artery, and portal vein during PPP and those of the liver during PVP. We also determined enhancement of the celiac artery during the arterial phase. For each protocol we compared the mean enhancement values of the pancreas, celiac artery, liver, and portal vein obtained in the 2 body weight (BW) groups, i.e. in patients weighing less than 60 kg (group A) and those with a BW equal to or more than 60 kg (group B).

The enhancement values during PPP and PVP were measured by placing a manually-defined ROI on the pancreas, liver, celiac artery, and portal vein. These procedures were carried out by a board-certified radiologist (Y.Y.) with 10 years of experience in abdominal CT imaging. She was blinded to the specific protocol used and the group each patient was in P1 or P2.

In the pancreas, attenuation was measured in the head, body, and tail, and all attenuation values were averaged. An attempt was made to maintain a constant ROI area of approximately 50 mm^2. The actual ROI area ranged from 30 to 60 mm^2. Visible blood vessels, the pancreatic duct, tumor, cystic lesion, calcification, and artifacts were carefully excluded from ROI measurements in the pancreatic parenchyma. Contrast enhancement in HU of the pancreatic parenchyma during PPP was calculated as the absolute difference in the attenuation values of the pancreas on unenhanced- and PPP scans.

To measure enhancement of the celiac artery, an attempt was made to maintain a constant ROI area of approximately 15 mm^2. The actual ROI area ranged from 12 to 17 mm^2. Enhancement of the celiac artery in the arterial phase and PPP was calculated as the absolute difference in the attenuation values of the celiac artery on unenhanced scans and on scans obtained during the aortic phase or PPP.

Liver attenuation was measured in 3 areas, i.e. the left lobe and the anterior- and posterior segment of the right lobe on images obtained at the level of the main portal vein; all attenuation values were averaged. An attempt was made to maintain a constant ROI area of approximately 150 mm^2. The actual ROI area ranged from 80 to 200 mm^2. Visible blood vessels, bile ducts, and artifacts were carefully excluded from

ROI measurements in the hepatic parenchyma. Contrast enhancement in the hepatic parenchyma during PVP was calculated as the absolute difference in the attenuation values of the liver on unenhanced- and PVP scans.

We also measured the attenuation values of the main portal vein during PPP. We attempted to maintain a constant ROI area of approximately 50 mm^2; the actual ROI area ranged from 40 to 60 mm^2. Contrast enhancement in the main portal vein during PPP was calculated as the absolute difference in the attenuation values of the main portal vein on unenhanced- and PPP scans.

Qualitative Assessment

Two board-certified radiologists (K.A. and Y.N.) with 20 and 12 years of experience independently performed visual evaluation of the quality of pancreatic enhancement. They specialized in body-imaging and read abdominal CT on a regular basis and they were blinded to the contrast-injection protocol used.

We prepared a 4-point imaging scale to record image quality (Fig. 3.1). Grade 1 images were regarded as poor (no pancreas enhancement), grade 2 was assigned to images judged as fair (despite slight pancreatic enhancement, the image is diagnostically inadequate), grade 3 to images with adequate pancreatic enhancement,

and grade 4 to images judged to be excellent. If the readers disagreed about the quality of enhancement, the images were reevaluated for consensus.

Statistical Analysis

We used the two-tailed Student t-test to evaluate differences between P1 and P2 with respect to pancreatic enhancement during PPP and to assess differences in the enhancement of the pancreas, celiac artery, liver, and portal vein in the 2 body weight groups subjected to the 2 different protocols. The Mann-Whitney U-test was used to compare the quality of images obtained in the 2 body weight groups subjected to the different protocols. Furthermore, we performed a generalized estimating equation (GEE) analysis (63) for the evaluation of enhancement of the celiac artery because we measured it during the both the arterial and pancreatic parenchymal phases and enhancement of the celiac artery during these 2 phases may correlate each other. GEE, in particular, was focusing on the effect of patient body weight on the enhancement of the celiac artery and GEE was performed for protocols 1 and 2, independently.

The sample size was obtained as follows: the primary variable was pancreatic enhancement during the pancreatic parenchymal phase and anticipated effect size d (difference of means/standard deviation) was estimated 1.3 from a result of the

preliminary study conducted before this study. The sample size was based on a two-tailed t-test with significant level of 0.05, a power level of 0.90. The required sample size was 13 in each group for a total of 26.

To assess the degree of observer agreement for the quality of depiction of the pancreatic enhancement, we used the Cohen κ coefficient. The scale for the κ coefficients for interobserver agreement was as follows: less than 0.20, poor; 0.21–0.40, fair; 0.41–0.60, moderate; 0.61–0.80, substantial; and 0.81–1.00, almost perfect. Statistical analyses were performed with a statistical software package (SPSS, version 15.0, SPSS Inc. Chicago, IL). For all statistical analyses, a p value less than 0.05 was considered to indicate a significant difference. Sample size was calculated with statistical software (Sample Power, version 2.0, SPSS Inc. Chicago, IL).

RESULTS

Pancreatic enhancement during the PPP *(Fig. 3.2.)*

Under P1, mean pancreatic enhancement for all patients was 89.0 HU ± 24.4; under P2 it was 87.2 HU ± 19.1; the difference was not statistically significant ($p = 0.54$). Under P1 it was 94.1 HU ± 24.3 (range, 61.3–140.7 HU) for group A and 76.1 HU ± 19.0 (35.3–109.3) for group B; the difference was statistically significant at $p = 0.02$. Under P2, mean pancreatic enhancement was 89.5 HU ± 19.4 (51.3–138.7) and 84.7 HU ± 19.5 (37.3–110.3) in group A and B, respectively; the difference was not statistically significant ($p = 0.45$).

Enhancement of the celiac artery during the arterial and pancreatic parenchymal phase *(Fig. 3.3.)*

During the arterial phase, under P1, mean enhancement was 283.9 HU ± 56.2 (207.3–395.5) in group A and 235.3 HU ± 29.6 (190.1–294.4) in group B; the difference was statistically significant ($p < 0.01$). Under P2, it was 268.0 HU ± 59.0 (155.6–372.4) and 291.1 HU ± 31.0 (251.5–367.5) in group A and B, respectively; the difference was not statistically significant ($p = 0.21$).

During the PPP, under P1, mean enhancement was 188.1 HU ± 90.0 (94.8–420.7) in group A and 168.8 HU ± 81.4 (99.7–396.8) in group B; the difference was not statistically significant ($p = 0.64$). Likewise, there was no statistically significant difference under P2; enhancement was 189.0 HU ± 76.5 (109.9–384.0) and 204.1 HU ± 89.0 (117.7–396.1) in groups A and B, respectively ($p = 0.59$).

In the analysis of the effect of patient body weight on the enhancement of the celiac artery by GEE, there was statistically significant correlation between the aortic enhancement and patient body weight in both the protocols 1 and 2 ($p < 0.01$, $p < 0.01$).

Hepatic enhancement during PVP *(Fig 3.4.)*

Mean hepatic enhancement for all patients was 55.9 HU ± 12.3 and 56.7 HU ± 9.5 under P1 and P2, respectively and the difference was not statistically significant ($p = 0.75$). Under P1, it was 59.6 HU ± 12.8 (45.3–93.0) in group A and 48.5 HU ± 6.8 (39.0–59.3) in group B. The difference was statistically significant ($p < 0.01$). Under P2, mean hepatic enhancement was 55.4 HU ± 10.5 (36.7–79.0) in group A and 58.3 HU ± 7.9 (46.7–76.3) in group B; the difference was not statistically significant ($p = 0.34$).

Portal venous enhancement during PPP *(Fig. 3.5.)*

Under P1 and P2, mean portal venous enhancement for all patients was 120.4 HU ± 21.8 and 124.5 HU ± 14.4, respectively; the difference was not statistically significant ($p = 0.32$). With P1, it was 193.8 HU ± 46.9 (50.7–282.7) in group A and 139.9 HU ± 34.8 (88.7–206.0) in group B and the difference was statistically significant ($p < 0.01$). Under P2, the difference was not significant ($p = 0.24$); mean portal venous enhancement was 180.4 HU ± 31.4 (117.7–269.0) and 168.6 HU ± 29.8 (111.7–221.0) in groups A and B, respectively.

Qualitative Assessment

Under P1, 21 of 26 (80.8%) images from group A patients were judged to be excellent; the remaining images were graded as adequate (Table 3.1.). The majority of images (8/13, 61.5%) obtained in group B showed good enhancement. Under P1, pancreatic enhancement was significantly better in patients weighing less than 60 kg (group A) than in heavier patients ($p < 0.01$). Under P2, there was no statistically significant difference between the 2 body weight groups; the images of 19 of 22 group A- (86.4%) and 13 of 17 group B patients (76.5%) showed excellent pancreatic enhancement ($p = 0.43$).

There was good interobserver agreement for the quality of depiction of the pancreatic enhancement (κ = 0.69).

The population mean for grade 4 and 3 was 129.6 HU ± 23.0 and 99.0 HU ± 21.4, respectively (Table 3.2.). As grade 2 was assigned to only 2 images, and none of the scans were categorized as poor, we did not calculate these values for this set of images.

DISCUSSION

Under the fixed contrast dose protocol (P1), pancreatic enhancement during PPP was significantly worse in the heavier- (body weight equal or more than 60kg, group B) than the lighter patients (body weight less than 60kg, group A). On the other hand, under the protocol that tailored the contrast dose to patient weight (P2), there was no statistically significant difference between the 2 weight groups. Qualitative evaluation of the images indicated that among lighter weight groups (group A), the readers judged 80.8% of the images acquired with P1 and 86.4% of those obtained with P2 to show excellent pancreatic enhancement. On the other hand, in the heavier weight groups (group B), only 23.1% of patients with P1 were graded as excellent, although 76.5 % of patients with P2 were graded as excellent. This suggests that at pancreatic dynamic CT, fixed-dose protocols do not, while weight-adjusted protocols do, yield diagnostically satisfactory pancreatic enhancement in heavier patients.

Under P2 (contrast dose 2.0 mL/kg), mean pancreatic enhancement during PPP for all patients was 87.1 HU. Others reported mean pancreatic enhancement to be 84.0-93.6 HU when a fixed dose of 140–150 mL was injected at 4.0–5.0 mL/sec (22, 64). Direct comparison of their and our results is difficult because the attenuation value of organs is affected by the effective tube voltage of the CT equipment used, even

if the blood iodine concentration is similar (29, 30). However, our results suggest that a weight-tailored contrast injection protocol, e.g. 2.0 mL/kg, yields pancreatic enhancement similar to that achieved with protocols using a fixed contrast dose of 140–150 mL.

Our findings suggest that as P2 yields better enhancement of the celiac artery during the arterial phase in patients of greater body weight. Therefore, the BW-tailored contrast dose protocol is preferable in this group for CT angiography of the peripancreatic arteries (65) .

Mean hepatic enhancement during PVP exceeded 50 HU in all patients subjected to P2 and in lighter patients subjected to P1. In the heavier patient group, P1 yielded lower enhancement (48.5 HU). Walkey (66) suggested that 50 HU enhancement was the lowest threshold for the visualization of hepatic lesions with low attenuation. Similarly, Brink et al. (11) reported 50 HU during PVP as the minimum enhancement value required of contrast injection protocols used at hepatic dynamic CT. Based on these considerations we suggest that, especially in heavier patients, the weight-tailored contrast injection protocol should be used to assure sufficient hepatic enhancement at dynamic CT.

Under P1 we injected 120 mL of contrast material, a dose lower than that used by others (140–150 mL) (17-20, 22, 23, 64, 67), because the mean weight of Japanese, at around 60 kg (61), is lower than the BW of patients in those studies. In our study, the contrast dose delivered in group A under P1 was approximately 2.0 mL/kg, set to correspond with the per kg dose used under P2. We are aware that, although appropriate in Japanese patients, injection doses of 120 mL may be too low in Westerners.

We delivered a saline flush after the administration of contrast material. Schoellnast et al. (12) reported a saline flush statistically significantly improved enhancement of the liver, pancreas, portal vein, and abdominal aorta at contrast-enhanced abdominal MDCT. It is possible that a contrast dose of 2.0 mL/kg patient BW may be too low unless contrast administration is followed by a saline flush.

In P1, the contrast medium (120 mL) was delivered at 4.0 mL/sec resulting in a 30-sec delivery time; in P2, the injection duration was fixed at 30 sec. The prevalent method for contrast delivery at pancreatic dynamic CT is to choose a fixed injection rate. Awai et al. (68) reported that variations in aortic peak times and aortic peak enhancement values are reduced with injection protocols that employ fixed duration times and adjust the contrast dose to the patient weight. Because the feeding arteries

to the pancreas are branches derived from the abdominal aorta, enhancement of the pancreas and the abdominal aorta can be expected to occur almost simultaneously. We postulate that injection protocols with doses tailored to the patient weight and fixed injection duration may help to reduce variations in pancreatic enhancement.

Under P1, we used protocol with a fixed contrast dose at an injection rate of 4.0 ml/sec. We consider that the faster injection rate may increase the risk of extravasation of contrast material, though previous study reported that there was no extravasation of contrast material or any systemic disorders by using injection with high flow rate of 8 ml/sec (69).

There were some potential limitations in our study. First, as the weight range and the mean BW of our study population is smaller than in Westerners, the applicability of our results to populations of greater BW needs to be verified. Second, although our results suggest that it may be possible to reduce variations in pancreatic enhancement by using injection protocols that tailor the contrast dose to the patient weight and apply a fixed injection duration, the optimum injection duration remains to be determined.

In conclusion, our results suggest that protocols that deliver a contrast dose tailored to the patient weight at a fixed injection duration yield satisfactory pancreatic enhancement in patients of different body weights.

Chapter 4. Optimal Contrast Dose for Depiction of Hypervascular Hepatocellular Carcinoma at Dynamic MDCT

Contents

ABSTRACT

Purpose: To investigate prospectively the optimal contrast dose for the depiction of hypervascular hepatocellular carcinoma (HCC) during the hepatic arterial phase (AP) at dynamic CT using a 64-detector CT scanner.

Materials and Methods: The study included 135 patients with known or suspected HCC; all underwent dynamic CT on a 64-detector scanner and 47 were found to have 71 hypervascular HCCs. The patients were randomly assigned to 3 protocols; a contrast dose of 450-, 525-, and 600 mgI per kg weight (BW) was delivered over 30 sec in protocols A, -B, and -C, respectively. We measured the tumor-liver contrast (TLC) during AP in the 3 groups and compared the results. Two radiologists qualitatively evaluated tumor conspicuity during AP using a 3-point scale; their results were compared t.

Results: The TLC in protocols A, B, and C was 27, 38, and 52 HU, respectively; the difference was significant between protocols A and B ($p = 0.05$), A and C ($p < 0.01$), and B and C ($p = 0.02$). In our qualitative analysis of tumor conspicuity the mean score for protocols A, B, and C was 1.6, 2.3, and 2.7, respectively; there was a

significant difference between protocols A and B and A and C, but not between B and C.

Conclusion: The Administration of a total iodine dose of 525 mg or more per kg BW is desirable for the good or excellent depiction of hypervascular HCC although the administration of 450 mgI per kg BW can depict hypervascular HCC.

INTRODUCION

As most hepatocellular carcinomas (HCCs) are fed by the hepatic artery, one of the branches from the abdominal aorta, they are demonstrated as hyperattenuated tumors during the hepatic arterial phase (HAP) of hepatic dynamic CT (9, 10, 70). Possible technical factors relating to contrast administration that contribute to the depiction of HCC during HAP at hepatic dynamic CT include the scan delay-time after the start of contrast injection, the total iodine dose, the contrast concentration, and the injection rate (injection duration). Among these technical factors, the scan delay-time (71-76, 77), injection rate (10, 68, 78-81) , and contrast material concentration (82-87) have been well-studied since the advent of single- or multi-detector helical CT. However, to our knowledge, there are only few reports regarding the optimal contrast dose during HAP at abdominal dynamic CT (15, 80) and although their authors described enhancement of the liver parenchyma and the abdominal aorta during HAP at various contrast doses, they did not analyze the conspicuity of the liver tumors. Furthermore, hypervascular HCCs often appear isodense compared with the surrounding liver, therefore, portal venous-phase (PVP) helical CT scans are of limited value for the detection of hypervascular HCCs (9, 10). As the major role of hepatic dynamic CT that includes the HAP is the detection of hypervascular hepatic tumors, the

conspicuity of the liver tumors during the HAP, which can be expressed by the attenuation difference between the tumor and the hepatic parenchyma (3), is important. Therefore, we should investigate the contrast dose necessary for hepatic dynamic CT scans from the standpoint of tumor conspicuity. The purpose of our study was to examine the effect of the contrast dose on the conspicuity of hypervascular tumors during HAP at hepatic dynamic CT using a 64-detector CT scanner.

MATERIALS AND METHODS

This prospective study received institutional review board approval; written informed consent to participate was obtained from all patients.

Patients and Tumors

Between July and December 2006, we enrolled 145 patients who met our inclusion criteria. These were (*a*) a diagnosis of type B, C, or alcoholic hepatitis; (*b*) confirmed HCC untreated during the 3 months preceding the current CT study, the presence of a suspected space-occupying hepatic lesion based on sonographic study, or elevated levels of tumor markers (α-fetoprotein, protein induced by the absence of vitamin K, or antagonist-II); and (*c*) the absence of both renal failure (serum creatinine < 1.5 mg/dL) and a contraindication for iodinated contrast material.

Ten of the 145 patients were subsequently excluded, 3 because of tumor thrombi in the central portal veins, 4 because numerous tumors involving the entire liver may have changed the hepatic hemodynamics, and 3 because they harbored tumors larger than 5.0 cm that may also have altered the hepatic hemodynamics.

Thus, the final study population consisted of 135 patients, 97 men and 38 women aged 35–85 years (mean 66.1 years). In the men the age range was 35–85 years (mean 65.4 years); in the women it was 39–82 years (mean 67.9 years). There was no significant age difference between the male and female patients ($p = 0.17$, two-tailed Student *t* test). The mean body weight for all patients was 58.7 ± 9.2 kg (standard deviation [SD]); the range was 34–80 kg.

As the mean CT number of the normal liver parenchyma is about 60 HU on unenhanced images and about 80 HU during HAP (68), we defined as hypervascular tumors whose CT number during HAP was 25 HU greater than on unenhanced scans. Of the 135 patients, 47 (39 men, 8 women; age range 48–85 years; mean age 70.2 years) had solitary or multiple hypervascular HCC nodules ($n = 71$). The definitive diagnosis of hypervascular HCC was based on the following findings: histopathologic evidence after hepatic surgery ($n = 13$); needle biopsy results ($n = 10$); substantially increased levels of α-fetoprotein, protein induced by vitamin K absence, or antagonist-II with follow-up dynamic CT demonstrating an increase in tumor size within 3 months ($n = 24$). All patients who had histological evidence and 20 of 24 (83 %) without histologically confirmed hypervascular HCC patients who did not had histological evidence underwent CT during hepatic arteriography (CTHA). Two board-certified

radiologists (K.A. and T.N. with 21- and 9 years of experience with liver CT, respectively), consensually confirmed the presence of hypervascular tumors on CTHA in these patients. At our institution, we routinely subject all patients with HCCs to CTHA and CT portography before starting treatments.

CT Scanning- and Contrast Material Infusion Protocols

All patients were scanned with a 64-detector CT scanner (Brilliance-64; Philips Medical Systems, Cleveland, OH) at the following settings: rotation time, 0.5 second; beam collimation, 64 x 0.625 mm; section thickness and intervals, 5.0 mm; helical pitch (beam pitch), 0.798; table movement, 63.8 mm; scan field of view, (FOV) 40 cm; voltage, 120 kV; tube current, 250–300 mAs. Image reconstruction was performed in a 25–35-cm display FOV depending on the patient's physique. All helical studies were started at the top of the liver in a cephalocaudal direction and unenhanced and 3-phase contrast-enhanced helical scans of the entire liver were obtained. Patients were instructed to hold their breath with tidal inspiration during scanning. Three-phase contrast-enhanced CT scanning of the liver was performed during the hepatic arterial- and portal venous phase (HAP, PVP), and the equilibrium phases. An automatic bolus-tracking program (Bolus Pro Ultra; Philips Medical Systems) was used to time

the start of scanning for each phase after contrast injection. The CT number was monitored by 3 radiology technologists with 3-, 12-, and 22 years of experience with abdominal CT. Monitoring was at the L1 vertebral body level; the region-of-interest (ROI) cursor (0.8–2.0 cm^2) was placed in the abdominal aorta. Real-time, low-dose (120 kVp, 15 mAs) serial monitoring studies began 8 sec after the start of contrast injection. The trigger threshold level was set at 150 HU. During the real-time low-dose serial monitoring studies, the patients were instructed to take shallow, regular breaths. The trigger time in protocols A, B, and C was 19.8 ± 4.2 sec (range 13–29 sec), 18.8 ± 2.5 sec (range 14–26 sec), and 18.2 ± 3.0 sec (range 13–26 sec), respectively. HAP-, PVP-, and equilibrium-phase scanning were started 18-, 40-, and 160 sec after triggering. We based our selection of the scan delay for HAP on a recent paper that described the optimal scan delay for hypervascular HCCs during HAP at hepatic dynamic CT (77). Consequently, the mean scan times for HAP and PVP were 37.8 sec (range 31–47 sec) and 59.8 sec (range 53–69 sec) in protocol A; 36.8 sec (range 32–44 sec) and 58.8 sec (range 54–66 sec) in protocol B; and 36.2 sec (range 31–44 sec) and 58.2 sec (range 53–66 sec) in protocol C.

Patients were randomly assigned to 3 contrast injection protocols; the contrast dose was 450 mg iodine per kg patient body weight in protocol A, 525 mgI per kg in

protocol B, and 600 mgI per kg in protocol C. Yamashita et al. (15) who administered 1.5-, 2.0-, or 2.5 mL/kg or a fixed dose (100 mL) of iopamidol-300 to patients who underwent hepatic dynamic CT, performed a quantitative and qualitative evaluation of the enhancement of the aorta, portal vein, liver, and pancreas. They found that arterial enhancement did not differ between the 2.0 mL/kg, and the 2.5 mL/kg group. Contrast doses of 1.5 and 2.0 mL/kg correspond to 450 and 600 mg iodine per kg patient body weight. The contrast dose used in this study was based on the results of Yamashita et al.; the injection duration was 30 sec in all protocols. Consequently, the contrast injection rate was different in each patient. The mean injection rate in protocols A, B, and C was 3.0 mL/sec (range 2.1–3.9 mL/sec), 3.4 mL/sec (range 2.5–4.4 mL/sec), and 3.9 mL/sec (range 2.3–5.3 mL/sec). The mean injection volumes in protocols A, B, and C were 88.8 mL (range 63–117 mL), 101.9 mL (range 75.3–131.3 mL), and 117.4 mL (range 68–160 mL), respectively.

Among the 3 patient groups there were no significant differences with respect to age or weight ($p = 0.45$ and 0.89, respectively, by one-way analysis of variance [ANOVA]), sex distribution, the number of patients with HCCs ($p = 0.46$ and 0.99, respectively, by the χ^2 test), or the size of HCC nodules ($p = 0.21$, by one-way ANOVA) (Table 4.1.). Iopamidol (Iopamiron; Nihon Schering, Osaka, Japan) with an

iodine concentration of 300 mg/mL was administered using a power injector (Dual Shot; Nemoto Kyorindo, Tokyo, Japan) and a 20-gauge intravenous catheter inserted into an antecubital vein. The delivery of contrast material was followed by flushing with 30 mL of physiologic saline at the same injection rate.

Quantitative Analysis

One radiologist (Y.Y.) with 10 years of experience with liver CT and blinded to the protocol used, measured the mean attenuation values of the abdominal aorta and hepatic parenchyma with a circular ROI cursor. Attempts were made to maintain a constant ROI area of approximately 1.0 cm^2; the range of the ROI areas was 0.5–1.3 cm^2. Aortic attenuation values were determined on 3 consecutive images at the level of the main portal vein during unenhanced- and HAP scanning in all 135 patients. The measured attenuation values obtained for each phase were averaged. Contrast enhancement in the abdominal aorta during HAP was calculated as the absolute difference in aortic attenuation (in Hounsfield units, HU) between unenhanced- and HAP scans.

Hepatic attenuation was measured in 3 separate areas (the left lobe of the liver and anterior and posterior segments of the right lobe) on images obtained at the level of the main portal vein during unenhanced-, HAP-, and PVP studies in all 135 patients. The attenuation values for each phase were averaged. An attempt was made to maintain a constant ROI area of approximately 2 cm^2; the range of ROI areas was 0.8–2.0 cm^2. Visible blood vessels, bile ducts, and artifacts were carefully excluded from ROI measurements in the hepatic parenchyma. Contrast enhancement in the parenchyma was calculated as the absolute difference in the attenuation value of the liver (in HU) on unenhanced- and HAP- or PVP scans.

The conspicuity of a hepatic tumor can be expressed by the attenuation difference between it and the hepatic parenchyma, the so-called tumor-liver-contrast (TLC) (3). We defined the TLC as the result obtained by subtracting the parenchymal attenuation value from the attenuation value of the hepatic tumor. In the 47 patients with hypervascular HCC, the same radiologist (Y.Y.) also determined the TLC for each phase of contrast-enhanced scanning. Tumor attenuation was assessed in the most enhanced portion of the tumor. An attempt was made to maintain an ROI area of approximately 0.5 cm^2; the range of the ROI areas was 0.3–0.5 cm^2. To obtain the parenchymal attenuation value used for TLC calculations, we measured the normal

hepatic parenchyma at least 1 cm from the edge of the tumor to nullify the risk of encountering fibrosis (88). An attempt was made to maintain a constant ROI area of approximately 2 cm^2; the range of ROI areas was 0.8–2.0 cm^2. In patients with fewer than 3 tumors we calculated the mean TLC for all tumors; in patients with 3 or more tumors we used the averaged TLC of the 3 largest tumors.

Qualitative Evaluation

To investigate the relationship between subjectively determined tumor conspicuity and the TLC during HAP, 2 radiologists (K.A. and T.N.) with 21- and 10 years of experience with liver CT, respectively, performed independent visual assessments of the hypervascular HCCs. In patients with 2 or more tumors they assessed the conspicuity of the largest tumor. They used a 3-point scale to classify tumor conspicuity where grade 1 = poor (tumor barely demonstrated), grade 2 = fair (tumor is demonstrated but not as clear as grade 3, and grade 3 = excellent (tumor clearly demonstrated and presence of tumor can be mentioned with confidence). After their independent evaluation, they assigned a grade by consensus.

All images were reviewed in random order on a liquid crystal display (LCD) monitor with a spatial resolution of 1600 x 1200 (Radiforce R22; Eizo, Ishikawa, Japan) using our picture archiving and communications system (View R, version 1.0; Yokogawa Electric, Tokyo, Japan). The preset window level (50 HU) and window width (300 HU) could be changed at will.

Statistical Analysis

Contrast enhancement values in the aorta, hepatic parenchyma, and TLC are reported as the mean ± SD.

We used one-way analysis of variance (ANOVA) to investigate intergroup differences among the 3 protocols with respect to aortic-, hepatic-, and portal vein enhancement and TLC values. When the overall differences were statistically significant, post-hoc analysis was performed using the Tukey-Kramer test for multiple comparisons among the 3 protocols.

The Kruskal-Wallis test was applied to examine intergroup differences for tumor conspicuity among the 3 protocols. When the overall differences were statistically significant, post-hoc analysis was performed using the Steel-Dwass test for multiple comparisons among the 3 protocols.

To estimate the 95% confidence interval (CI) of the population mean for TLC during HAP for each visual grade we applied t-statistics. Interobserver variability between the 2 radiologists in their visual analysis of tumor conspicuity was assessed by the κ test of concordance to measure their degree of agreement. The scale for the κ coefficients for interobserver agreement was: less than 0.20 = poor, 0.21–0.40 = fair, 0.41–0.60 = moderate, 0.61–0.80 = substantial, and 0.81–1.00 = almost perfect (89).

P values of less than 0.05 were considered to indicate statistically significant differences. Statistical analysis except the Steel-Dwass test was with a statistical software package (SPSS, version 15.0; SPSS, Chicago, IL). The Steel-Dwass test was performed on the statistical WEB site (MEPHAS, http://www.gen-info.osaka-u.ac.jp/testdocs/tomocom/).

RESULTS

Aortic- and hepatic enhancement, and TLC during HAP

The mean values for aortic enhancement were 224.5 ± 50.3, 264.4 ± 47.3, and 291.0 ± 42.7 HU for protocols A, B, and C, respectively, and the overall difference among the 3 groups was statistically significant ($p < 0.01$) as was the difference between protocols A and B ($p < 0.01$), A and C ($p < 0.01$), and B and C ($p = 0.02$) (Fig. 4.1.).

The mean values for hepatic enhancement were 15.9 ± 8.1, 17.1 ± 8.5, and 17.6 ± 9.3 HU, respectively, for protocols A, B, and C and there was no overall difference among the 3 protocols ($p = 0.63$).

The mean values for TLC in protocols A, B, and C were 26.5 ± 8.3, 38.4 ± 8.6, and 52.3 ± 20.3 HU, respectively and the overall difference among the 3 groups was statistically significant ($p < 0.01$). We found a significant difference between protocols A and B ($p = 0.05$), A and C ($p < 0.01$), and B and C ($p = 0.02$) (Fig. 4.2.).

Hepatic enhancement and TLC during PVP

The mean values for hepatic enhancement were 43.2 ± 8.7, 48.7 ± 9.1, and 53.9 ± 10.2 HU, respectively, for protocols A, B, and C and the overall difference among the

3 groups was statistically significant ($p < 0.01$). There were statistically significant differences between protocols A and B ($p = 0.02$), A and C ($p = 0.01$), and B and C ($p = 0.02$) (Fig. 4.3.).

The mean values for TLC in protocols A, B, and C were -1.5 ± 7.2, -2.3 ± 12.9, and -3.9 ± 14.0 HU, respectively; the overall difference among the 3 groups was not statistically significant ($p = 0.85$).

Results of visual analysis of tumor conspicuity during HAP

Based on our quantitative analysis of tumor conspicuity during HAP, of the 47 hypervascular tumors, 10 were categorized as grade 1, 17 as grade 2, and 20 as grade 3. The mean TLC was 21.3 ± 5.3 HU (95% CI: 17.3 HU, 25.0 HU), 35.6 ± 2.7 HU (34.2 HU, 36.9 HU), and 53.2 ± 16.7 HU (45.4 HU, 61.0 HU) for grades 1, 2, and 3, respectively (Table 4.2.). The mean score for tumor conspicuity in protocols A, B, and C was 1.6, 2.3, and 2.7, respectively and the overall difference among the 3 groups was statistically significant ($p < 0.01$). While there was no statistically significant difference between protocols B and C ($p = 0.22$), there was a significant difference between protocols A and B ($p = 0.02$), and A and C ($p < 0.01$) (Fig. 4.4.).

An HCC conspicuity score of 2 or 3 was assigned to 8 of 16 (50.0 %) protocol A-, 13 of 15 (86.7%) protocol B-, and all 16 (100 %) protocol C patients. Lastly, there was good interobserver agreement for the degree of tumor conspicuity (κ = 0.73).

Representative cases for each protocol are shown in Fig. 4.5..

DISCUSSION

In our quantitative analysis, TLC increased in the order protocol A (450 mgI/kg), B (525 mgI/kg), and C (600 mgI/kg) during HAP, and there was a statistically significant difference between protocols A and B, B and C, and A and C. In our qualitative analysis of tumor conspicuity during HAP, there was no statistically significant difference between protocols B and C, however, there was a significant difference between protocols A and B. Based on our results, we concluded that at least 525 mg iodine per kg BW should be administered for the good or excellent depiction of hypervascular HCC during HAP. Furthermore, although 87% of protocol B patients received a score of 2 or 3 for tumor conspicuity, all patients subjected to protocol C had a score of 2 or 3. Therefore, we recommend the administration of 600 mgI per kg BW to further improve the depiction of HCC.

In previously reported hepatic dynamic CT studies the contrast injection protocols involved fixed doses (72, 75, 90-93) or doses adjusted to the patient weight (10, 73, 74, 76, 80-85, 94). However, it remains to be undetermined which type of contrast injection protocol is best for hepatic dynamic CT. As hypervascular HCCs are usually fed by the hepatic artery, one of the branches from the abdominal aorta, theoretically, their enhancement is correlated with aortic enhancement during HAP. In fact, Yanaga

et al. (51) recently reported that the TLC of hypervascular HCCs is almost proportional to aortic enhancement. On the other hand, in phantom experiments, we observed that at a given injection duration, aortic enhancement increased linearly with the administered contrast dose (24). Thus, we concluded that the contrast dose should be determined according to the patient weight at hepatic dynamic CT for the demonstration of hypervascular HCCs. Yamashita et al. (15), who performed a prospective randomized study to evaluate the optimal contrast dose to achieve adequate aortic and pancreatic enhancement at abdominal dynamic CT, also suggested that the contrast dose be tailored to the patient weight.

PVP images are important for the detection of hypovascular HCC as these lesions may be best demonstrated during this phase (70). Hepatic enhancement of 50 HU requires 521 mg of iodine per kg BW (14); this iodine dose corresponds to 1.73 mL/kg of contrast material with an iodine concentration of 300 mg I/mL and is very similar to the contrast dose in protocol B (1.75 mL/kg). Mean hepatic enhancement in protocols B and C was 48.7 and 53.9 HU, respectively. As this level of hepatic enhancement sufficed for diagnosing hypovascular hepatic tumors, the contrast dose in protocols B and C might be adequate for the diagnosis of these tumors during PVP, although we did not validated contrast dose of 525 mg or more is appropriate for

hypovascular tumor in this study. However, the PVP is not useful for the demonstration of hypervascular HCC because the TLC is minimized during this phase (9, 10). In fact, the attenuation values between the tumors and the liver parenchyma during PVP differed by less than 5 HU in all the protocols examined in the current study. In general, aortic enhancement increases as the injection rate increases at given contrast doses (78). In our study, we determine contrast dose according to the patient weight and adopted a fixed injection duration (30 sec). Therefore, the injection rate varied even among individuals treated under the same contrast injection protocol. Awai et al. reported (68) that variations in aortic peak times and aortic peak enhancement values were reduced with injection protocols that used fixed duration times and adjusted the contrast dose to the patient weight. As hypervascular HCCs are usually fed by branches from the aorta, theoretically, their enhancement may be almost constant in contrast injection protocols with fixed duration and adjust the contrast dose to the patient weight. We believed that contrast injection protocols with fixed duration and adjust the contrast dose to the patient weight, which we adopted in our study, was effective for evaluation of effect of contrast dose on depiction of the hypervascluar HCCs.

The results presented here apply only to hepatic dynamic CT with injection duration of 30 sec. If the contrast dose is constant, aortic enhancement increases as the injection duration becomes shorter, in other words, the injection rate increases (78). Therefore, lower contrast doses delivered at shorter injection duration may yield aortic enhancement and tumor conspicuity similar to those in the current study. On the other hand, the rate of increase of hepatic peak enhancement is very small at injection rates greater than 2.0 mL/sec, although hepatic peak enhancement increases with the injection rate at a given contrast dose (78). Consequently, the delivery of lower contrast doses at higher injection rates (that is, shorter injection duration) may not yield sufficient hepatic peak enhancement during PVP. According to Heiken et al. (14), hepatic peak enhancement increases with the contrast dose at a given injection rate and patient body weight. Therefore, satisfactory aortic and hepatic enhancement may require a sufficient contrast dose and optimized injection duration. We suggest that our protocols B and C can achieve sufficient enhancement in both the aorta and liver.

We believe that the contrast dose for hepatic dynamic CT investigated in this study can be applied to single to 4-slice CT. However, scan timing during the hepatic arterial phase should be changed when single or 4-slice CT is used for the CT examination. In the scan by 64-detector CT, liver can be scanned about 2 sec, thus

center of the scan period is about 39 (38+[2/2]) sec after contrast injection start (95). In single to 4-slice CT, we should set scan delay so that the center of scan period is 39 sec after injection start. For example, when scan period is 20 sec, we should set scan delay at 29 (39-[20/2]) sec.

There are potential limitations in our study. First, as the range and mean of the body weight of our patients was lower than in patients from North America and Europe, the applicability of our results to populations of greater body weight must be confirmed. Second, there was no histopathological confirmation of HCC in about half of our patients. Nonetheless, as 43 of 47 HCC patients underwent CTHA, we think that the presence and location of HCC was confirmed in more than 90 % of our patients. While receiver operating characteristics (ROC) analysis (95) should be performed to establish the detectability of HCC under each protocol, it requires complete confirmation of HCC. Third, we adopted contrast injection protocols in which the dose was adjusted to the patient body weight and the injection duration was fixed. With these protocols, the injection rate is high in heavy patients. An upper-limit injection rate may have to be set when our contrast injection protocol is to be used in routine clinical practice. Finally, as our patient population manifested type B- or C- or

alcoholic hepatitis, the results from our study cannot be applied directly to patients free of liver damage.

In conclusion, when the injection duration is 30 sec, a total iodine dose of 525 mg or more per kg patient body weight was desirable for the good or excellent depiction of hypervascular HCC during HAP although the administration of 450 mgI per kg BW can depict hypervascular HCC.

Chapter 5. Low-Dose Hepatic Perfusion CT Using a Low Tube Voltage Technique and an Adaptive Noise Reduction Filter

Contents

ABSTRACT

Purpose: To investigate the clinical applicability of the low-dose hepatic perfusion CT using a low tube voltage technique and an adaptive noise reduction filter.

Materials and Methods: Thirty patients (mean age, 55.7 years) underwent serial hepatic dynamic CT on a 64-detector scanner (Brilliance-64, Philips). The first 15 patients were assigned to 120 kVp protocol; and the subsequent 15, 80 kVp protocol. The scan parameters for 120 kVp protocol were detector collimation 8 x 5 mm, 200 mAs, scan cycle 3 sec/cycle, scan duration 60 sec. The scan parameters for 80 kVp protocol were detector collimation 4 x 10 mm, 150 mAs, scan cycle 3 sec/cycle, scan duration 60 sec. We applied an adaptive noise reduction filter for images obtained at 80 kVp scan. In both protocols, 15g iodine was administered at same injection rate (5 mL/sec). We generated hepatic perfusion images on a workstation (EBW, Philips). The image noise on liver parenchyma was measured on 120-, 80-, and filtered 80 kVp images. Furthermore, 2 radiologists qualitatively evaluated image quality of the perfusion images for diagnostic applicability using a 3-point scale (1: poor, 3: excellent) We also calculated estimated effective dose for each protocol.

Results: The image noise on 120-, 80-, and filtered 80 kVp images was 9.4 ± 1.5, 15.0 ± 3.0, and 8.3 ± 1.9 HU, respectively. There was no statistically significant difference

between 120- and filtered 80 kVp images ($p = 0.30$), however, noise was significantly lower on 120- than 80 kVp images ($p < 0.01$). In the evaluation of diagnostic acceptability, there was no statistically significant difference between 120- and filtered 80 kVp images ($p = 0.20$) while the difference between 120- and 80 kVp images was statistically significant ($p = 0.03$). Estimated effective dose was 11.33 and 2.59 mSv for 120- and 80 kVp scan, respectively.

Conclusion: The hepatic perfusion CT with 80 kVp and an adaptive noise reduction filter had almost comparable image quality as that with 120 kVp.

INTRODCUTION

Hepatic perfusion CT demonstrates the vascular physiology of the hepatic parenchyma and hepatic lesions. It is useful for evaluating changes in the hepatic blood flow after liver transplantation (96), for the differential diagnosis of liver tumors (97), and for monitoring the tumor response to anti-angiogenic therapies and other treatments (98-100).

Detector width of multi-detector CT has increased year by year and it is possible to demonstrate blood flow information in a width of 40 mm for each organ in the current 64-detector CT. Furthermore, the recently introduced 320-detector CT instruments feature 160 mm of scan coverage and the whole liver can be scanned with serial dynamic CT. The clinical utility of hepatic perfusion CT may be enhanced by the introduction of the new multidetector scanners with wider detectors.

The most important issue for hepatic perfusion CT is high radiation exposure. As the radiation dose is proportional to the square of the tube voltage (29, 31), one of the methods for radiation reduction at CT is the use of a low tube voltage technique. Although the iodine attenuation increases as the tube voltage decreases, lowering the tube voltage decreases the amount of transmitted x-rays and results in increased image noise. The adaptive noise-reduction filter developed to reduce image noise at CT can

now be applied to low-dose CT images in the clinical setting (28, 40). The purpose of this study was to compare the quality of hepatic perfusion CT images obtained at 180 kVp with an adaptive noise reduction filter and the quality of images acquired with 120 kVp and to investigate the feasibility of using low-dose hepatic perfusion CT in the clinical setting.

MATERIALS AND METHODS

This investigation was based on a retrospective analysis of routine hepatic perfusion CT studies performed before and after we changed our standard 120 kVp protocol for the evaluation of hepatic perfusion to an 80 kVp protocol. The low-dose technique was applied to achieve a reduction in the radiation dose. Our study had institutional review board approval; due to its retrospective nature, informed patient consent was waived.

Patients

Our study included 30 patients who were referred by the department of surgery between August 2006 and December 2007. The first 15 were the last consecutive patients we scanned with 120 kVp protocol; the second 15 were the first consecutive patients we scanned after changing to a 80 kVp protocol. Hepatic perfusion CT is performed routinely in our hospital. Of the 30 patients, 5 were recipients of living-related liver transplants [LRLT], 8 were LRLT donors, 5 had cirrhosis before percutaneous transarterial splenic embolization [PSE], 2 had cirrhosis after PSE, 5 presented with liver tumors before percutaneous transhepatic portal vein embolization [PTPE], 1 had

liver tumors after PTPE, 3 had liver tumors before hepatectomy, and 1 had a common hepatic artery aneurysm. Patients with renal failure (serum creatinine level > 1.5 mg/dL [114 mol/L]) or contraindication for iodinated contrast material were excluded in advance from CT study.

Patients treated under the 120 kVp protocol ranged in age from 15–81 years (mean 55.6 years). Patients subjected to the 80 kVp protocol ranged from 23–77 years (mean 55.7 years). The difference in the age of the 2 groups was not statistically significant (Student t-test p = 0.98). The 15 patients subjected to the 120 kVp protocol were 5 men and 10 women, patients subjected to 120 kVp protocol consisted of 4 men and 11 women and there was no significant difference in the sex distribution (Fisher exact probability test p = 0.50). Body weight of patients under the 120- and 80 kVp protocol was 36–75 kg (mean, 59.7 kg) and 44–70 kg (mean, 59.3 kg), respectively. There was no statistically significant difference in the body weight between the two protocols (P = .92, two-tailed Student *t* test).

CT Scan and Contrast Injection Protocols

Multisection-level serial dynamic CT scans of the liver were obtained 0–60 sec after the start of contrast injection; the position was fixed along the z-axis, the scan cycles were 3 sec. All patients were scanned with a 64-detector CT scanner (Brilliance-64; Philips Medical Systems, Cleveland, OH).

Serial dynamic scans using 120 kVp were performed with the following parameters: rotation time 0.5 sec, detector collimation 8 x 5 mm, section thickness 5 mm, scan field of view (FOV) 50 cm, tube current 200 mAs, 120 kV. Scan parameters for 120 kVp scan were default parameters which were set in our CT scanner beforehand. Serial dynamic scans using the 80 kVp were acquired with the following parameters: rotation time 0.5 sec, detector collimation 4 x 10-mm, section thickness 10 mm, scan FOV 50 cm, tube current 150 mAs, 80 kV. A phantom study was performed to establish scan parameters for the 80 kVp protocol before clinical study with 80 kVp (Appendix).

The patients were instructed to hold their breath for 60 sec. Before scanning, each patient inhaled 3–5 L of pure oxygen per minute for about 5 min.

Iohexol (Omnipaque; Daiichi Pharmaceutical, Tokyo, Japan) with an iodine concentration of 300 mg/mL was administered using a power injector (Dual Shot;

Nemoto Kyorindo, Tokyo, Japan) and a 20-gauge intravenous catheter inserted into an antecubital vein. In all patients the contrast dose was 50 mL and the injection rate was 5.0 mL/sec. The delivery of contrast material was followed by flushing with 30 mL of physiologic saline at the same injection rate.

Adaptive Noise Reduction Filter

See the Chapter 1.

Generation of Hepatic Perfusion Images

A radiologist (Y.Y.) with 10 years of experience with abdominal CT generated hepatic perfusion images on a workstation (Extended Brilliance Workstation, version 3.5; Philips Medical Systems) using CT perfusion software that generates CT perfusion images based on maximum slope methods (101). Blood flow images supplied by the hepatic artery and portal vein, and total blood flow images of the liver were generated. Functional maps were displayed in colors ranging from blue to red, blue being the lower range of display for the blood flow.

Qualitative Analysis

To compare the quality of perfusion images acquired at 120-, 80-, and filtered 80 kVp, 2 radiologists (K.A. and T.N.) with 22 and 11 years of experience with abdominal CT, respectively, performed independent visual assessment of streak artifacts and diagnostic acceptability. After their independent evaluation, they assigned a grade by consensus.

Streak artifacts were quantified on a two-point scale where a score of 2 indicated almost no streak artifacts throughout the image and a score of 1 indicated the presence of streak artifacts. We adopted a two-point scale because it was difficult to determine the degree of streak artifact on hepatic perfusion images.

Diagnostic acceptability of the hepatic perfusion images was quantified by using a four-point scale where a score of 4 = fine granularity in the liver texture and excellent diagnostic acceptability, 3 = moderate granularity in the liver texture and good diagnostic acceptability, 2 = coarse granularity and fair diagnostic acceptability, and 1 = diagnostically unacceptable.

All images were reviewed in random order on a liquid crystal display (LCD) monitor with a spatial resolution of 1600 x 1200 pixels (Radiforce R22; Eizo, Ishikawa,

Japan) using our picture-archiving and communications system (View R, version 1.06; Yokogawa Electric, Tokyo, Japan). The window level and window width could be changed at will.

Quantitative Analysis

One board-certified radiologist (Y.Y.) with 11 years of experience with abdominal CT measured the attenuation values of the liver, abdominal aorta, and portal vein with a circular region-of-interest (ROI) cursor on source images of perfusion CT scans acquired with 120- and 80 kVp.

Hepatic attenuation was measured in 3 separate areas on images obtained at the level of the main- or right portal vein on the 1st and 15th scan. The measured area was principally the left lobe of the liver and the anterior and posterior segment of the right lobe. In patients who had undergone resection of the left liver lobe we measured hepatic attenuation in the anterior-, middle-, and posterior third part of the right lobe. The attenuation values for each scan were averaged. An attempt was made to maintain a constant ROI area of approximately 2 cm^2; the range of ROI areas was 0.8–2.0 cm^2. Visible blood vessels, bile ducts, and artifacts were carefully excluded from ROI

measurements in the hepatic parenchyma. Contrast enhancement in the liver parenchyma was calculated as the absolute difference from the attenuation value of the liver (in Hounsfield units, HU) on the 1st and 15th scan.

Aortic attenuation values were measured at the level of the main- or right portal vein on the 1st and 5th scan. An attempt was made to maintain a constant ROI area of approximately 80 mm^2; the range of the ROI areas was 0.3–1.0 cm^2. Contrast enhancement in the aorta was calculated as the absolute difference from the attenuation value of the aorta (in HU) on the 1st and 5th scan.

Attenuation values of the portal vein were measured in the main- or right portal vein on the 1st and 8th scan. An attempt was made to maintain a constant ROI area of approximately 50 mm^2; the range of the ROI areas was 0.3–0.7 cm^2. Contrast enhancement in the portal vein was calculated as the absolute difference from the attenuation value of the portal vein (in HU) on the 1st and 8th scan.

In general, image noise was defined as the standard deviation of the mean CT number (29). We measured the image noise on 120 kVp-, 80 kVp-, and filtered 80 kVp images. It was determined in 3 separate areas of the liver on images obtained at the level of the main- or right portal vein during the 1st scan and the values were

averaged.

Estimation of the Effective Radiation Dose

We recorded the volume CT dose index ($CTDI_{volume}$) for serial dynamic scans at 120- and 80 kVp; calculation was on the operating console of the CT scanner. Furthermore, we calculated the dose-length product (DLP) by using the equation (44):

DLP = $CTDI_{volume}$ x scan range along z-axis [4.0 cm] (mGy cm)

Then we estimated the effective radiation dose by using the equation (102):

Effective dose = (DLP) x 0.012 (mSv)

Statistical Analysis

All enhancement values are reported as the mean ± standard deviation (SD). We performed pairwise comparison of the visual scores assigned to 120-, 80-, and filtered 80 kVp images by using the Steel test; values obtained at 120 kVp were the control. We used the $\chi 2$ test to compare the frequency of streak artifact in each scan technique.

Interobserver variability in the visual analysis of tumor conspicuity was assessed with the Cohen coefficients of concordance to measure the degree of agreement between the 2 radiologists.

To compare the enhancement values of the liver, aorta, and portal vein on images acquired at 120- and 80 kVp we used the paired t-test. To perform multiple comparisons of image noise on 120-, 80-, and filtered 80 kVp images we applied the Dunnett method; values obtained at 120 kVp were the control.

Statistical analyses were performed with the free statistical software "R" (R, version 2.6.1; The R Project for Statistical Computing; http://www.r-project.org/). For all statistical analyses, a p value less than 0.05 was considered to indicate a significant difference.

RESULTS

Qualitative Analysis

There was no statistically significant difference in the frequency of streak artifacts among 120 kVp-, 80 kVp-, and filtered 80 kVp images ($p = 0.29$) (Table 5.).

In the visual evaluation of diagnostic acceptability of the hepatic perfusion images, there was no statistically significant difference between 120 kVp- and filtered 80 kVp images ($p = 0.20$). On the other hand, the difference between 120 kVp- and 80 kVp images was statistically significant ($p = 0.03$) (Fig. 5.1.).

The κ coefficient for streak artifacts and diagnostic acceptability was 0.81 and 0.71, respectively, indicating good interobserver agreement in the visual evaluation.

Quantitative Analysis

The enhancement values of the liver, aorta, and portal vein on 120 kVp images were 91.7 ± 11.9, 293.9 ± 91.1, and 79.5 ± 28.5 HU, respectively; on 80 kVp images they were 127.5 ± 21.7, 490.5 ± 67.7, and 128.6 ± 28.2 HU. At all organs, the

enhancement values were significantly higher on 80- than 120 kVp images ($p < 0.01$) (Fig. 5.2.).

The image noise value on 120-, 80-, and filtered 80 kVp images was 9.4 ± 1.5, 15.0 ± 3.0, and 8.3 ± 1.9 HU, respectively. There was no statistically significant difference between 120- and filtered 80 kVp images ($p = 0.30$), however, image noise was significantly lower on 120- than 80 kVp images ($p < 0.01$) (Fig. 5.3.).

Effective Dose

CTDIvolume for 120- and 80 kVp protocols were 236 and 54 mGy, respectively; the corresponding DLP was 944 and 216 mGy cm, respectively. Furthermore, the corresponding estimated effective dose was 11.33 and 2.59 mSv, respectively.

Representative cases are shown in Figures 5.4. -5.6..

DISCUSSION

In general, one of the most critical issues for perfusion CT is its high radiation exposure. In our institute, the DLP of routine three-phase hepatic dynamic CT including pre-contrast enhanced scan, hepatic arterial phase scanning, and portal venous phase scanning ranges 522–1044 mGy cm when we use automatic dose modulation technique (38), tube voltage is 120 kVp, planned tube current is 300 mA, scan time is 0.5 sec, and scan range is 20 cm. DLP of our 120 kVp protocol for hepatic perfusion CT was 944 mGy cm and it was almost comparable maximum DLP for hepatic dynamic CT and relatively high. On the other hand, DLP of 80 kVp protocol was 216 mGy cm. The reference DLP value for the abdomen is 770 mGy cm (102); thus, at 216 mGy cm, we concluded that the dose for scanning with 80 kVp technique was within an acceptable range.

Strategies for reducing the radiation dose at MDCT include lowering the tube current or tube voltage (28-31), performing fewer scans (33, 35), using X-ray filtration (36), controlling x-ray tube focal spot motion and beam collimation (42), applying adaptive noise reduction filters (28), and using a dose modulation technique (42). Among these methods, low tube voltage techniques drastically reduce the radiation dose (29-31). However, the low tube voltage (90 or 80 kVp) technique affects low contrast

detectability, tissue contrast, iodine enhancement, and image noise, therefore, the application of this technique in the clinical setting requires an understanding of the characteristics of low tube voltage images (28-30).

There was a direct correlation between the contrast noise ratio (CNR) and the radiation dose at a given tube voltage. Funama et al. reported that at identical radiation doses, the CNR at 90 kV was 1.29 times higher than at 120 kV (29). They also described that a 35% reduction in the radiation dose can be achieved when scanning is performed at 90- rather than 120 kV without degradation of detectability on low-contrast images (29). To control dose reduction within 35% at low tube voltage setting, we have to increase tube current second compensatorily. Although currently available multidetector CT scanners can accommodate the higher tube current needed with low tube voltage settings, the tube power is not high enough for these scan parameter settings. Therefore, use of the noise reduction filter may be indispensable at low tube voltage settings.

Noise reduction filter can reduce image noise and it is effective to improve the quality of abdominal CT images obtained at a reduced tube current. However, application of the noise reduction filter may also render the boundaries of each structure indistinct (39). On the other hand, Funama et al. reported that a novel adaptive filter

could reduced image noise without rendering the boundaries of structures indistinct the by changing kernel size, smoothing, and edge enhancement according to the standard deviation of the CT number in the local region (28); and they also reported that tube current can be reduced by 50% without loss of nodule detectability by applying the adaptive noise reduction filter. Our adaptive noise reduction filter (XRES filter) can also reduce image noise without obscuring the boundaries of each structure. To our knowledge, our study is the first report to apply an adaptive noise reduction filter to images obtained with low tube voltage scan technique.

Iodine enhancement is also affected by the low tube voltage technique. The attenuation of iodine increases as the effective energy (keV) decreases because the energies in the x-ray beam move closer to the k-absorption edge of iodine. There was a significant linear correlation between the CT number and iodine concentration at a given tube voltage. The increase was greater at lower tube voltage setting. For example, CT number at 90 kV was about 1.4 times higher than at 120 kV at identical iodine concentration (30). Therefore, at the lower kVp setting, the difference of iodine contrast of each organ become more prominent than at 120 kVp setting and it may have an advantage in generation of hepatic perfusion images in which time-density curves for each pixel are calculated.

In our low-tube voltage technique with the adaptive noise reduction filter could achieve almost same image noise and diagnostic acceptability although radiation dose of low-dose technique was almost 1/4 of that for 120 kVp technique. Thus, we believe that calculated values of blood flow in hepatic perfusion images are almost equivalent between 120- and 80 kVp scan technique, however, statistical comparison have not been performed because it was difficult to perform both 120- and 80 kVp hepatic perfusion scan from an ethical problem.

The arithmetic algorithm for hepatic perfusion images includes essential fallacy. In general, arithmetic algorithm for perfusion images is designed on the assumption that administered contrast material remain within the capillary vein in the tissue and does not leak to the interstitium of the tissue. However, in the liver, administered contrast material rapidly leaks to the interstitium after arrival at the capillary veins. Therefore, blood flow values in the hepatic perfusion images may not accurately reflect blood flow in the liver. Furthermore, we used the arithmetic algorithm based on maximum slope method (101) for this study. Maximum slope method premises that there is no outflow of the contrast to the vein. To work out this premise, we have to intravenously administer contrast media with injection rate of more than 10 mL/sec, however, this flow rate is not practical in the clinical setting. From these discussions, we have to

improve arithmetic algorithm for hepatic perfusion images to measure accurate hepatic blood flow.

Our study has some limitations. First, we did not verify whether calculated blood flow values are almost equivalent on images obtained at 120- and 80 kVp scans. To investigate this, we have to scan the same patients with 120- and 80 kVp scans, however, it has an ethical problem. We are now planning to perform to animal experiments to investigate reproducibility of measured blood flow value at different tube voltage setting. Second, as the range and mean of the body weight of Japanese patients is lower than in patients from North America and Europe. Heavier population than Japanese patients may require more radiation dose than our results. The applicability of our results to populations of greater body weight must be confirmed.

In conclusion, hepatic perfusion CT with 80 kVp technique and an adaptive noise reduction filter could achieve radiation dose reduction of 77 % as compared with that with 120 kVp technique and it showed diagnostic image quality comparable to that of the 120 kVp tube voltage technique.

Figure Legends and Figures

Fig.1.1. Transverse CT image at level of left portal vein in 68-year-old man with hepatocellular carcinoma (HCC). Hepatic arterial phase image (b) demonstrates liver tumor which is a hyperattenuatted compared with the surrounding liver parenchyma. This tumor is depicted as a hypoattenuated tumor during pre-enhanced image (a), portal venous phase image (c), and equilibrium phase image (d).

Fig.1.2. Transverse CT image at level of pancreas tail in 72-year-old woman with pancreatic cancer. In the pre-enhanced image (a), pancreatic tumor cannot be demonstrated. The pancreatic parenchymal phase image (b) depicts hypoattenuated tumor in the pancreas tail. This image also clearly demonstrate peripancreatic vessels, In pre-enhanced image (a), pancreatic tumor cannot be demonstrated. Hepatic metastasis is not seen in the portal venous phase image (c).

Fig. 1.3A. Principle underlying the XRES noise-reduction algorithm. The image is separated into 3 components; these are filtered independently by specialized kernels. The results image is obtained by summing the filtered components. Examples of

decomposition are (A) weakly textured organs, (B) elongated structures such as vessels, and (C) boundaries between organs.

Fig. 1.3B. XRES multi-resolution layer based on the Laplacian pyramid (24). A succession of sub-bands, each representing different scales, is created using a low-pass filter and down-sampling. The sub-bands are processed according to the method described in Fig. 1A. A filtered image is obtained with the filtered sub-bands using up-sampling and accumulation operations.

Figure 2.1. Multislice CT phantom (type MHT, Kyoto-Kagaku, Kyoto, Japan). A syringe containing different concentrations of iodine solution (0-, 2-, 4-, 6-, 8-, 10-, 12-, and 14 mg/mL) was inserted in the central cavity of the phantom.

Figure 2.2. The low-contrast module phantom (Catphan 424; Phantom Laboratory, Cambridge, NY). Background was used to measure the image noise at each of the applied scan techniques.

Figure 2.3. Graph showing the relationship between the iodine concentration and the attenuation value (CT number) in the test syringe at each kV setting. At each kV setting there was a strong positive linear correlation between the iodine concentration and the attenuation value.

Figure 2.4. Graph showing the relationship between the iodine concentration and the image noise in the the test syringe at each kV setting. At all kV settings the image noise was almost constant irrespective of the iodine concentration.

Figure 2.5. Graph showing the relationship between the radiation dose ($CTDI_{volume}$) and tube current second (mAs) at each kV setting. At each kV setting there was a strong positive linear correlation between the tube current second and $CTDI_{volume}$ ($r = 0.99, p < 0.001$).

Figure 2.6. Graph showing the relationship between the image noise and the tube current second (mAs) at each kV scan. The image noise value on the processed images acquired with the XRES filter at 80 kV and 150 mAs was comparable to images obtained at 120 kV and 200 mAs.

Figure 3.1. Examples of visual grade of the pancreatic enhancement.

(1a) Transaxial CT image at level of the pancreaitc body and tail of a 62-year-old woman with pancreatic cancer. (1b) Trans-axial CT image at level of the pancreatic body and tail of a 41-year-old man who was proven to be without pancreatic lesions. (1c) Trans-axial CT image at level of the pancreas body and tail of a 72-year-old man with pancreas head cancer that causes dilatation of the main pancreatic duct.

Fig. 1a, 1b, and 1c, show grade 2 (despite slight pancreatic enhancement, the image is diagnostically inadequate), grade 3 (adequate), and grade 4 (excellent) of the pancreatic enhancement, respectively.

Figure 3.2. Enhancement of the pancreas during the pancreatic parenchymal phase. Under protocol 1, mean pancreatic enhancement in patients with a body weight equal to or more than 60 kg (group B) was significantly lower than in patients weighing less than 60 kg (group A) ($p = 0.02$). Under protocol 2, there was no statistically significant difference between the 2 weight groups ($p = 0.45$).

Figure 3.3. Enhancement of the celiac artery during the arterial phase and the pancreatic parenchymal phase (PPP)

A. Mean enhancement of the celiac artery during the arterial phase. Under protocol 1, enhancement was significantly lower in patients with a body weight equal to or more than 60 kg (group B) than in those weighing less than 60 kg (group A) ($p < 0.01$). Under protocol 2, there was no statistically significant difference between the 2 weight groups ($p = 0.21$).

B. Mean enhancement of the celiac artery during PPP. Irrespective of the protocol used, there was no statistically significant difference between the 2 weight groups (protocol 1: $p = 0.64$, protocol 2: $p = 0.59$).

Figure 3.4. Hepatic enhancement during the portal venous phase.

Under protocol 1, mean hepatic enhancement was significantly higher in patients weighing less than 60 kg (group A) than in those weighing 60 kg or more (group B) ($p < 0.01$). Under protocol 2, there was no statistically significant difference between the 2 weight groups ($p = 0.34$).

Figure 3.5. Enhancement of the portal vein during the pancreatic parenchymal phase.

Under protocol 1, mean enhancement of the portal vein was significantly higher in patients weighing less than 60 kg (group A) than in those weighing 60 kg or more

(group B) ($p < 0.01$). Under protocol 2, there was no statistically significant difference between the 2 weight groups ($p = 0.24$).

Figure 4.1. Aortic enhancement during the hepatic arterial phase obtained with the 3 different contrast injection protocols. Aortic enhancement values in protocols A, B, and C were 224.5 ± 50.3, 264.4 ± 47.3, and 291.0 ± 42.7 HU, respectively. There was a statistically significant difference between protocols A and B ($p < 0.01$), A and C ($p < 0.01$), and B and C ($p = 0.02$).

Figure 4.2. Tumor-liver-contrast (TLC) in each contrast injection protocol during hepatic arterial phase. The TLC in protocols A, B, and C was 26.5 ± 8.3, 38.4 ± 8.6, and 52.3 ± 20.3 HU, respectively; the difference was significant between protocols A and B ($p = 0.05$), A and C ($p < 0.01$), and B and C ($p = 0.02$).

Figure 4.3. Hepatic enhancement in each contrast injection protocol during portal venous phase. The mean values for hepatic enhancement were 43.2 HU ± 8.7, 48.7

HU ± 9.1, 53.9 HU ± 10.2, respectively, for protocols A, B, and C. There were statistically significant differences between protocols A and B, A and C, and B and C ($p = 0.02$, $p < 0.01$, and $p = 0.02$, respectively).

Figure 4.4. Visual evaluation of tumor conspicuity during the hepatic arterial phase for each of the 3 different contrast injection protocols. There was a significant difference between protocols A and B ($p = 0.02$) and A and C ($p < 0.01$) but not between protocols B and C ($p = 0.22$).

Figure 4.5.

(a) Transverse CT image at the level of the left portal vein in a 68-year-old man with HCC, scanned according to protocol A. The TLC in this patient was 27.0 HU (mean TLC for protocol A, 26.5 HU).

(b) Transverse CT image at the level of the porta hepatis in an 82-year-old man with HCC, scanned according to protocol B. The TLC in this patient was 44.0 HU (mean TLC for protocol B, 38.4 HU).

(c) Transverse CT image at the level of the left portal vein in a 73-year-old man with HCC, scanned according to protocol C. The TLC in this patient was 51.1 HU (mean TLC for protocol C, 52.3 HU).

Figure 5.1. Diagnostic acceptability of the hepatic perfusion images with each scan technique.

In the visual evaluation of diagnostic acceptability of the hepatic perfusion images, there was no statistically significant difference between 120 kVp- and filtered 80 kVp images, while the difference between 120 kVp- and 80 kVp images was statistically significant.

Note: "f-80 kVp" means filtered 80 kVp images.

Figure 5.2. Enhancement values in the liver, aorta, and portal vein.

At all organs, the enhancement values were significantly higher on 80- than 120 kVp images ($p < 0.01$).

Figure 5.3. Image noise in the hepatic parenchyma in each technique.

There was no statistically significant difference between 120- and filtered 80 kVp images ($p = 0.30$), however, image noise was significantly lower on 120- than

80 kVp images ($p < 0.01$).

Note: "f-80 kVp" means filtered 80 kVp images.

Figure 5.4. A 15-year-old girl who underwent living-related liver transplants (LRLT) due to Wilson disease.

The portal perfusion image acquired with 120 kVp showed fine granularity in the liver texture. There were minimal streak artifacts.

Figure 5.5. A 69-year-old man with hepatocellular carcinoma before percutaneous transhepatic portal vein embolization (PTPE). The comparison of portal perfusion images obtained with 80- (A) and filtered 80 kVp (B) demonstrated that the granularity in the liver texture was improved on filtered 80- compared to non-filtered 80 kVp images.

Figure 5.6. A 59-year-old female recipient of living-related liver transplants (LRLT) due to alcoholic cirrhosis. The source image of the hepatic perfusion CT scan acquired at 120 kVp (Fig. 5.6A, white arrow) and the corresponding hepatic arterial perfusion image (Fig. 5.6B, pink arrow) contained streak artifacts.

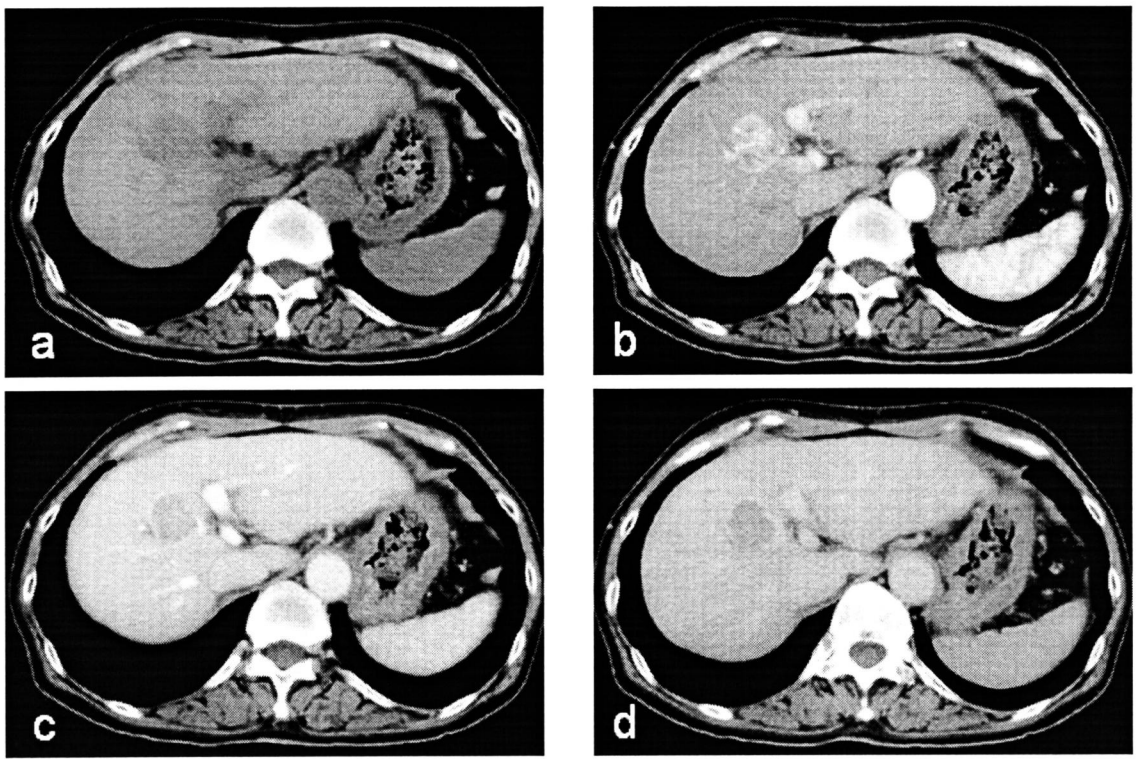

Fig.1.1. Transverse CT image at level of left portal vein in 68-year-old man with hepatocellular carcinoma (HCC). Hepatic arterial phase image (b) demonstrates liver tumor which is a hyperattenuatted compared with the surrounding liver parenchyma. This tumor is depicted as a hypoattenuated tumor during pre-enhanced image (a), portal venous phase image (c), and equilibrium phase image (d).

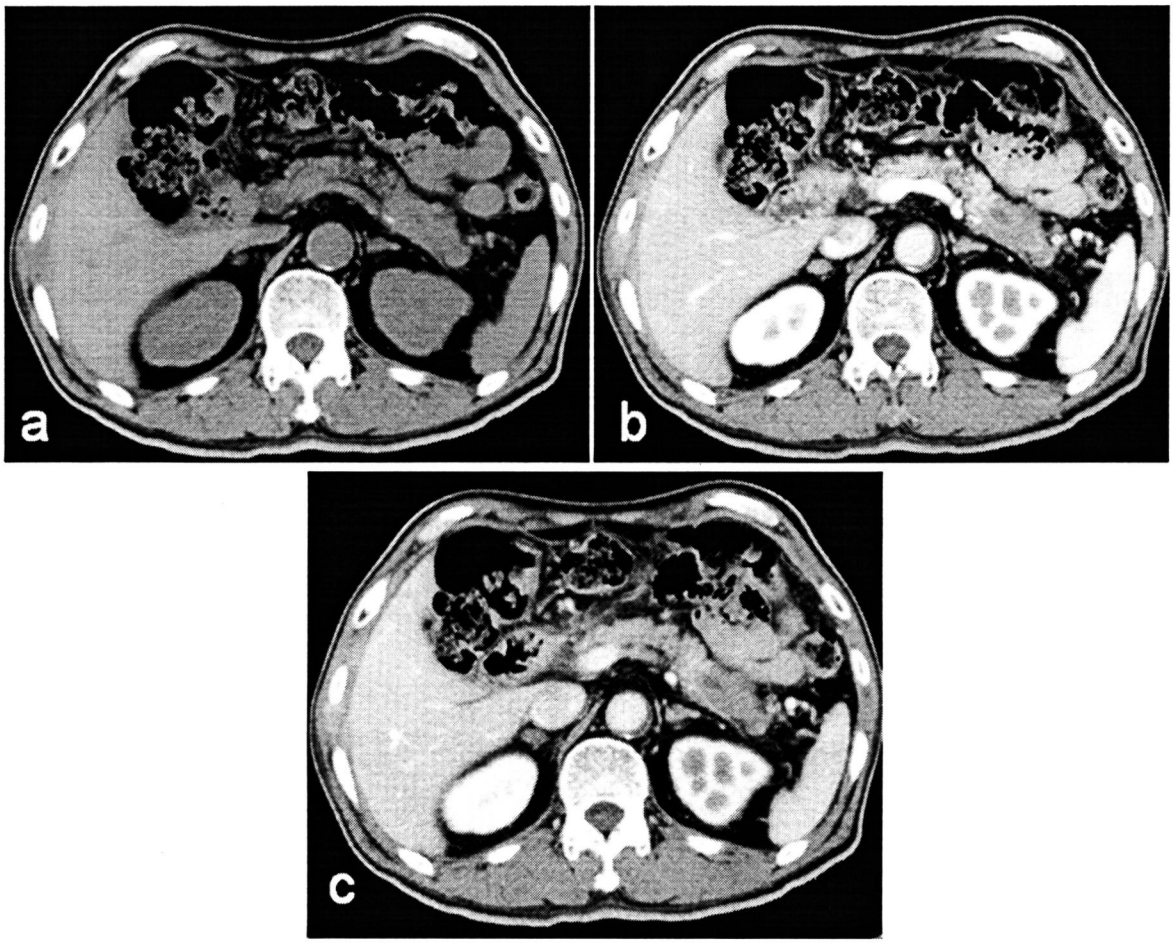

Fig.1.2. Transverse CT image at level of pancreas tail in 72-year-old woman with pancreatic cancer. In the pre-enhanced image (a), pancreatic tumor cannot be demonstrated. The pancreatic parenchymal phase image (b) depicts hypoattenuated tumor in the pancreas tail. This image also clearly demonstrate peripancreatic vessels, In pre-enhanced image (a), pancreatic tumor cannot be demonstrated. Hepatic metastasis is not seen in the portal venous phase image (c).

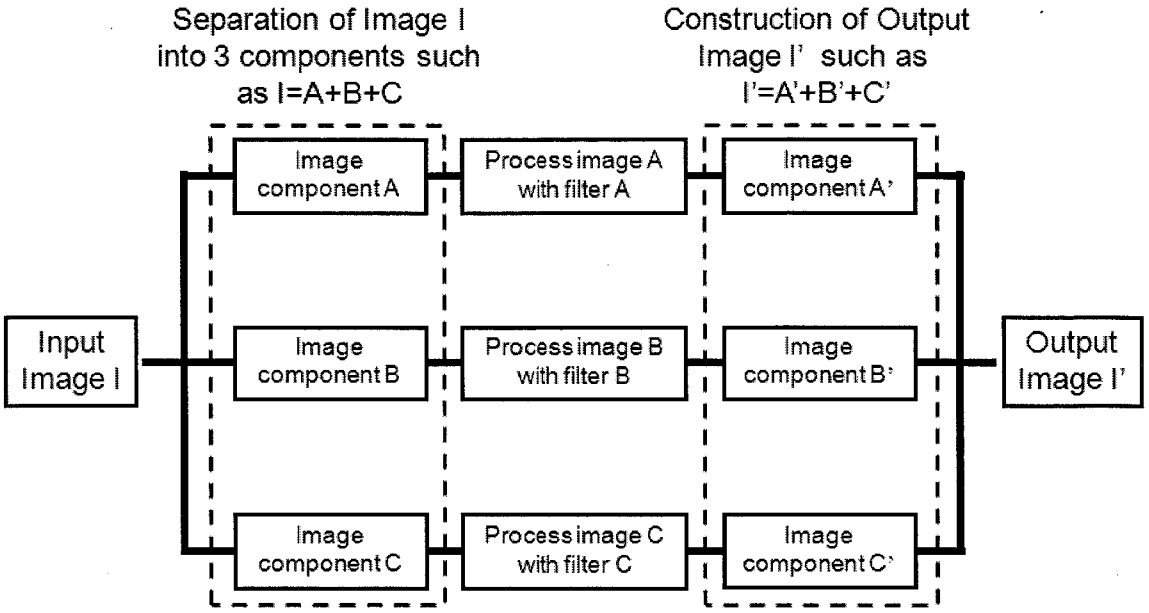

Fig. 1.3A. Principle underlying the XRES noise-reduction algorithm.

The image is separated into 3 components; these are filtered independently by specialized kernels. The results image is obtained by summing the filtered components. Examples of decomposition are (A) weakly textured organs, (B) elongated structures such as vessels, and (C) boundaries between organs.

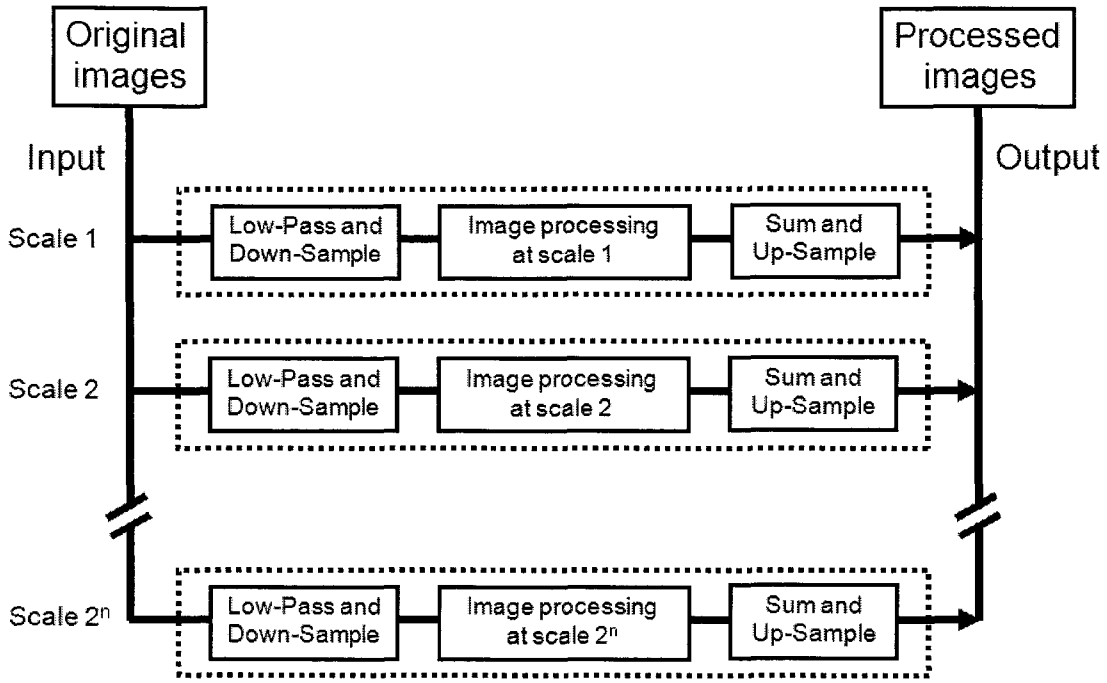

Fig. 1.3B. XRES multi-resolution layer based on the Laplacian pyramid (24).

A succession of sub-bands, each representing different scales, is created using a low-pass filter and down-sampling. The sub-bands are processed according to the method described in Fig. 1A. A filtered image is obtained with the filtered sub-bands using up-sampling and accumulation operations.

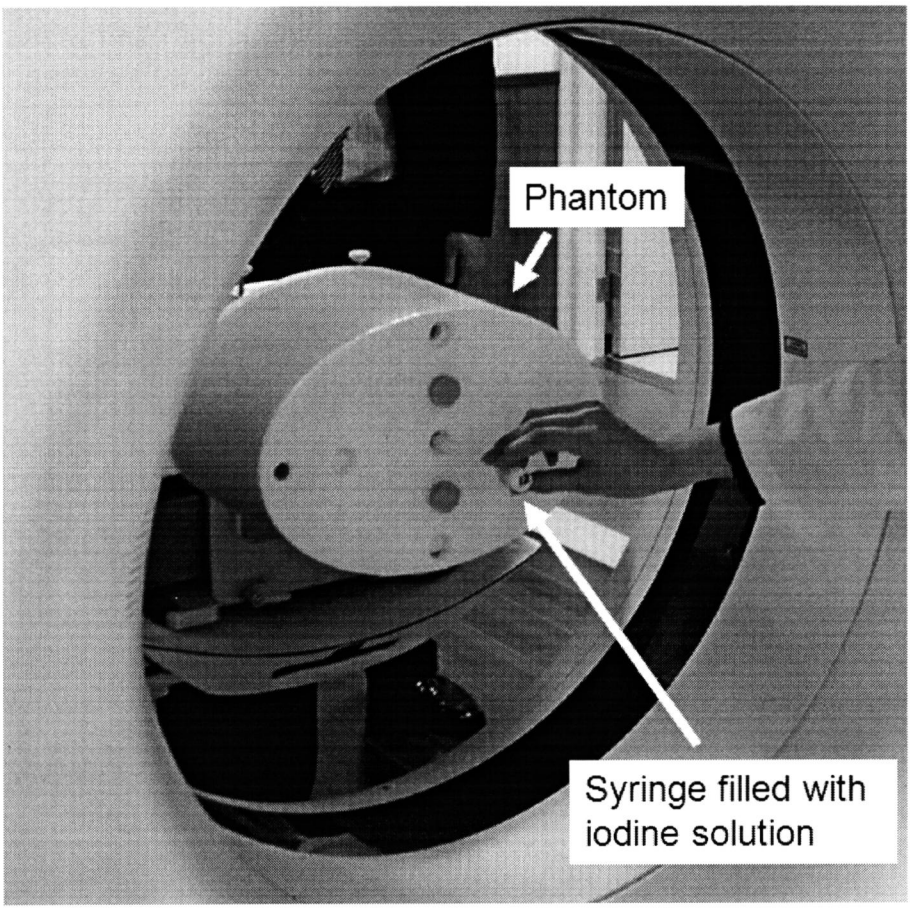

Figure 2.1. Multislice CT phantom (type MHT, Kyoto-Kagaku, Kyoto, Japan).

A syringe containing different concentrations of iodine solution (0-, 2-, 4-, 6-, 8-, 10-, 12-, and 14 mg/mL) was inserted in the central cavity of the phantom.

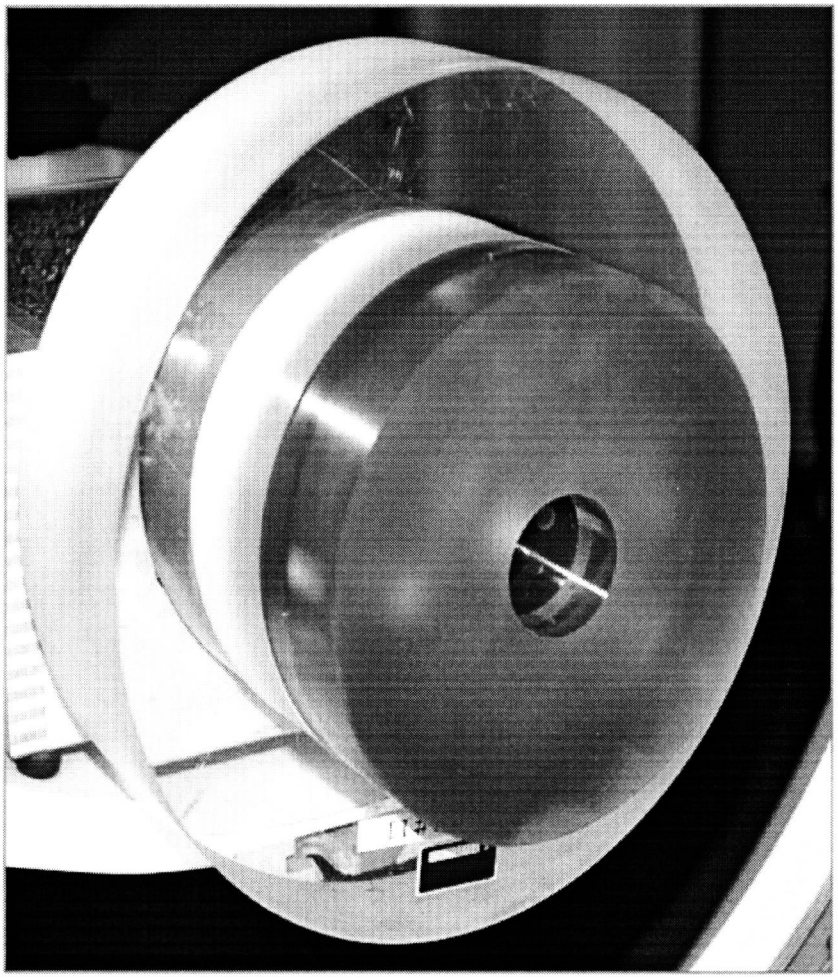

Figure 2.2. The low-contrast module phantom (Catphan 424; Phantom Laboratory, Cambridge, NY). Background was used to measure the image noise at each of the applied scan techniques.

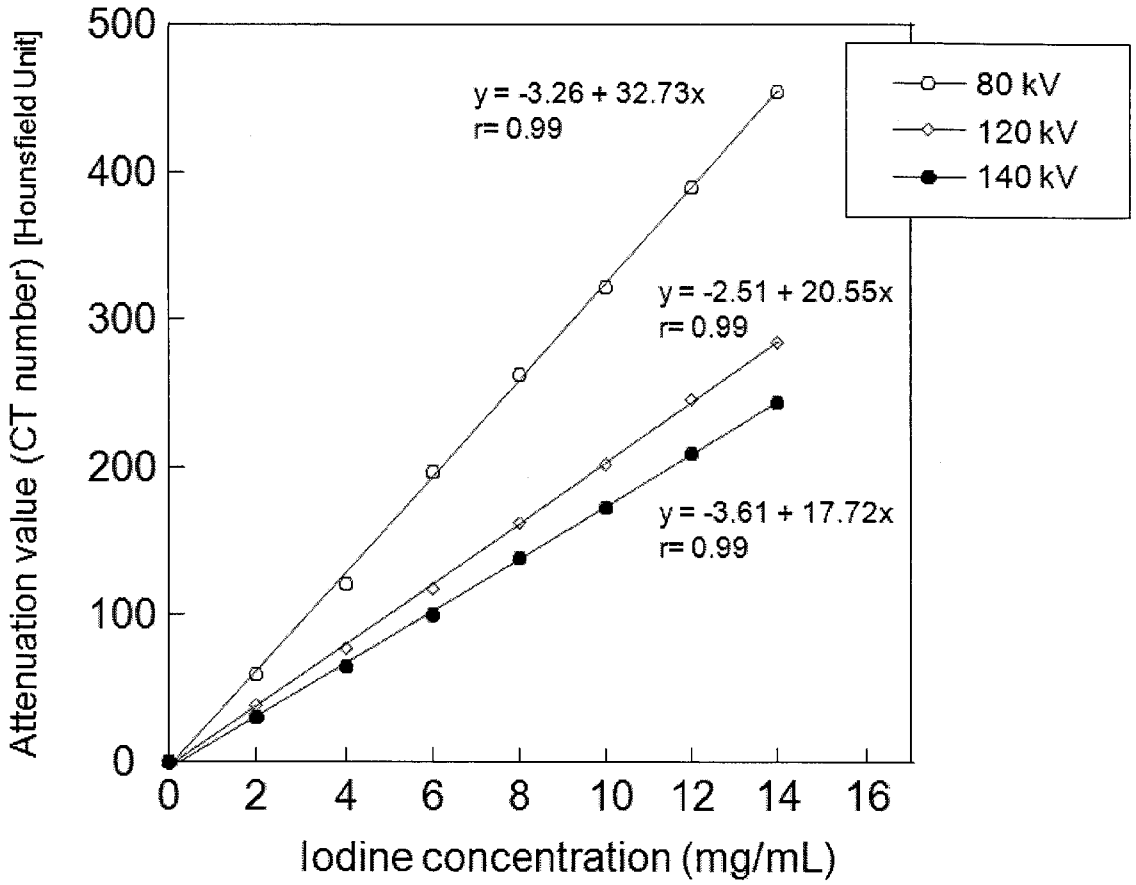

Figure 2.3. Graph showing the relationship between the iodine concentration and the attenuation value (CT number) in the test syringe at each kV setting.

At each kV setting there was a strong positive linear correlation between the iodine concentration and the attenuation value.

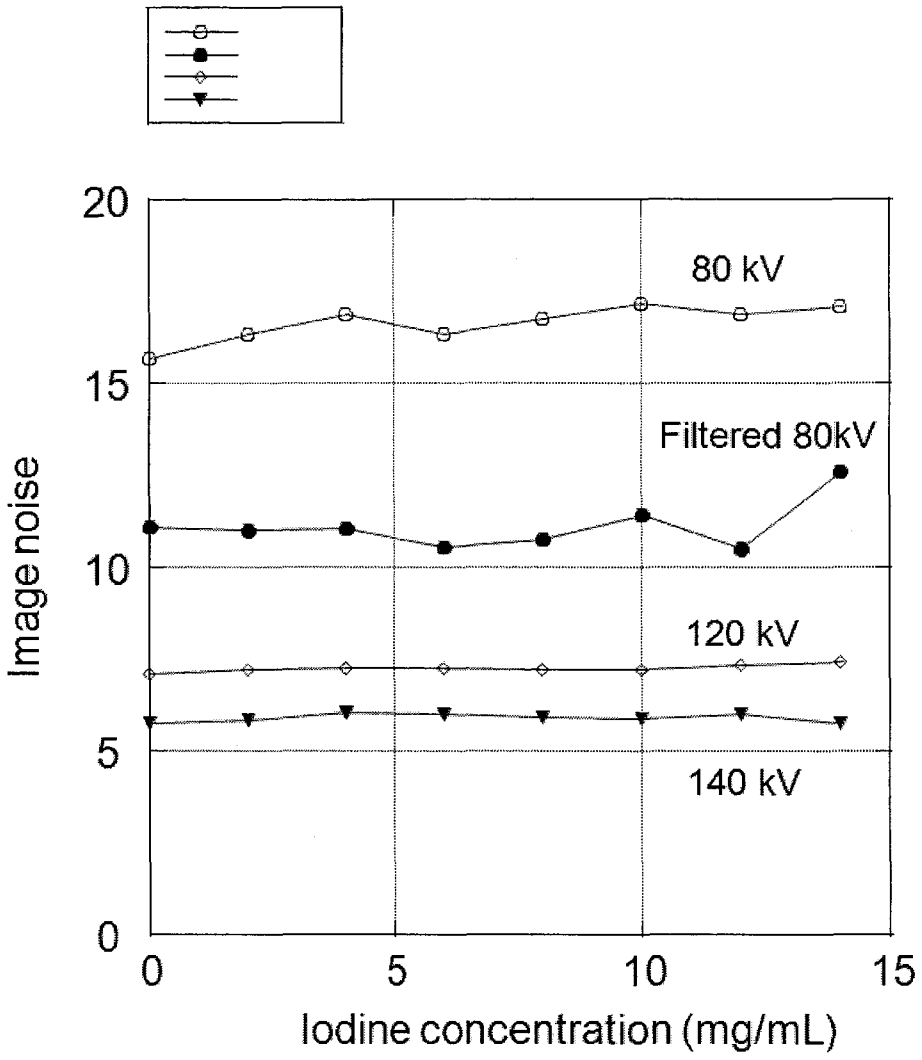

Figure 2.4. Graph showing the relationship between the iodine concentration and the image noise in the test syringe at each kV setting.

At all kV settings the image noise was almost constant irrespective of the iodine concentration.

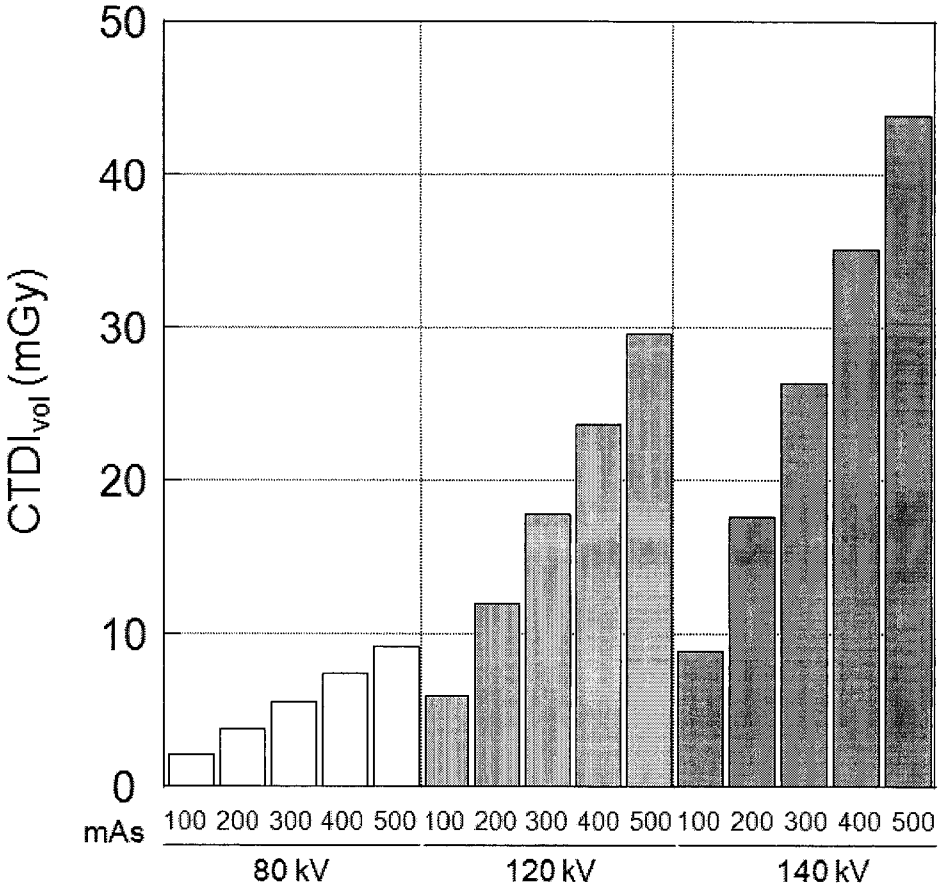

Figure 2.5. Graph showing the relationship between the radiation dose ($CTDI_{volume}$) and the tube current second (mAs) at each kV setting.

At each kV setting, there was a strong positive linear correlation between the tube current second and $CTDI_{volume}$ ($r = 0.99, p < 0.001$).

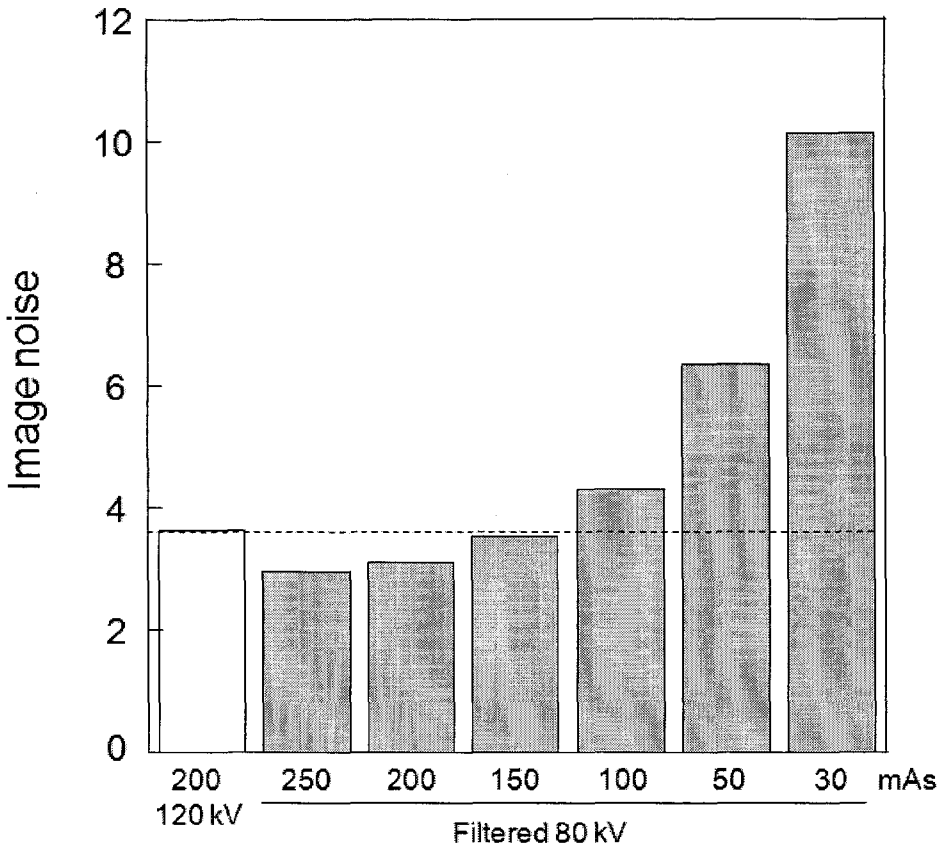

Figure 2.6. Graph showing the relationship between the image noise and tube current second (mAs) at each kV scan.

The image noise value on the processed images acquired with the XRES filter at 80 kV and 150 mAs was comparable to images obtained at 120 kV and 200 mAs.

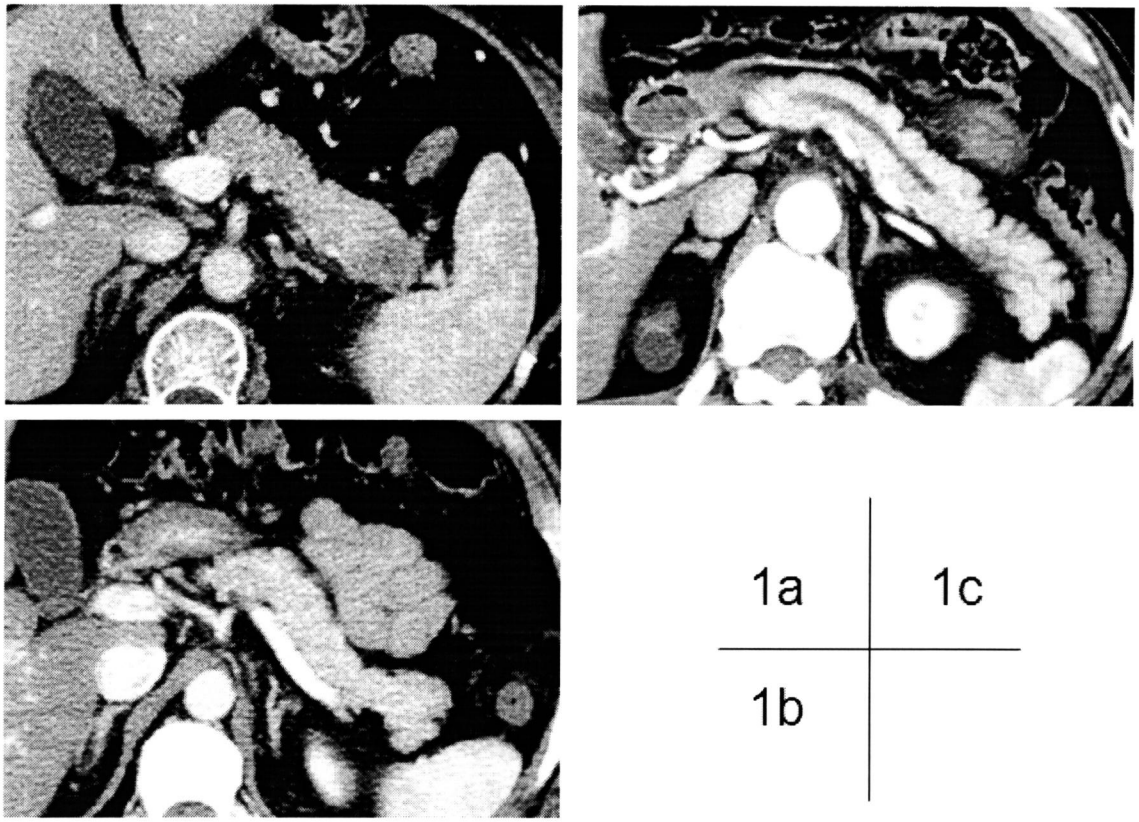

Figure 3.1. Examples of visual grade of the pancreatic enhancement.

(1a) Transaxial CT image at level of the pancreaitc body and tail of a 62-year-old woman with pancreatic cancer. (1b) Trans-axial CT image at level of the pancreatic body and tail of a 41-year-old man who was proven to be without pancreatic lesions. (1c) Trans-axial CT image at level of the pancreas body and tail of a 72-year-old man with pancreas head cancer that causes dilatation of the main pancreatic duct.

Figs. 1a, 1b, and 1c, show grade 2 (despite slight pancreatic enhancement, the image is diagnostically inadequate), grade 3 (adequate), and grade 4 (excellent) of the pancreatic enhancement, respectively.

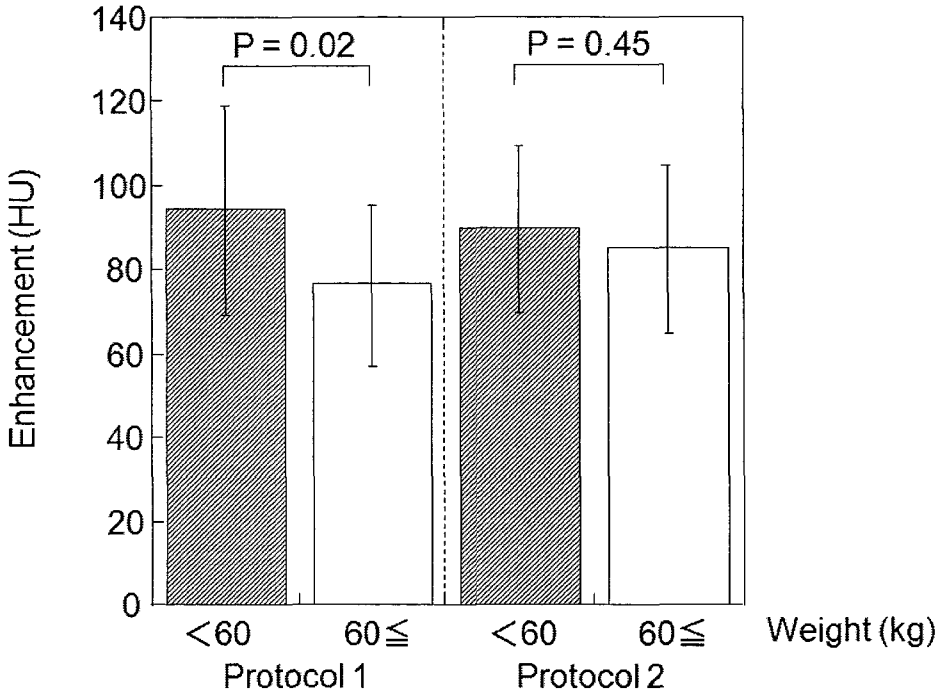

Figure 3.2. Enhancement of the pancreas during the pancreatic parenchymal phase. Under protocol 1, mean pancreatic enhancement in patients with a body weight equal to or more than 60 kg (group B) was significantly lower than in patients weighing less than 60 kg (group A) ($p = 0.02$). Under protocol 2, there was no statistically significant difference between the 2 weight groups ($p = 0.45$).

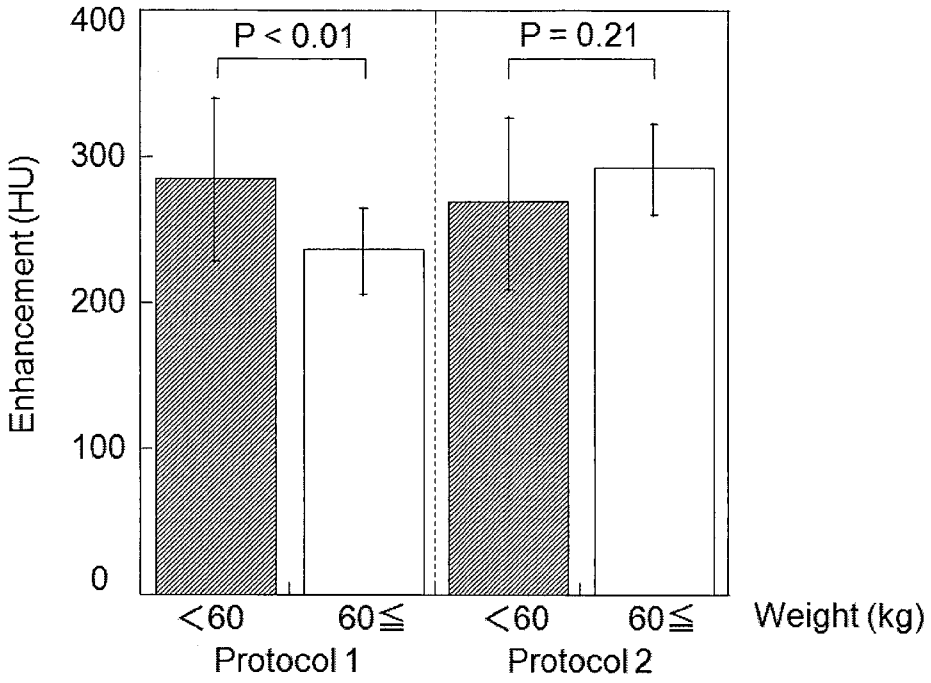

Figure 3.3. Enhancement of the celiac artery during the arterial phase and the pancreatic parenchymal phase (PPP)

A. Mean enhancement of the celiac artery during the arterial phase. Under protocol 1, enhancement was significantly lower in patients with a body weight equal to or more than 60 kg (group B) than in those weighing less than 60 kg (group A) ($p < 0.01$). Under protocol 2, there was no statistically significant difference between the 2 weight groups ($p = 0.21$).

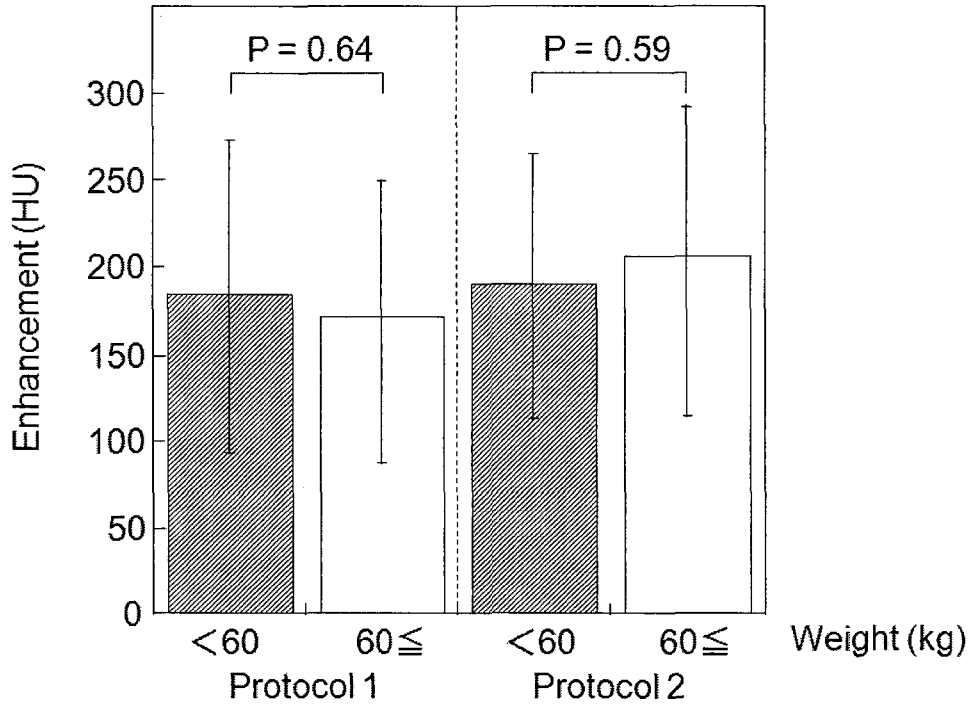

B. Mean enhancement of the celiac artery during PPP. Irrespective of the protocol used, there was no statistically significant difference between the 2 weight groups (protocol 1: p = 0.64, protocol 2: p = 0.59).

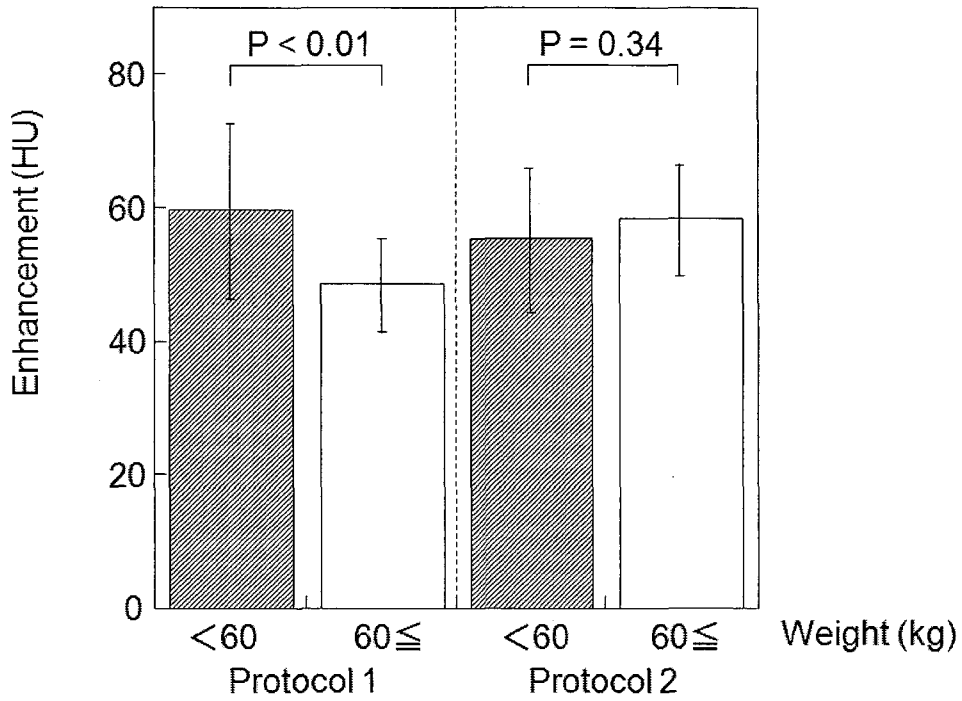

Figure 3.4. Hepatic enhancement during the portal venous phase.

Under protocol 1, mean hepatic enhancement was significantly higher in patients weighing less than 60 kg (group A) than in those weighing 60 kg or more (group B) ($p < 0.01$). Under protocol 2, there was no statistically significant difference between the 2 weight groups ($p = 0.34$).

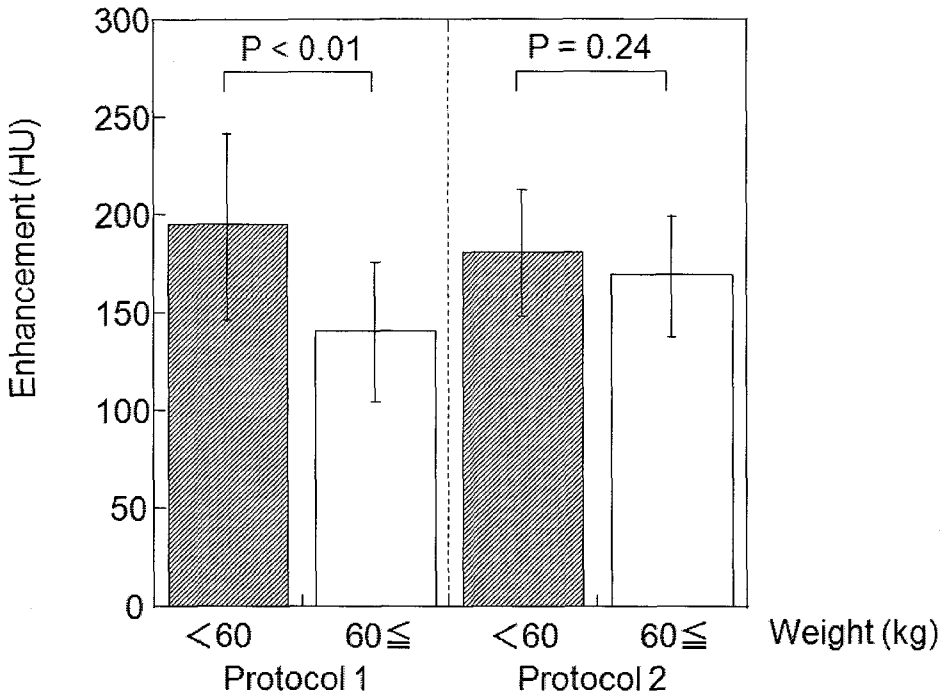

Figure 3.5. Enhancement of the portal vein during the pancreatic parenchymal phase. Under protocol 1, mean enhancement of the portal vein was significantly higher in patients weighing less than 60 kg (group A) than in those weighing 60 kg or more (group B) ($p < 0.01$). Under protocol 2, there was no statistically significant difference between the 2 weight groups ($p = 0.24$).

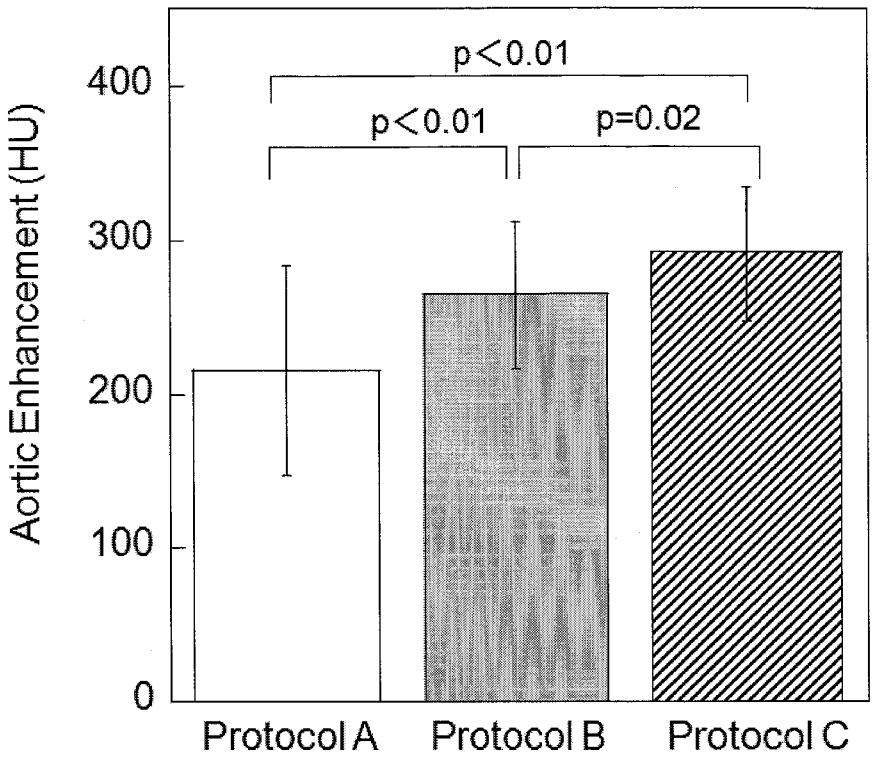

Figure 4.1. Aortic enhancement during the hepatic arterial phase obtained with the 3 different contrast injection protocols. Aortic enhancement values in protocols A, B, and C were 224.5 ± 50.3, 264.4 ± 47.3, and 291.0 ± 42.7 HU, respectively. There was a statistically significant difference between protocols A and B ($p < 0.01$), A and C ($p < 0.01$), and B and C ($p = 0.02$).

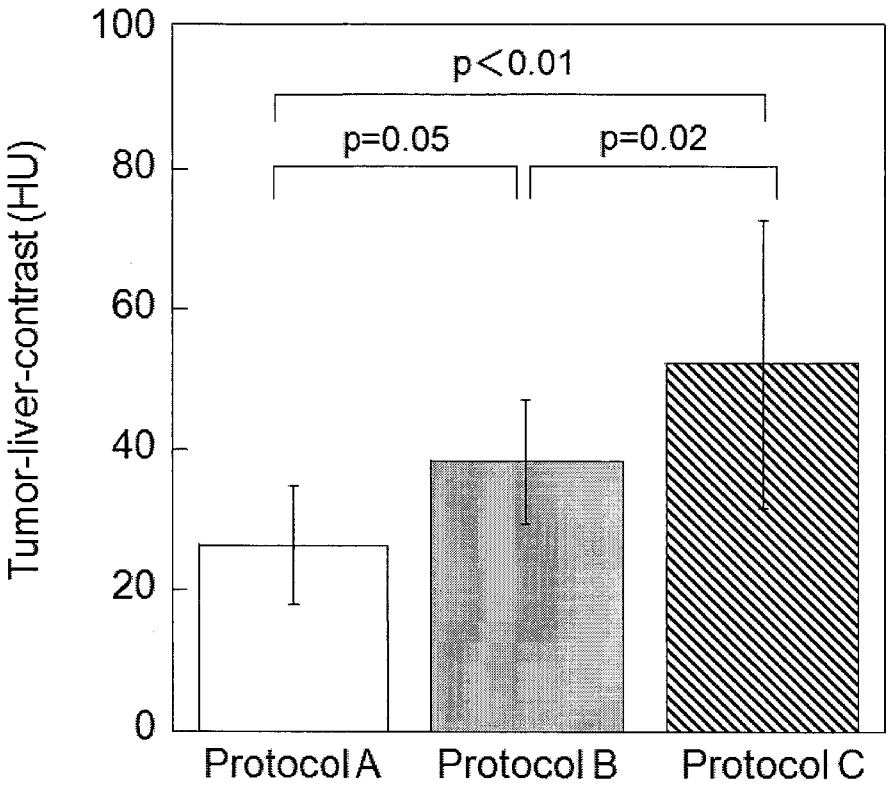

Figure 4.2. Tumor-liver-contrast (TLC) in each contrast injection protocol during hepatic arterial phase. The TLC in protocols A, B, and C was 26.5 ± 8.3, 38.4 ± 8.6, and 52.3 ± 20.3 HU, respectively; the difference was significant between protocols A and B ($p = 0.05$), A and C ($p < 0.01$), and B and C ($p = 0.02$).

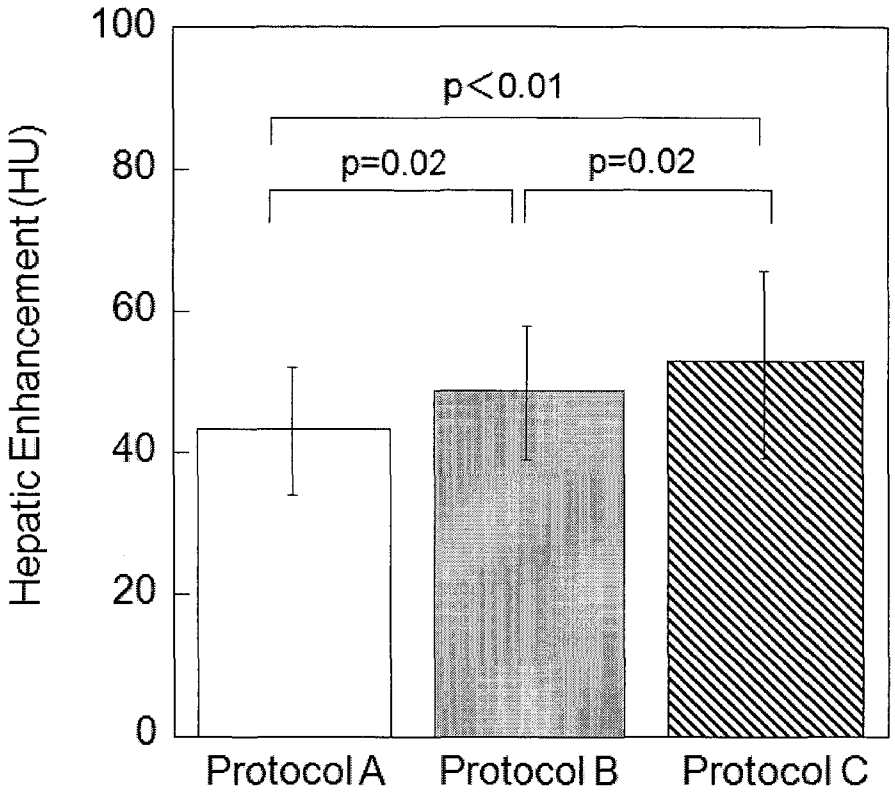

Figure 4.3. Hepatic enhancement in each contrast injection protocol during portal venous phase.

The mean values for hepatic enhancement were 43.2 HU ± 8.7, 48.7 HU ± 9.1, 53.9 HU ± 10.2, respectively, for protocols A, B, and C. There were statistically significant differences between protocols A and B, A and C, and B and C ($p = 0.02$, $p < 0.01$, and $p = 0.02$, respectively).

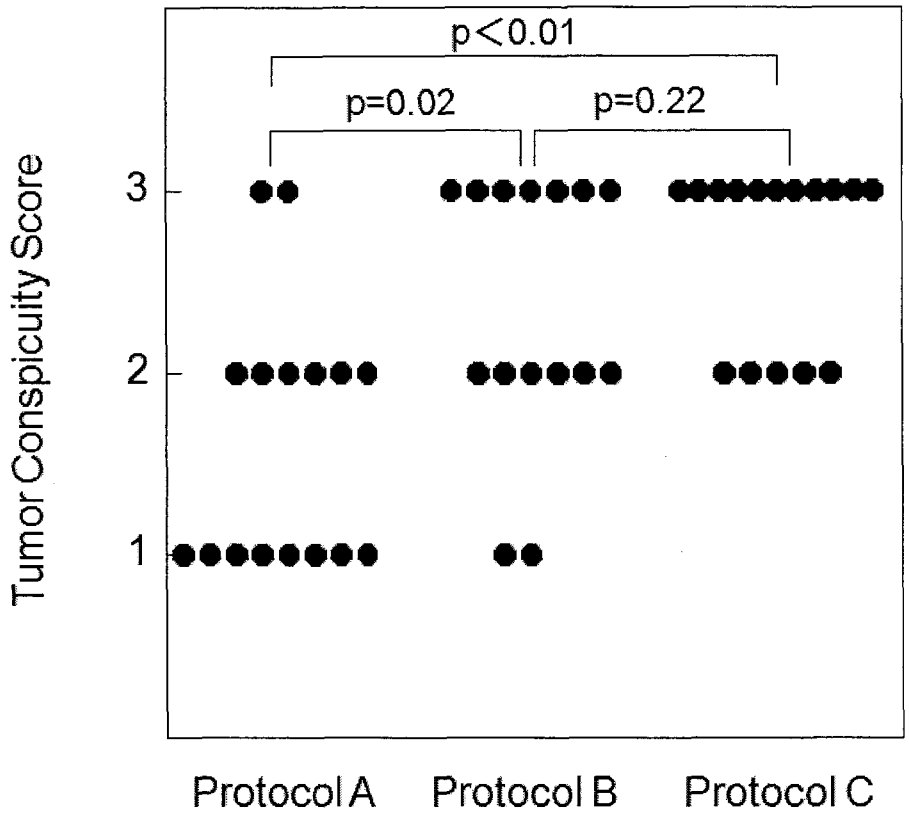

Figure 4.4. Visual evaluation of tumor conspicuity during the hepatic arterial phase for each of the 3 different contrast injection protocols. There was a significant difference between protocols A and B ($p = 0.02$) and A and C ($p < 0.01$) but not between protocols B and C ($p = 0.22$).

Figure 4.5.

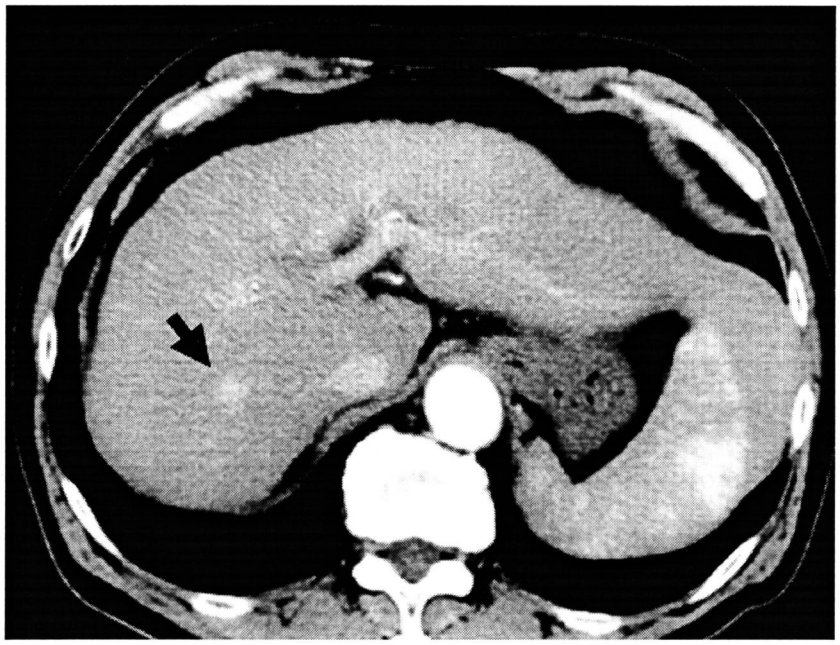

(a) Transverse CT image at the level of the left portal vein in a 68-year-old man with HCC, scanned according to protocol A. The TLC in this patient was 27.0 HU (mean TLC for protocol A, 26.5 HU).

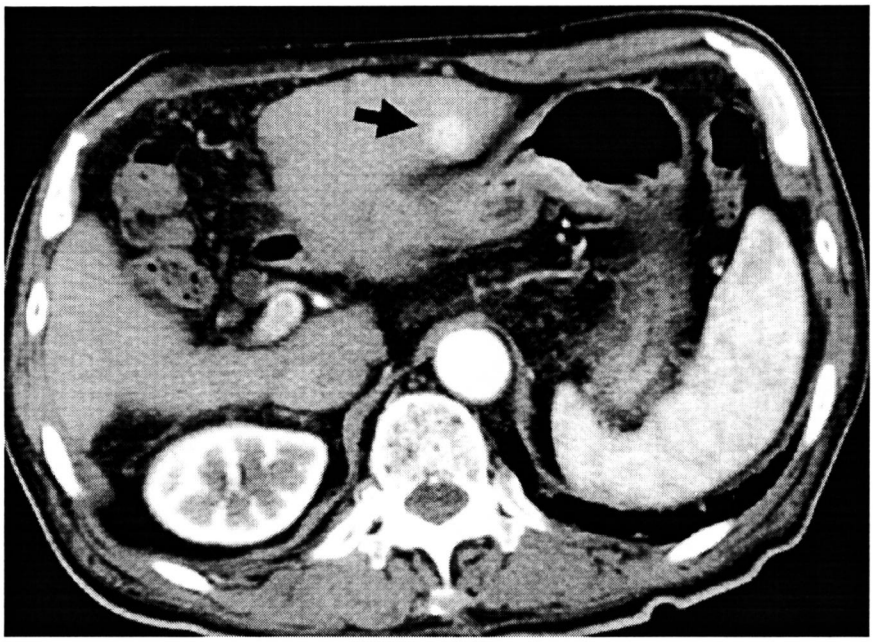

(b) Transverse CT image at the level of the porta hepatis in an 82-year-old man with HCC, scanned according to protocol B. The TLC in this patient was 44.0 HU (mean TLC for protocol B, 38.4 HU).

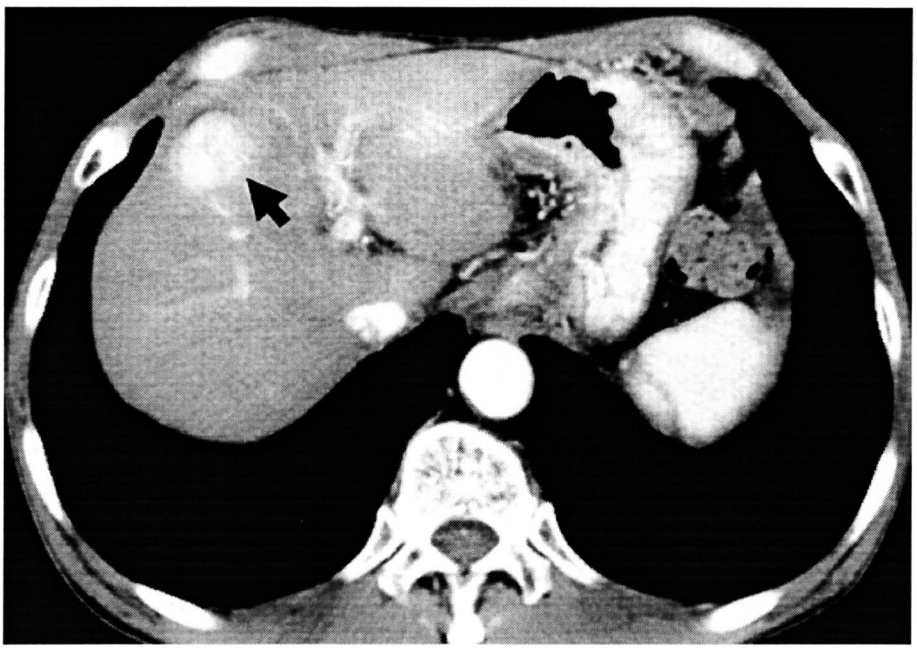

(c) Transverse CT image at the level of the left portal vein in a 73-year-old man with HCC, scanned according to protocol C. The TLC in this patient was 51.1 HU (mean TLC for protocol C, 52.3 HU).

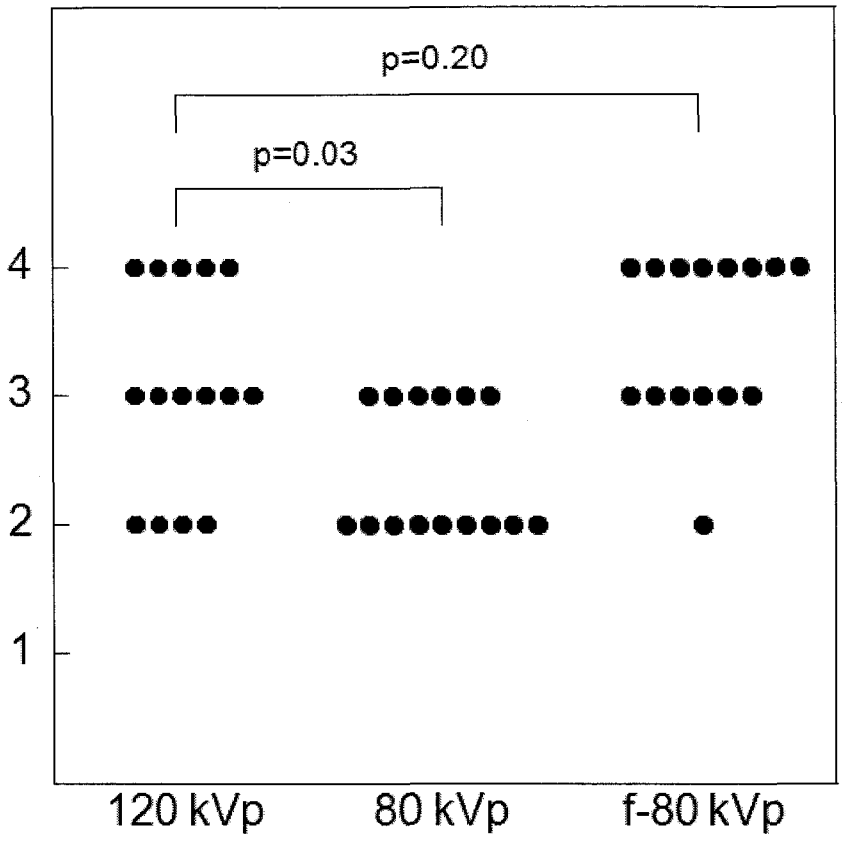

Figure 5.1. Diagnostic acceptability of the hepatic perfusion images with each scan technique.

In the visual evaluation of diagnostic acceptability of the hepatic perfusion images, there was no statistically significant difference between 120 kVp- and filtered 80 kVp images, while the difference between 120 kVp- and 80 kVp images was statistically significant.

Note: "f-80 kVp" means filtered 80 kVp images.

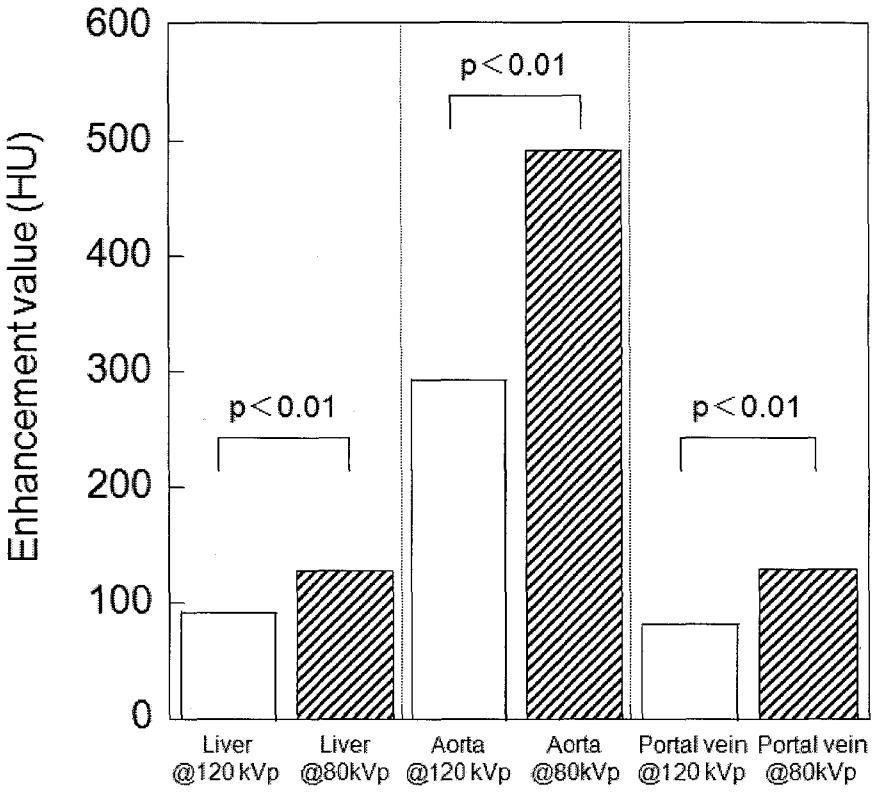

Figure 5.2. Enhancement values in the liver, aorta, and portal vein.

At all organs, the enhancement values were significantly higher on 80- than 120 kVp images ($p < 0.01$).

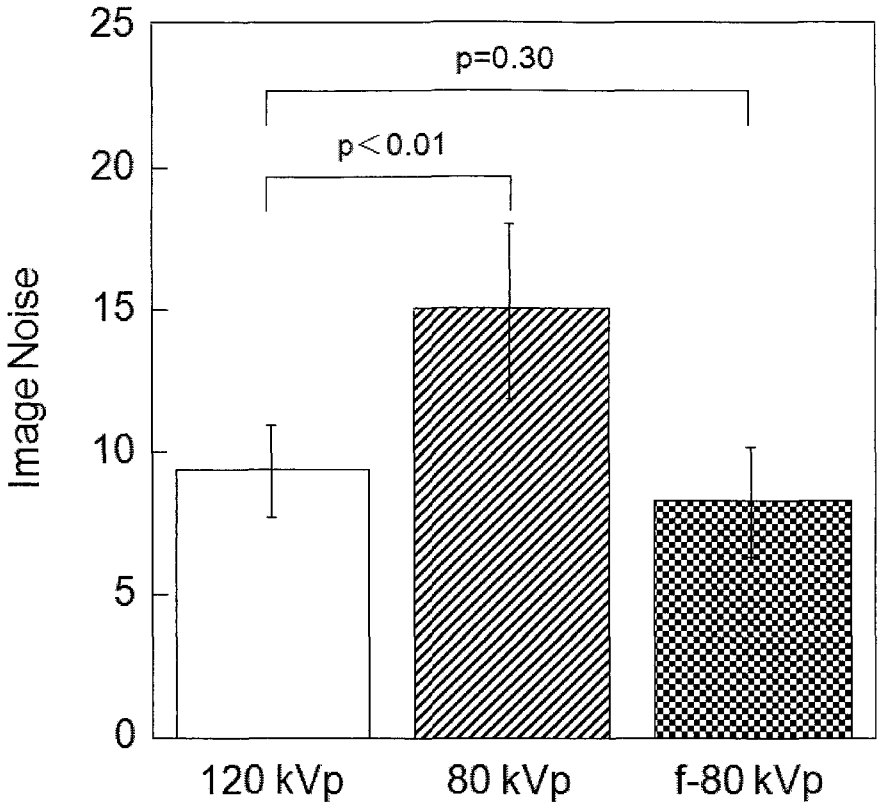

Figure 5.3. Image noise in the hepatic parenchyma in each technique.

There was no statistically significant difference between 120- and filtered 80-kVp images ($p = 0.30$), however, image noise was significantly lower on 120- than 80-kVp images ($p < 0.01$).

Note: "f-80 kVp" means filtered 80 kVp images.

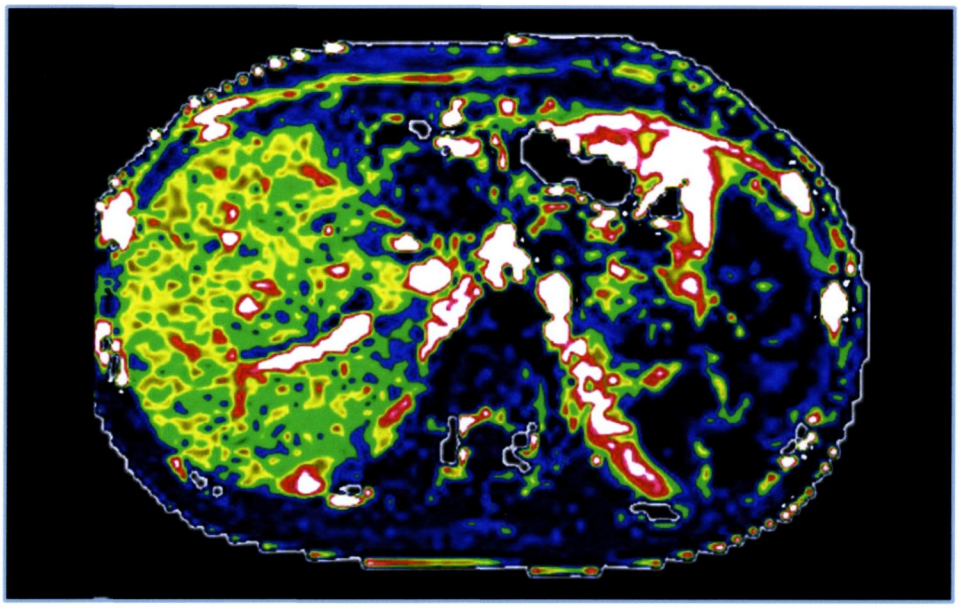

Figure 5.4. A 15-year-old girl who underwent living-related liver transplants (LRLT) due to Wilson disease.

The portal perfusion image acquired with 120 kVp showed fine granularity in the liver texture. There were minimal streak artifacts.

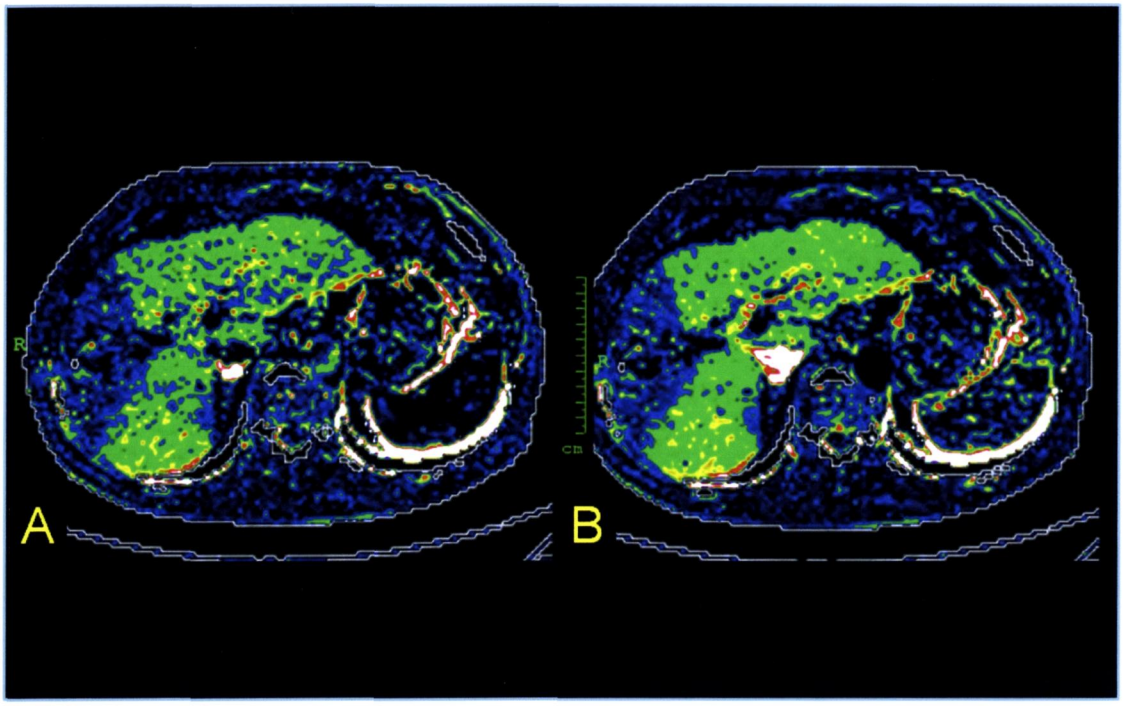

Figure 5.5. A 69-year-old man with hepatocellular carcinoma before percutaneous transhepatic portal vein embolization (PTPE). The comparison of portal perfusion images obtained with 80- (A) and filtered 80 kVp (B) demonstrated that the granularity in the liver texture was improved on filtered 80- compared to non-filtered 80 kVp images.

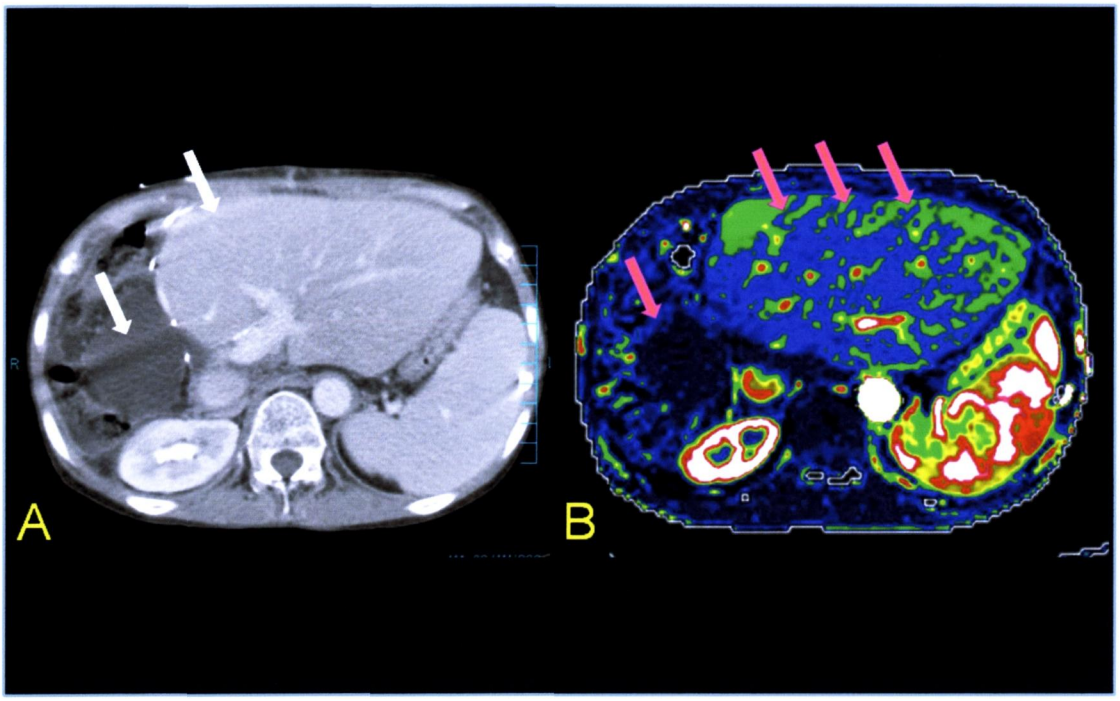

Figure 5.6. A 59-year-old female recipient of living-related liver transplants (LRLT) due to alcoholic cirrhosis. The source image of the hepatic perfusion CT scan acquired at 120 kVp (Fig. 5.6A, white arrow) and the corresponding hepatic arterial perfusion image (Fig. 5.6B, pink arrow) contained streak artifacts.

Table Lists and Tables

Table 3.1. Visual Analysis of Contrast Enhancement of the Pancreas during the Pancreatic Parenchymal Phase

Protocol and Patient	Image Grade			
Body Weight (kg)	1	2	3	4
1				
＜60 (n = 26)	0	0	5 (19)	21 (81)
≧60 (n = 13)	0	2 (15)	8 (62)	3 (23)
2				
＜60 (n = 22)	0	0	3 (14)	19 (86)
≧60 (n = 17)	0	0	4 (24)	13 (76)

Note. —Images were rated on a four-point scale, as follows: 1 = poor, 2 = fair, 3 = adequate, and 4 = excellent.

Data are numbers of patients, with percentages in parentheses.

Table 3.2. Estimated population mean and 95% confidence interval of pancreatic enhancement during pancreatic phase in each visual grade

Image Grade	Mean Enhancement (HU)	95% Confidence Interval (HU)
4	129.6 (23.0)	123.4, 135.8
3	99.0 (21.4)	88.3, 109.6
2	NC	NC
1	NC	NC

Note. —Numbers in parentheses are standard deviations.
The mean and 95 % confidence interval for grade 1 and 2 were not calculated because the sample number was very small (grade 2, $n = 2$; grade 1, $n = 0$).
NC = not calculated

Table 4.1. Patient's data in each protocol

Protocols	Patient Number	Age (average)	Body Weight (kg) (average)	Sex [Male/Female]	Number of Patients with HCCs	Number of Patients with single vs. multiple HCCs (single/multiple)	Number of HCC Nodules Evaluated	Size of HCC Nodules Evaluated (Average ± SD)
A	46	39-84 (67.1)	42-78 (59.1)	36/10	16	9/7	26	7-30 (20.8±6.9)
B	44	46-82 (66.6)	43-75 (58.2)	31/13	15	8/7	27	12-46 (22.6±7.2)
C	45	35-85 (58.2)	34-85 (58.7)	30/15	16	11/5	22	11-44 (21.9±7.8)
P values in statistical analysis	-	0.45*	0.89*	0.46**	0.99*	0.65**	-	0.21*

* tested by one-way analysis of variance (ANOVA)

** tested by $\chi 2$ test

Table 4.2. TLC Values by Tumor Conspicuity Grade

Conspicuity Grade	Population Mean (HU)	95% CI
1	21.1 ± 5.3	17.3, 25.0
2	35.6 ± 2.7	34.2, 36.9
3	53.2 ± 16.7	45.4, 61.0

*TLC values are given as the means ± SD

Table 5. Frequency of streak artifacts in each scan technique

Streak artifact	120 kVp	80 kVp	f-80 kVp
positive	5	2	2
negative	10	13	13

$P = 0.29$ at χ^2 test

Note. —Numbers indicate number of patients.

References

1. Taguchi K, Aradate H. Algorithm for image reconstruction in multi-slice helical CT. Med Phys 1998; 25:550-561.
2. Hu H. Multi-slice helical CT: scan and reconstruction. Med Phys 1999; 26:5-18.
3. Baron RL. Understanding and optimizing use of contrast material for CT of the liver. AJR Am J Roentgenol 1994; 163:323-331.
4. Bonaldi VM, Bret PM, Reinhold C, Atri M. Helical CT of the liver: value of an early hepatic arterial phase. Radiology 1995; 197:357-363.
5. Choi BI, Han JK, Cho JM, et al. Characterization of focal hepatic tumors. Value of two-phase scanning with spiral computed tomography. Cancer 1995; 76:2434-2442.
6. Frederick MG, McElaney BL, Singer A, et al. Timing of parenchymal enhancement on dual-phase dynamic helical CT of the liver: how long does the hepatic arterial phase predominate? AJR Am J Roentgenol 1996; 166:1305-1310.
7. Hollett MD, Jeffrey RB, Jr., Nino-Murcia M, Jorgensen MJ, Harris DP. Dual-phase helical CT of the liver: value of arterial phase scans in the detection of small (< or = 1.5 cm) malignant hepatic neoplasms. AJR Am J Roentgenol 1995; 164:879-884.
8. Honda H, Matsuura Y, Onitsuka H, et al. Differential diagnosis of hepatic tumors (hepatoma, hemangioma, and metastasis) with CT: value of two-phase incremental imaging. AJR Am J Roentgenol 1992; 159:735-740.
9. Hwang GJ, Kim MJ, Yoo HS, Lee JT. Nodular hepatocellular carcinomas: detection with arterial-, portal-, and delayed-phase images at spiral CT. Radiology 1997; 202:383-388.
10. Mitsuzaki K, Yamashita Y, Ogata I, Nishiharu T, Urata J, Takahashi M. Multiple-phase helical CT of the liver for detecting small hepatomas in patients with liver cirrhosis: contrast-injection protocol and optimal timing. AJR Am J Roentgenol 1996; 167:753-757.
11. Brink JA, Heiken JP, Forman HP, Sagel SS, Molina PL, Brown PC. Hepatic spiral CT: reduction of dose of intravenous contrast material. Radiology 1995; 197:83-88.
12. Foley WD, Hoffmann RG, Quiroz FA, Kahn CE, Jr., Perret RS. Hepatic helical CT: contrast material injection protocol. Radiology 1994; 192:367-371.

13. Foley WD, Kerimoglu U. Abdominal MDCT: liver, pancreas, and biliary tract. Semin Ultrasound CT MR 2004; 25:122-144.
14. Heiken JP, Brink JA, McClennan BL, Sagel SS, Crowe TM, Gaines MV. Dynamic incremental CT: effect of volume and concentration of contrast material and patient weight on hepatic enhancement. Radiology 1995; 195:353-357.
15. Yamashita Y, Komohara Y, Takahashi M, et al. Abdominal helical CT: evaluation of optimal doses of intravenous contrast material--a prospective randomized study. Radiology 2000; 216:718-723.
16. Fletcher JG, Wiersema MJ, Farrell MA, et al. Pancreatic malignancy: value of arterial, pancreatic, and hepatic phase imaging with multi-detector row CT. Radiology 2003; 229:81-90.
17. Lu DS, Reber HA, Krasny RM, Kadell BM, Sayre J. Local staging of pancreatic cancer: criteria for unresectability of major vessels as revealed by pancreatic-phase, thin-section helical CT. AJR Am J Roentgenol 1997; 168:1439-1443.
18. Lu DS, Vedantham S, Krasny RM, Kadell B, Berger WL, Reber HA. Two-phase helical CT for pancreatic tumors: pancreatic versus hepatic phase enhancement of tumor, pancreas, and vascular structures. Radiology 1996; 199:697-701.
19. McNulty NJ, Francis IR, Platt JF, Cohan RH, Korobkin M, Gebremariam A. Multi--detector row helical CT of the pancreas: effect of contrast-enhanced multiphasic imaging on enhancement of the pancreas, peripancreatic vasculature, and pancreatic adenocarcinoma. Radiology 2001; 220:97-102.
20. Diehl SJ, Lehmann KJ, Sadick M, Lachmann R, Georgi M. Pancreatic cancer: value of dual-phase helical CT in assessing resectability. Radiology 1998; 206:373-378.
21. Takeshita K, Furui S, Takada K. Multidetector row helical CT of the pancreas: value of three-dimensional images, two-dimensional reformations, and contrast-enhanced multiphasic imaging. J Hepatobiliary Pancreat Surg 2002; 9:576-582.
22. Tublin ME, Tessler FN, Cheng SL, Peters TL, McGovern PC. Effect of injection rate of contrast medium on pancreatic and hepatic helical CT. Radiology 1999; 210:97-101.
23. Vargas R, Nino-Murcia M, Trueblood W, Jeffrey RB, Jr. MDCT in Pancreatic adenocarcinoma: prediction of vascular invasion and resectability using a

multiphasic technique with curved planar reformations. AJR Am J Roentgenol 2004; 182:419-425.

24. Awai K, Nakayama Y, Nakaura T, et al. Prediction of aortic peak enhancement in monophasic contrast injection protocols at multidetector CT: phantom and patient studies. Radiat Med 2007; 25:14-21.
25. Brenner DJ, Hall EJ. Computed tomography--an increasing source of radiation exposure. N Engl J Med 2007; 357:2277-2284.
26. Berrington de Gonzalez A, Darby S. Risk of cancer from diagnostic X-rays: estimates for the UK and 14 other countries. Lancet 2004; 363:345-351.
27. Coppenrath E, Meindl T, Herzog P, et al. Dose reduction in multidetector CT of the urinary tract. Studies in a phantom model. Eur Radiol 2006; 16:1982-1989.
28. Funama Y, Awai K, Miyazaki O, et al. Improvement of low-contrast detectability in low-dose hepatic multidetector computed tomography using a novel adaptive filter: evaluation with a computer-simulated liver including tumors. Invest Radiol 2006; 41:1-7.
29. Funama Y, Awai K, Nakayama Y, et al. Radiation dose reduction without degradation of low-contrast detectability at abdominal multisection CT with a low-tube voltage technique: phantom study. Radiology 2005; 237:905-910.
30. Nakayama Y, Awai K, Funama Y, et al. Abdominal CT with low tube voltage: preliminary observations about radiation dose, contrast enhancement, image quality, and noise. Radiology 2005; 237:945-951.
31. Nakayama Y, Awai K, Funama Y, et al. Lower tube voltage reduces contrast material and radiation doses on 16-MDCT aortography. AJR Am J Roentgenol 2006; 187:W490-497.
32. Chow LC, Sommer FG. Multidetector CT urography with abdominal compression and three-dimensional reconstruction. AJR Am J Roentgenol 2001; 177:849-855.
33. Maher MM, Kalra MK, Rizzo S, Mueller PR, Saini S. Multidetector CT urography in imaging of the urinary tract in patients with hematuria. Korean J Radiol 2004; 5:1-10.
34. Sudakoff GS, Dunn DP, Hellman RS, et al. Opacification of the genitourinary collecting system during MDCT urography with enhanced CT digital radiography: nonsaline versus saline bolus. AJR Am J Roentgenol 2006; 186:122-129.

35. Sudakoff GS, Guralnick M, Langenstroer P, et al. CT urography of urinary diversions with enhanced CT digital radiography: preliminary experience. AJR Am J Roentgenol 2005; 184:131-138.
36. Toth TL. Dose reduction opportunities for CT scanners. Pediatr Radiol 2002; 32:261-267.
37. Kalra MK, Maher MM, Toth TL, et al. Strategies for CT radiation dose optimization. Radiology 2004; 230:619-628.
38. Kalra MK, Maher MM, Blake MA, et al. Detection and characterization of lesions on low-radiation-dose abdominal CT images postprocessed with noise reduction filters. Radiology 2004; 232:791-797.
39. Kalra MK, Maher MM, Sahani DV, et al. Low-dose CT of the abdomen: evaluation of image improvement with use of noise reduction filters pilot study. Radiology 2003; 228:251-256.
40. Khullar D, Subramanyan K, Johnson P. Evaluation of a noise-reduction contrast-enhancement algorithm for CT cardiac angiography. Proc SPIE 2005; 5749:310-318.
41. Kalra MK, Maher MM, Toth TL, Kamath RS, Halpern EF, Saini S. Comparison of Z-axis automatic tube current modulation technique with fixed tube current CT scanning of abdomen and pelvis. Radiology 2004; 232:347-353.
42. Kalra MK, Maher MM, Toth TL, et al. Techniques and applications of automatic tube current modulation for CT. Radiology 2004; 233:649-657.
43. Kalra MK, Rizzo S, Maher MM, et al. Chest CT performed with z-axis modulation: scanning protocol and radiation dose. Radiology 2005; 237:303-308.
44. McNitt-Gray MF. AAPM/RSNA Physics Tutorial for Residents: Topics in CT. Radiation dose in CT. Radiographics 2002; 22:1541-1553.
45. Jago J, Collet-Billon A, Chenal C, Jong J, Makram-Ebeid S. Adaptive enhnacement of ultrasound images. Medica Mundi 2002; 46:3.
46. Meuwly JY, Thiran JP, Gudinchet F. Application of adaptive image processing technique to real-time spatial compound ultrasound imaging improves image quality. Invest Radiol 2003; 38:257-262.
47. Burt P, Adelson E. The laplacian pyrmid as compact image code. IEEE trans Commun. 1983; 31:532-540.
48. Nakayama Y, Awai K, Yanaga Y, et al. Optimal contrast medium injection protocols for the depiction of the Adamkiewicz artery using 64-detector CT angiography. Clin Radiol 2008; 63:880-887.

49. Goldman LW. Principles of CT: radiation dose and image quality. J Nucl Med Technol 2007; 35:213-225; quiz 226-218.
50. Yanaga Y, Awai K, Nakaura T, et al. Optimal contrast dose for depiction of hypervascular hepatocellular carcinoma at dynamic CT using 64-MDCT. AJR Am J Roentgenol 2008; 190:1003-1009.
51. Yanaga Y, Awai K, Nakayama Y, et al. Optimal dose and injection duration (injection rate) of contrast material for depiction of hypervascular hepatocellular carcinomas by multidetector CT. Radiat Med 2007; 25:278-288.
52. Yanaga Y, Awai K, Nakaura T, et al. Low-dose Multidetector CT Urography (MDCTU) Using a Low Tube-Voltage Technique and an Adaptive Noise Reduction Filter: Feasibility Study. AJR Am J Roentgenol; (in press).
53. Kawashima A, Vrtiska TJ, LeRoy AJ, Hartman RP, McCollough CH, King BF, Jr. CT urography. Radiographics 2004; 24 Suppl 1:S35-54; discussion S55-38.
54. Noroozian M, Cohan RH, Caoili EM, Cowan NC, Ellis JH. Multislice CT urography: state of the art. Br J Radiol 2004; 77 Spec No 1:S74-86.
55. Goshima S, Kanematsu M, Kondo H, et al. MDCT of the Liver and Hypervascular Hepatocellular Carcinomas: Optimizing Scan Delays for Bolus-Tracking Techniques of Hepatic Arterial and Portal Venous Phases. AJR Am J Roentgenol 2006; 187:W25-W32.
56. Shinagawa M, Uchida M, Ishibashi M, Nishimura H, Hayabuchi N. Assessment of pancreatic CT enhancement using a high concentration of contrast material. Radiat Med 2003; 21:74-79.
57. Kim T, Murakami T, Takahashi S, et al. Pancreatic CT imaging: effects of different injection rates and doses of contrast material. Radiology 1999; 212:219-225.
58. Fenchel S, Fleiter TR, Aschoff AJ, van Gessel R, Brambs HJ, Merkle EM. Effect of iodine concentration of contrast media on contrast enhancement in multislice CT of the pancreas. Br J Radiol 2004; 77:821-830.
59. Matoba M, Kondou T, Yokota H, Higashi K, Tonami H. Usefulness of a saline flush for intravenous 3-dimensional computed tomography portography using multidetector-row helical computed tomography. J Comput Assist Tomogr 2005; 29:780-785.
60. Schoellnast H, Tillich M, Deutschmann HA, et al. Improvement of parenchymal and vascular enhancement using saline flush and power injection for multiple-detector-row abdominal CT. Eur Radiol 2004; 14:659-664.

61. Katayama H, Yamaguchi K, Kozuka T, Takashima T, Seez P, Matsuura K. Adverse reactions to ionic and nonionic contrast media. A report from the Japanese Committee on the Safety of Contrast Media. Radiology 1990; 175:621-628.
62. Keogan MT, McDermott VG, Paulson EK, et al. Pancreatic malignancy: effect of dual-phase helical CT in tumor detection and vascular opacification. Radiology 1997; 205:513-518.
63. Zeger SL, Liang KY, Albert PS. Models for longitudinal data: a generalized estimating equation approach. Biometrics 1988; 44:1049-1060.
64. Prokesch RW, Chow LC, Beaulieu CF, Bammer R, Jeffrey RB, Jr. Isoattenuating pancreatic adenocarcinoma at multi-detector row CT: secondary signs. Radiology 2002; 224:764-768.
65. Fishman EK, Horton KM, Urban BA. Multidetector CT angiography in the evaluation of pancreatic carcinoma: preliminary observations. J Comput Assist Tomogr 2000; 24:849-853.
66. Walkey MM. Dynamic hepatic CT: how many years will it take 'til we learn? Radiology 1991; 181:17-18.
67. Prokesch RW, Chow LC, Beaulieu CF, et al. Local staging of pancreatic carcinoma with multi-detector row CT: use of curved planar reformations initial experience. Radiology 2002; 225:759-765.
68. Awai K, Hiraishi K, Hori S. Effect of contrast material injection duration and rate on aortic peak time and peak enhancement at dynamic CT involving injection protocol with dose tailored to patient weight. Radiology 2004; 230:142-150.
69. Schueller G, Schima W, Schueller-Weidekamm C, et al. Multidetector CT of pancreas: effects of contrast material flow rate and individualized scan delay on enhancement of pancreas and tumor contrast. Radiology 2006; 241:441-448.
70. Baron RL, Oliver JH, 3rd, Dodd GD, 3rd, Nalesnik M, Holbert BL, Carr B. Hepatocellular carcinoma: evaluation with biphasic, contrast-enhanced, helical CT. Radiology 1996; 199:505-511.
71. Bae KT. Peak contrast enhancement in CT and MR angiography: when does it occur and why? Pharmacokinetic study in a porcine model. Radiology 2003; 227:809-816.
72. Francis IR, Cohan RH, McNulty NJ, et al. Multidetector CT of the liver and hepatic neoplasms: effect of multiphasic imaging on tumor conspicuity and vascular enhancement. AJR Am J Roentgenol 2003; 180:1217-1224.

73. Goshima S, Kanematsu M, Kondo H, et al. MDCT of the liver and hypervascular hepatocellular carcinomas: optimizing scan delays for bolus-tracking techniques of hepatic arterial and portal venous phases. AJR Am J Roentgenol 2006; 187:W25-32.
74. Kanematsu M, Goshima S, Kondo H, et al. Optimizing scan delays of fixed duration contrast injection in contrast-enhanced biphasic multidetector-row CT for the liver and the detection of hypervascular hepatocellular carcinoma. J Comput Assist Tomogr 2005; 29:195-201.
75. Koizumi M, Takada T, Kawarada Y, et al. JPN Guidelines for the management of acute pancreatitis: diagnostic criteria for acute pancreatitis. J Hepatobiliary Pancreat Surg 2006; 13:25-32.
76. Laghi A, Iannaccone R, Rossi P, et al. Hepatocellular carcinoma: detection with triple-phase multi-detector row helical CT in patients with chronic hepatitis. Radiology 2003; 226:543-549.
77. Sultana S, Awai K, Nakayama Y, et al. Hypervascular hepatocellular carcinomas: bolus tracking with a 40-detector CT scanner to time arterial phase imaging. Radiology 2007; 243:140-147.
78. Bae KT, Heiken JP, Brink JA. Aortic and hepatic peak enhancement at CT: effect of contrast medium injection rate--pharmacokinetic analysis and experimental porcine model. Radiology 1998; 206:455-464.
79. Bae KT, Heiken JP, Brink JA. Aortic and hepatic contrast medium enhancement at CT. Part I. Prediction with a computer model. Radiology 1998; 207:647-655.
80. Itoh S, Ikeda M, Achiwa M, Ota T, Satake H, Ishigaki T. Multiphase contrast-enhanced CT of the liver with a multislice CT scanner. Eur Radiol 2003; 13:1085-1094.
81. Schima W, Hammerstingl R, Catalano C, et al. Quadruple-phase MDCT of the liver in patients with suspected hepatocellular carcinoma: effect of contrast material flow rate. AJR Am J Roentgenol 2006; 186:1571-1579.
82. Awai K, Takada K, Onishi H, Hori S. Aortic and hepatic enhancement and tumor-to-liver contrast: analysis of the effect of different concentrations of contrast material at multi-detector row helical CT. Radiology 2002; 224:757-763.
83. Awai K, Inoue M, Yagyu Y, et al. Moderate versus high concentration of contrast material for aortic and hepatic enhancement and tumor-to-liver contrast at multi-detector row CT. Radiology 2004; 233:682-688.

84. Itoh S, Ikeda M, Achiwa M, Satake H, Ota T, Ishigaki T. Multiphase contrast-enhanced CT of the liver with a multislice CT scanner: effects of iodine concentration and delivery rate. Radiat Med 2005; 23:61-69.
85. Suzuki H, Oshima H, Shiraki N, Ikeya C, Shibamoto Y. Comparison of two contrast materials with different iodine concentrations in enhancing the density of the the aorta, portal vein and liver at multi-detector row CT: a randomized study. Eur Radiol 2004; 14:2099-2104.
86. Furuta A, Ito K, Fujita T, Koike S, Shimizu A, Matsunaga N. Hepatic enhancement in multiphasic contrast-enhanced MDCT: comparison of high- and low-iodine-concentration contrast medium in same patients with chronic liver disease. AJR Am J Roentgenol 2004; 183:157-162.
87. Yagyu Y, Awai K, Inoue M, et al. MDCT of Hypervascular Hepatocellular Carcinomas: A Prospective Study Using Contrast Materials with Different Iodine Concentrations. AJR Am J Roentgenol 2005; 184:1535-1540.
88. Lim JH, Kim EY, Lee WJ, et al. Regenerative nodules in liver cirrhosis: findings at CT during arterial portography and CT hepatic arteriography with histopathologic correlation. Radiology 1999; 210:451-458.
89. Svanholm H, Starklint H, Gundersen HJ, Fabricius J, Barlebo H, Olsen S. Reproducibility of histomorphologic diagnoses with special reference to the kappa statistic. Apmis 1989; 97:689-698.
90. Kim T, Murakami T, Takahashi S, et al. Effects of injection rates of contrast material on arterial phase hepatic CT. AJR Am J Roentgenol 1998; 171:429-432.
91. Lee KH, Choi BI, Han JK, Jang HJ, Kim TK, Han MC. Nodular hepatocellular carcinoma: variation of tumor conspicuity on single-level dynamic scan and optimization of fixed delay times for two-phase helical CT. J Comput Assist Tomogr 2000; 24:212-218.
92. Ichikawa T, Nakajima H, Nanbu A, Hori M, Araki T. Effect of injection rate of contrast material on CT of hepatocellular carcinoma. AJR Am J Roentgenol 2006; 186:1413-1418.
93. Kim T, Murakami T, Hori M, et al. Small hypervascular hepatocellular carcinoma revealed by double arterial phase CT performed with single breath-hold scanning and automatic bolus tracking. AJR Am J Roentgenol 2002; 178:899-904.

94. Murakami T, Kim T, Takamura M, et al. Hypervascular hepatocellular carcinoma: detection with double arterial phase multi-detector row helical CT. Radiology 2001; 218:763-767.
95. Obuchowski NA. Receiver operating characteristic curves and their use in radiology. Radiology 2003; 229:3-8.
96. Bader TR, Herneth AM, Blaicher W, et al. Hepatic perfusion after liver transplantation: noninvasive measurement with dynamic single-section CT. Radiology 1998; 209:129-134.
97. Sahani DV, Holalkere NS, Mueller PR, Zhu AX. Advanced hepatocellular carcinoma: CT perfusion of liver and tumor tissue--initial experience. Radiology 2007; 243:736-743.
98. Hakime A, Peddi H, Hines-Peralta AU, et al. CT perfusion for determination of pharmacologically mediated blood flow changes in an animal tumor model. Radiology 2007; 243:712-719.
99. Ignashov AM, Grinev KM, Kanaev AI, Perlei VE, Petrova SN. [Aneurysms of the pancreaticoduodenal artery in association with stenosis or occlusion of the celiac trunk]. Vestn Khir Im I I Grek 2005; 164:105-110.
100. Kan Z, Kobayashi S, Phongkitkarun S, Charnsangavej C. Functional CT quantification of tumor perfusion after transhepatic arterial embolization in a rat model. Radiology 2005; 237:144-150.
101. Miles KA, Hayball MP, Dixon AK. Functional images of hepatic perfusion obtained with dynamic CT. Radiology 1993; 188:405-411.
102. Jessen KA, Shrimpton PC, Geleijns J, Panzer W, Tosi G. Dosimetry for optimisation of patient protection in computed tomography. Appl Radiat Isot 1999; 50:165-172.